The Philosophical Magazine

FIRST PUBLISHED IN 1798

A Journal of Theoretical
Experimental and Applied Physics

THE PHILOSOPHICAL MAGAZINE

Authors wishing to submit papers for publication in the Journal should send manuscripts directly to the Publishers.

Manuscripts should be typed in *double* spacing on one side of quarto (8 × 10 in.) paper, and authors are urged to aim at absolute clarity of meaning and an attractive presentation of their texts.

References should be listed at the end in alphabetical order of authors and should be cited in the text in terms of author's name and date. Diagrams should normally be in Indian ink on white card, with lettering in soft pencil, the captions being typed on a separate sheet.

A leaflet giving detailed instructions to authors on the preparation of papers is available on request from the Publishers.

Authors are entitled to receive 25 offprints of a paper in the Journal free of charge, and additional offprints can be obtained from the Publishers.

The *Philosophical Magazine* and its companion journal, *Advances in Physics,* will accept papers for publication in experimental and theoretical physics. The *Philosophical Magazine* publishes contributions describing new results, letters to the editor and book reviews. *Advances in Physics* publishes articles surveying the present state of knowledge in any branch of the science in which recent progress has been made. The editors welcome contributions from overseas as well as from the United Kingdom, and papers may be published in English, French and German.

[825]

Magnetomechanical Damping in Chromium†

By M. E. DE MORTON

Australian Defence Scientific Service, Defence Standards Laboratories,
Department of Supply, Maribyrnong, Victoria, Australia

[Received November 29, 1960]

ABSTRACT

Damping hysteresis observed with changing temperature and strain-amplitude below $\sim 40°$C and a marked reduction of strain-amplitude-dependent damping in this region when a biasing tensile stress is present, is consistent with the suggestion that an antiferromagnetic domain structure exists in chromium below $\sim 40°$C.

§ 1. INTRODUCTION

RECENT neutron diffraction measurements by Bacon (1960, private communication) have shown that polycrystalline chromium is antiferromagnetic at room temperature losing the major portion of magnetic ordering at $\sim 40°$C, the Néel temperature; the exact form of the curve is, however, sensitive to grain size. Changes in the temperature coefficient of several physical properties (see Sully 1954) also occur at this temperature and recently inflections in the magnetic susceptibility (Lingelbach 1958) and heat content (Beaumont *et al.* 1960) curves have been detected at $\sim 40°$C. Internal friction measurements (de Morton 1960) made at 1 c.p.s. on annealed high purity polycrystalline chromium have shown a steep rise in logarithmic decrement below $\sim 40°$C; moreover, damping in this region is strain-amplitude dependent. This form of damping is destroyed by heavy plastic deformation. The presence of an antiferromagnetic domain structure below $\sim 40°$C has been invoked to explain these internal friction phenomena, damping originating from stress-induced irreversible movement of domain walls. Street and Lewis (1956) however have pointed out that the formation of a domain structure is not a necessary consequence of antiferromagnetism; antiferromagnetic Cr_2O_3 for example does not behave according to domain theory.

The method for determining unequivocally the presence of magneto-mechanical damping in ferromagnetics by immobilizing domain boundaries in a strong external magnetic field is inapplicable with antiferromagnetics because of their intrinsic magnetic properties; however, domains can be aligned by a stress and this feature was tested in the present work.

---

† Communicated by Professor L. F. Bates, F.R.S.

§ 2. Experimental

Measurement of damping was made in an evacuated (10^{-5} mm Hg) torsional pendulum apparatus (background decrement, 4×10^{-5}) on a high purity chromium† specimen 0·076 cm diameter by 26 cm long. Adjustments were made to the inertia member attached to the free end of the specimen so that the natural frequency of vibration was 1 c.p.s. The measure of damping used was logarithmic decrement $\delta = 1/n \ln \theta_0/\theta_n$ where θ_0 is the initial amplitude and θ_n the amplitude after n oscillations. For small angles of twist the surface shear strain $\phi = r\theta/l$ where r and l are the radius and length of the specimen and θ the angle of twist in radians. The specimen was annealed *in vacuo* at 1150°c to give a grain diameter of 2–7 μ. Static tensile loading was applied by suspending weights from the free end of the specimen and frequency kept constant by adjusting bobs along the inertia bar. The maximum static stress applied was below 0·1 of the engineering elastic limit. After application of a stress the specimen was disordered by heating above the Néel temperature and slowly cooled before measurements were made.

§ 3. Results

Measurement of damping with temperature below 70°c gave a wide hysteresis loop on cooling and heating, fig. 1; this was not detected in previous measurements (de Morton 1960) because of high background damping. Measurement of internal friction as a function of strain amplitude at 19°c showed a marked amplitude dependence up to a strain of 10^{-4}, fig. 2; at higher strains internal friction was almost independent of amplitude. Hysteresis was also observed in these measurements on increasing and decreasing strain amplitude. (The measurements shown in figs. 1 and 2 were made with the minimum static tensile stress, i.e. 34 kg/cm².)

The effect of increasing the static tensile stress on internal friction in the strain-amplitude-dependent region is shown in fig. 3; at a strain of 9×10^{-5} the decrement is reduced by 40% and the amplitude-dependence is markedly reduced by the application of a static tensile stress of 232 kg/cm². These measurements were made on increasing amplitude only. Damping at 55°c, i.e. slightly above the Néel temperature, for all biasing stresses was about background level and essentially independent of strain amplitude. Similar measurements were made at other temperatures and constant amplitude resulted in the family of curves shown in fig. 4 showing firstly, the rapid decrease of decrement as the Néel temperature is approached and secondly, the large reduction in logarithmic decrement on increasing the static tensile stress on the specimen.

---

† Analysis: (Weight %): Mg <0·0002, Pb 0·0002, Si <0·0005, Al 0·0005, Fe <0·0005, Cu 0·0002, Ag 0·0001, Ti Trace, C <0·0005, O 0·013, N 0·0009, H <0·0002.
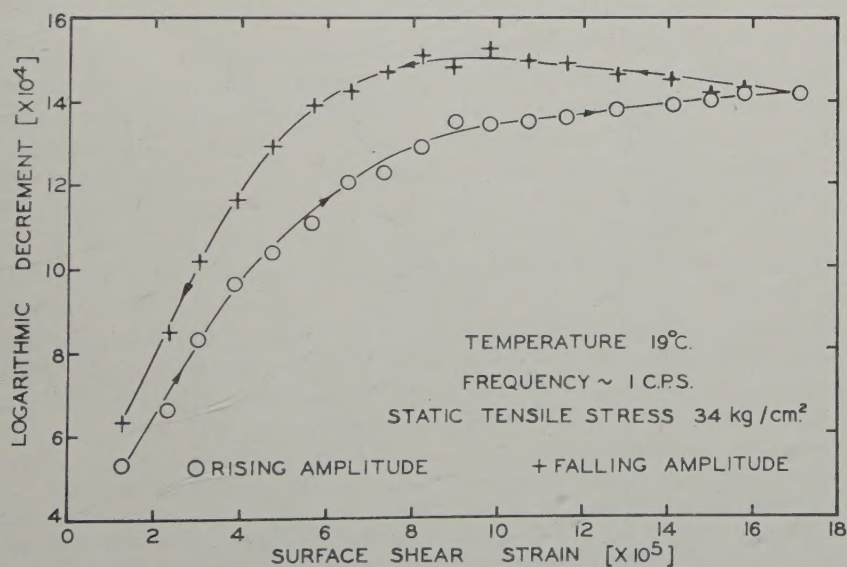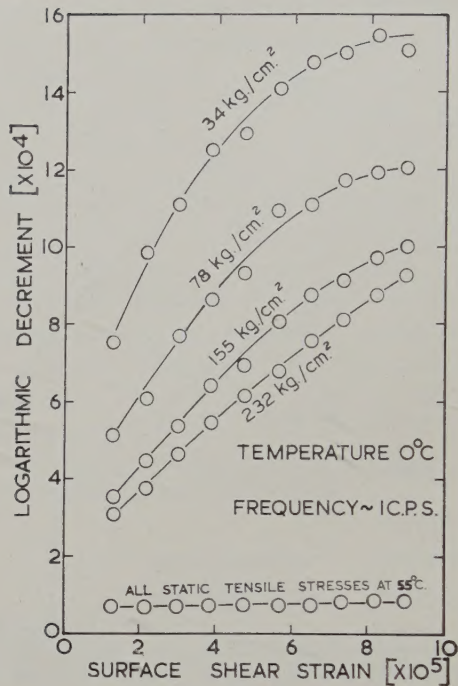
Fig. 1
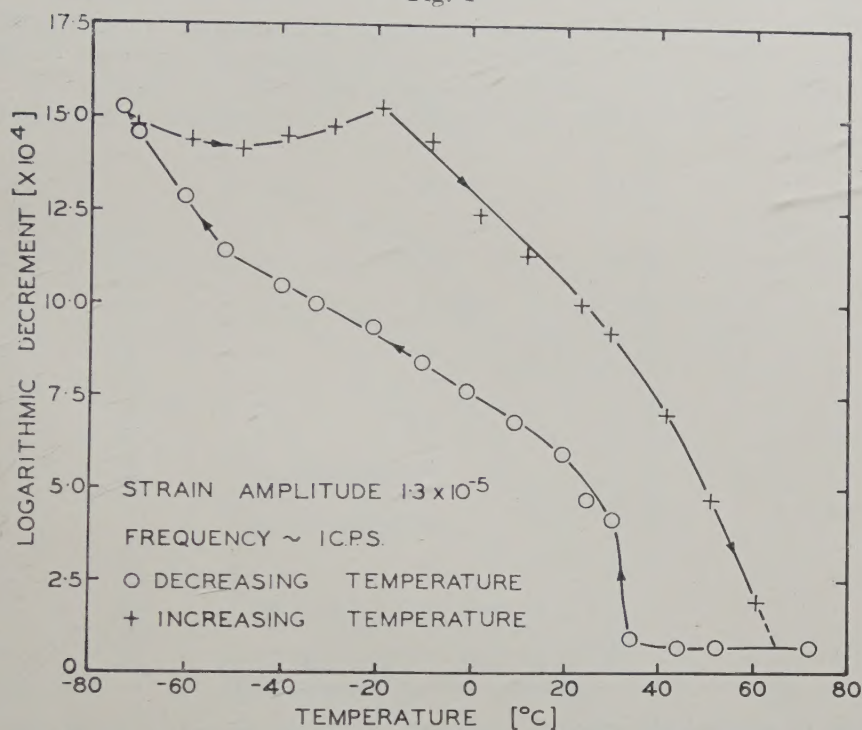
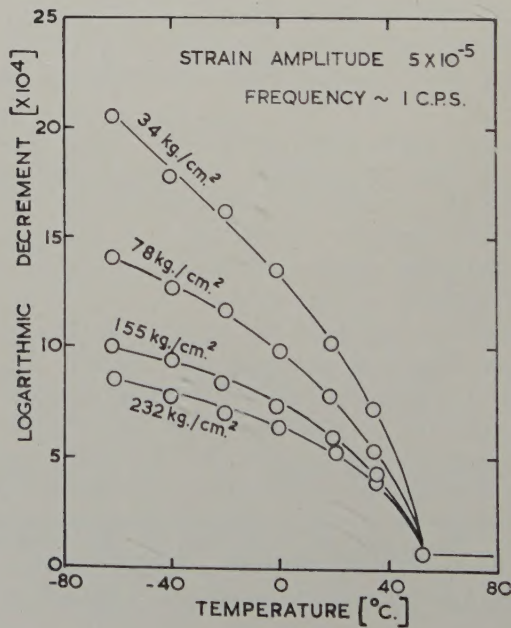Damping hysteresis loop as a function of temperature.

Fig. 2

Effect of rising and falling strain amplitude on logarithmic decrement.

M. E. de Morton *on*

Fig. 3

Effect of static tensile stress on the strain amplitude dependence of internal friction.

Fig. 4

Temperature dependence of internal friction at various static tensile stresses.

The form of the relationship between static tensile stress and observed damping at constant amplitude and temperature is shown graphically in fig. 5, the effect on damping being more marked at low stresses.

No permanent effect due to the maximum static stress used was observed on unloading to the minimum stress and re-testing.

Fig. 5

STRAIN   AMPLITUDE 5×10^{-5}
TEMPERATURE $- 62°C.$
FREQUENCY $\sim$ I C.P.S.
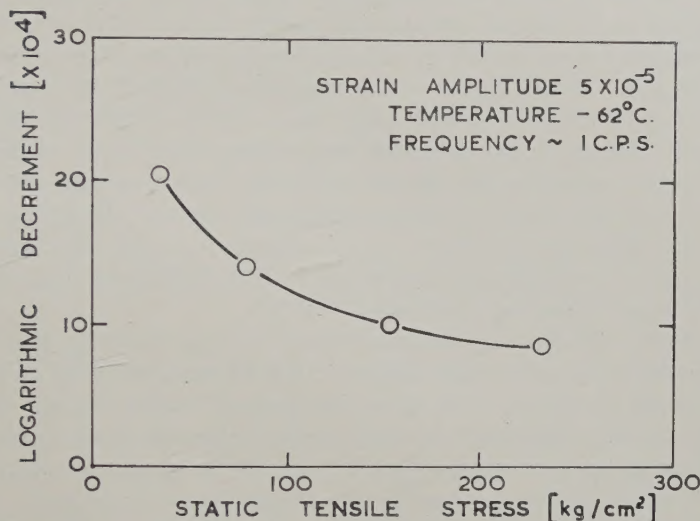
Effect of static tensile stress on logarithmic decrement.

§ 4. DISCUSSION

The close correspondence at $\sim 40°C$ between the onset of strain-amplitude-dependent damping observed at low frequencies and the appearance of magnetic ordering detected by neutron diffraction strongly suggests that damping originates from the stress-induced motion of antiferromagnetic domain boundaries. This inference is consistent with the absence of damping below $40°C$ in internal friction measurements made on electroformed chromium in the kilocycle frequency range by Fine *et al.* (1951) where insufficient time would be available for appreciable domain wall movement†; moreover, a superimposed biasing stress markedly reduces the internal friction which would follow if the preferential alignment of domains and partial fixing of domain walls occurred. Neither of these effects would be expected if damping was due to the movement of dislocation boundaries, the other most likely source of

---

† The marked internal friction peak observed by Fine *et al.* at $37°C$ is however very similar to the anomalous absorption of ultrasonic sound measured by Belov *et al.* (1960) in antiferromagnets at the Néel temperature and explained quantitatively by them as due to a redistribution of spins within domains by elastic stresses.

amplitude-dependent damping; dislocation damping appears generally insensitive to frequency (Lücke and Granato 1957) and further is increased by the application of a static stress as shown by Baker (1957).

Damping increases with decreasing temperature below the Néel temperature (fig. 1) as the degree of magnetic ordering within domains becomes stronger and on heating from $-70°c$ a lag of $\sim 50°c$ occurs before the loss of magnetic ordering reduces the volume of domains affected by the stress of measurement. (The dip in the curve observed immediately on heating is reproducible, but its origin is at present obscure.) The hysteresis loop observed at constant temperature and varying strain amplitude, fig. 2, is analogous to the magnetic hysteresis loop and implies that domain boundary jumps occur at a lower stress on decreasing amplitude. Figure 2 also shows an early linear dependence of decrement on amplitude, changing to almost amplitude-independence above 10^{-4}, presumably as saturation of domain alignment begins. (In ferromagnetics this linear dependence, which is in accordance with the mechanical counterpart of Rayleigh's law (see Bozorth 1959) is followed by a maximum in the curve as shown by Boulanger (1949).)

The effect of the biasing tensile stress is to align the magnetic domains and these domains will remain aligned if the vibrational stress of measurement is small compared with the superimposed biasing stress. Thus the damping and its amplitude and temperature dependence decrease rapidly as the biasing stress increases, figs. 3, 4 and 5, in much the same way as internal friction in ferromagnetics is reduced by external fields (Sumner and Entwistle 1959) and applied static tensile stress (Cochardt 1954).

Recently Corliss *et al.* (1959) have suggested an antiphase antiferromagnetic domain structure for chromium single crystals from a consideration of the splitting of neutron diffraction reflections.

References

BAKER, G. S., 1957, *J. appl. Phys.*, **28,** 734.
BEAUMONT, R. H., CHIHARA, H., and MORRISON, J. A., 1960, *Phil. Mag.*, **5,** 188.
BELOV, K. P., KATAYEV, G. I., and LEVITIN, R. Z., 1960, *J. appl. Phys.*, **31,** 153S.
BOULANGER, C., 1949, *Rev. Met.*, **46,** 321.
BOZORTH, R. M., 1951, *Ferromagnetism* (New York: Van Nostrand), p. 708.
COCHARDT, A. W., 1954, *J. appl. Phys.*, **25,** 670.
CORLISS, L. M., HASTINGS, J. M., and WEISS, R. J., 1959, *Phys. Rev. Letters*, **3,** 211.
FINE, M. E., GREINER, E. S., and ELLIS, W. C., 1951, *J. Met.*, **191,** 56.
LINGELBACH, R., 1958, *Z. Phys. Chem.*, *Frankfurt*, **14,** 1.

LÜCKE, K., and GRANATO, A., 1956, *Dislocations and Mechanical Properties of Crystals* (New York: Wiley, 1957).

DE MORTON, M. E., 1960, *Trans. Amer. Inst. min. (metall.) Engrs*, **218**, 294.

STREET, R., and LEWIS, B., 1956, *Phil. Mag.*, **1**, 663.

SULLY, A. H., 1954, *Chromium* (London: Butterworth Scientific Publications), Chap. 3.

SUMNER, G., and ENTWISTLE, K. M., 1959, *J. Iron St. Inst.*, **192**, 238.

The Interactions of π^--mesons with Complex Nuclei in the Energy Range (100–800) MeV

II. The Interaction Lengths and Elastic Scattering of 750 MeV π^--mesons in G5 Emulsion†

By J. E. Allen, A. J. Apostolakis, Y. J. Lee‡, J. V. Major
and E. Perez Ferreira§

The Physics Department, The Durham Colleges in the University of Durham,
Durham

Abstract

A total of 100·5 m of track has been scanned in a block of emulsion exposed to the 750 MeV π^--meson beam of the Brookhaven cosmotron. Allowing for the beam contamination of 7%, the interaction lengths for the production of inelastic events and for elastic scattering with projected angles of $2 \leqslant \phi < 10°$ are $(43·6 \pm 2·9)$ cm and $(66·8 \pm 5·6)$ cm respectively. The geometrical interaction length is 29·3 cm. A comparison with the optical model of the nucleus gives a value for the absorption coefficient $K = (1·5 \pm 0·2)\ 10^{12}$ cm^{-1} and for the change in wave number $k_1 = (1·84 \pm 0·06)\ 10^{12}$ cm^{-1}. The absorption coefficient corresponds to a mean free path in nuclear matter $\lambda_n = (6·7 \pm 0·9)\ 10^{-13}$ cm, to an imaginary component of potential $V_i = (15 \pm 2)$ MeV and with the value of the change in wave number to a real potential $V_r = (36 \pm 1)$ MeV.

§ 1. Introduction

This paper is the second of a series concerned with an examination of the interaction characteristics of π^--mesons with G5 emulsion nuclei within the energy range (100–800) MeV. A previous publication (Allen *et al.* 1959) dealt with the elastic scattering of π^--mesons at an energy of 88 MeV and will be referred to hereafter as I.

§ 2. Interaction Lengths and Elastic Scattering of 750 MeV π^--mesons in G5 Emulsion

2.1. *Experimental*

The emulsion block consisted of pellicles each 2 in. × 3 in. × 400 μ and had been exposed to the 750 MeV beam of the Brookhaven cosmotron. The stack was received already processed.

A similar method of scanning was employed to that described in I. It was carried out on four Cooke M4000 microscopes under a magnification

---

of $45 \times 1.5 \times 15$. Tracks lying within $\pm 5°$ of the general beam direction were selected 1 cm from the edge of the emulsion. An eyepiece hairline was aligned on each track to be followed and a comparison of the track with this direction was made at intervals. Each track was followed to an interaction, out of the emulsion or for a maximum length of 2·5 cm. The beam energy of 750 Mev was not expected to vary appreciably over this length.

An initial classification of the interactions was made into elastic scatterings of type $(n_h = 0, \ n_s = 1)$ and stars, the latter group including disappearances $(n_h = 0, \ n_s = 0)$. A careful search was made over a region of 150μ around each disappearance for secondary tracks or for a continuing primary. Star-sizes were estimated visually, particular attention being paid to those of type $(n_h = 1, n_s = 1)$. Of 19 such events, three were identified on dynamical grounds as $\pi^- - $p collisions with a visible recoiling proton; they were classified therefore as elastic scatterings.

All detectable scatterings with horizontally projected angle $\phi \geqslant 1°$ were recorded and determined from the coordinates of four points on the track, two on either side of the point of scattering. Those events having $\phi < 2°$ were later discarded as being due chiefly to Rutherford scattering.

2.2. *The Interaction Lengths*

There were found in a total track length of 100·5 m, 282 events initially classified as elastic scatterings, 3 π^-p elastic scatterings and 233 stars including 19 disappearances. Of the elastic scatterings, 130 were through projected angles $\phi < 2°$ and were due chiefly to Rutherford scattering, and 12 were through angles $\phi \geqslant 10°$ for which the probability of diffraction scattering is very small. Allowing for the contamination of the beam which has been given as 7% (Blau and Oliver 1956, Lindenbaum and Yuan 1955), the interaction length for the formation of inelastic events in G5 emulsion at 750 Mev is (43.6 ± 2.9) cm and the interaction length for elastic scattering through projected angles $2 \leqslant \phi < 10°$ is (66.8 ± 5.9) cm.

The mean free path for inelastic interaction is consistent with that which can be computed from Blau and Oliver (1956) of (42.6 ± 2.4) cm at 750 Mev and by Barbaro *et al.* (1958) of (42.4 ± 2.4) cm at 570 Mev. Moreover the three elastic scatterings on hydrogen which were identified in the events of type $(1 + 1)\pi$ are consistent with the five events expected from the cross sections of Crittenden *et al.* (1959). From this it is concluded that scanning losses are small.

2.3. *Comparison with the Optical Model*

A summary of the essential features of the optical model of nuclear interactions and its application to emulsion nuclei has been given in I. The cross section for inelastic interaction is determined by the radii of emulsion nuclei and the absorption coefficient, K, of nuclear matter for

meson waves. The total and differential cross sections for elastic scatterings are both further determined by the change in the wave number, k_1, of the meson wave on penetrating nuclear matter. From the expressions for the inelastic cross section given in I, the variation (with the absorption coefficient) of the interaction length for inelastic interactions, λ_a, has
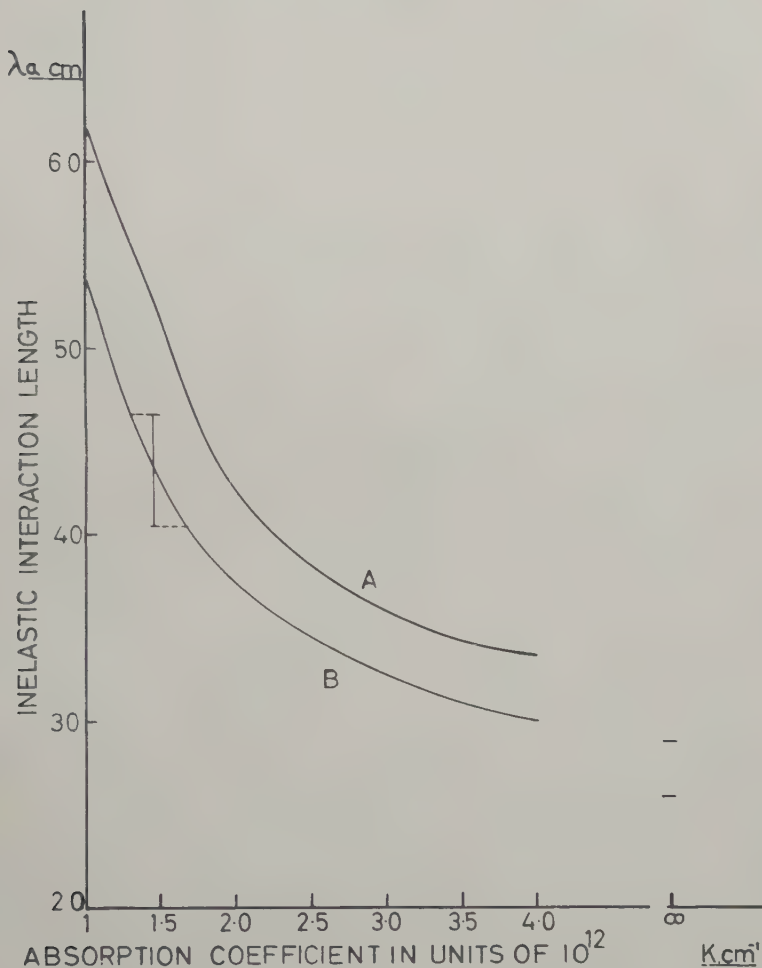
Fig. 1

The variation of the inelastic interaction length with absorption coefficient. Curve A is computed from the optical model and in curve B allowance has been made for the de Broglie wavelength.

been calculated. This is shown as curve A of fig. 1; the nuclear radii have been taken as $r_0 A^{1/3}$ with r_0 as $1\cdot35 \times 10^{-13}$ cm. The increase in cross section due to Coulomb attraction was calculated to be of the order

J. E. Allen *et al. on the*

of 2% and is considered negligible. In curve B allowance has been made for the de Broglie wavelength of the meson. Using this curve the experimental value of the interaction length yields a value of $(1\cdot5 \pm 0\cdot2)10^{12}$ m^{-1} for the absorption coefficient.

Fig. 2
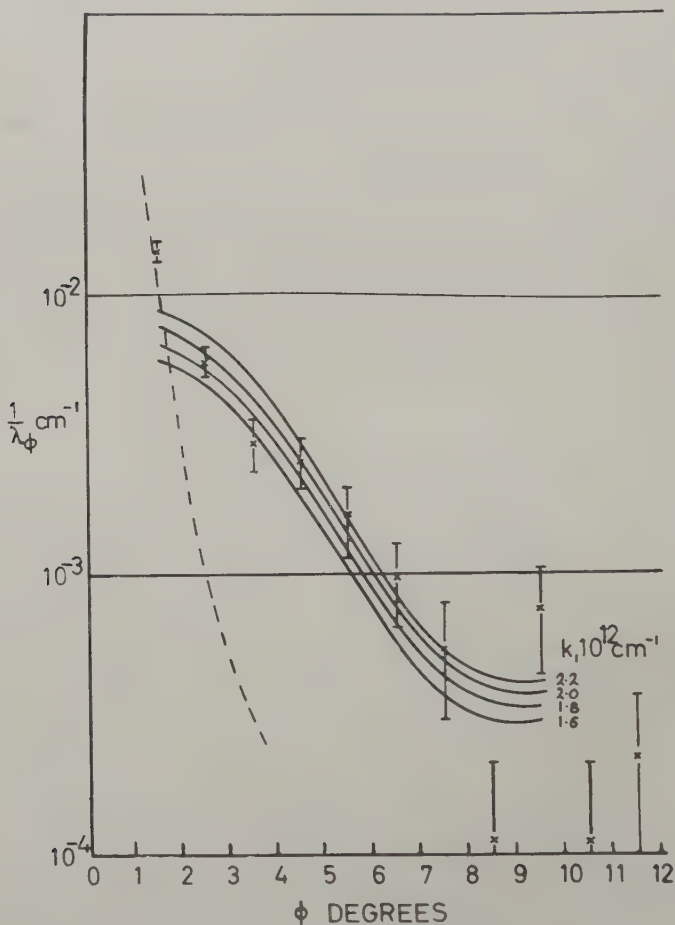
The observed distribution of horizontally projected angles of elastic scattering per 1° interval. The full curves have been calculated from the optical model for various assumed values of nuclear potential. The broken line represents Rutherford scattering.

With this value of absorption coefficient, the horizontally projected angular distribution of the scattered mesons was calculated for various assumed values of the change in wave number between 1·6 and $2\cdot2 \times 10^{12}$ cm^{-1} which correspond to various values of the real component of nuclear potential. In fig. 2 are shown the calculated distributions and

the experimental results, together with the distribution for Rutherford scattering. It is seen that the contribution of the latter to the angular distribution is small above 2°. To obtain a precise value of k_1 a numerical integration of the distributions was carried out to give the interaction length for scattering through projected angles between 2° and 10° as a function of k_1. The observed value of the interaction length corresponds to $k_1 = (1 \cdot 84 \pm 0 \cdot 06) 10^{12}$ cm^{-1}.

The attenuation mean free path of the meson wave in nuclear matter, λ_n, is given by $1/K$ and is found to be $(6 \cdot 7 \pm 0 \cdot 9) 10^{-13}$ cm; it corresponds to an imaginary component of nuclear potential $V_i = (15 \pm 2)$ MeV. The value of k_1 corresponds to a real component of potential $V_r = (36 \pm 1)$ MeV.

2.4. *Discussion*

The absorption coefficient may be calculated if the detailed processes of the inelastic interaction are known. Evidence of these may be obtained from the meson star-size at 750 MeV which is found to be $(4 \cdot 1 + 0 \cdot 5) \pi$. The secondary particles with ionization near the minimum value will be chiefly charged mesons. If allowance is made for uncharged mesons then the scattering of mesons must be the predominant process of inelastic interaction. In the case of the inelastic scattering arising from several scatterings of the meson on individual nucleons within the nucleus, the absorption coefficient may be calculated from the cross sections $\sigma_{\pi^- p}$, $\sigma_{\pi^+ p}$ of charged mesons in hydrogen. These are reduced within the nucleus by the restriction on low-energy transfers imposed by the Pauli exclusion principle. There are insufficient data at energies near 750 MeV to support a detailed calculation of this effect. An approximate calculation has been made assuming that the momenta of the nucleons are given by a Fermi distribution. The reduction in the cross section for elastic and charge exchange scattering in hydrogen is calculated approximately by the method of Cronin *et al.* (1957) and is about 13%. The reduction in the cross section for production of mesons in hydrogen has been computed from the momentum distribution of the recoiling nucleon (Puppi 1958), and is 32%. The total cross section for interaction of 750 MeV π^--mesons is thereby reduced by about 25% and it is assumed that there will be a similar reduction in the cross section for interaction of π^+-mesons.

Recent determinations of $\sigma_{\pi^- p}$ and $\sigma_{\pi^+ p}$ have been made by Burrowes *et al.* (1959) and Brisson *et al.* (1959) who found the cross sections to be (38 ± 2) mb and (17 ± 1) mb respectively. Assuming charge independence and allowing for the exclusion principle, the absorption coefficient is calculated to be $(2 \cdot 0 \pm 0 \cdot 1) 10^{12}$ cm^{-1} for the average emulsion nucleus. The estimate of error arises from the experimental uncertainties on $\sigma_{\pi^- p}$ and $\sigma_{\pi^+ p}$ and includes no estimate of the inaccuracies involved in the very approximate calculation of the Pauli effect. In view of this it is felt that significance should not be attached to the difference between this value of K and the value deduced earlier from the experimental results.

REFERENCES

ALLEN, J. E., APOSTOLAKIS, A. J., LEE, Y. J., MAJOR, J. V., and PEREZ FERREIRA, E., 1959, *Phil. Mag.*, **4**, 858.
BARBARO, A., BARONI, G., and CASTAGNOLI, C., 1958, *Nuovo Cim.*, **9**, 154.
BLAU, M., and OLIVER, A. R., 1956, *Phys. Rev.*, **102**, 489.
BRISSON, J. C., DETOEF, J., FALK-VAIRANT, P., VAN ROSSUM, L., VALLADAS, G., and YUAN, L. C. L., 1959, *Phys. Rev. Letters*, **3**, 561.
BURROWES, H. C., CALDWELL, D. O., FRISCH, D. H., HILL, D. A., RITSON, D. M., SCHULTER, R. A., and WAHLIG, M. A., 1959, *Phys. Rev. Letters*, **2**, 119.
CRITTENDEN, R. R., SCANDRETT, J. H., SHEPHARD, W. D., WALKER, W. D., and BALLAM, J., 1959, *Phys. Rev. Letters*, **2**, 121.
CRONIN, J. W., COOL, R., and ABASHIAN, A., 1957, *Phys. Rev.*, **107**, 1121.
LINDENBAUM, S. J., and YUAN, L. C. L., 1955, *Phys. Rev.*, **100**, 306.
PUPPI, G., 1958, *Annual International Conference on High Energy Physics at C.E.R.N.*, p. 39.

The Influence of Impurity Atoms on the Annealing Kinetics of Electron Irradiated Copper†

By D. G. MARTIN

Metallurgy Division, Atomic Energy Research Establishment, Harwell, Didcot, Berks

ABSTRACT

Spectroscopically pure copper and three dilute copper alloys containing approximately 0·05 atomic % of silver, cadmium and beryllium respectively have been irradiated with 4 MeV electrons at −196°c and then annealed at temperatures up to +50°c. The recovery of the irradiation damage has been observed by measuring changes in electrical resistance, measured in liquid helium.

Three annealing peaks at approximately −140°, −80° and 0°c have been observed in the spectroscopically pure copper. Similar peaks occur also in the dilute alloys, but their exact form is significantly altered. A tentative explanation consistent with a widely held description of the annealing stages in irradiated copper is put forward.

§ 1. INTRODUCTION

QUALITATIVELY it is now well recognized that impurity atoms appreciably influence the annealing kinetics of point defects in metals. As a result, materials in the purest form available are normally chosen for fundamental experiments in irradiation damage.

However, few quantitative observations of this impurity effect have been made. Blewitt *et al.* (1957) have neutron irradiated a number of dilute copper alloys at 14°K and shown that the 40°K annealing stage could be suppressed by impurity atoms that were both larger and smaller than copper.

Lomer and Cottrell (1955) have proposed that impurity atoms can act as trapping centres for point defects, and so hold up their migration and eventual annihilation. So far no detailed calculations have been performed to determine the feasibility of a specific defect being trapped by a particular impurity atom, and if so, the depth of the trap. Such a calculation would depend on both elastic and electronic interactions between the two. Thompson (1958 and 1960) interpreted some of the annealing stages to be observed after neutron irradiating tungsten in terms of the release of mobile defects from such impurity traps.

We report here some preliminary observations of the annealing of copper alloyed with small quantities of silver, cadmium and beryllium

---

† Communicated by the Author.

after irradiation at $-196°$c with 4 mev electrons. Electrical resistance measurements were used to observe changes in the defect concentration.

§ 2. Experimental Details

Approximately 0·05 atomic % alloys were chosen for these experiments. For such alloys the concentration of solute atoms is sufficiently small to form a homogeneous solid solution, yet considerably greater than the expected point defect concentration introduced by the irradiation.

The compositions of the silver and cadmium alloys were determined chemically; the beryllium alloy was estimated by means of a spectrographic method. The results agreed to within 0·01 atomic % with compositions calculated from measurements at $4·2°$k of the electrical resistivities of the alloys, using Linde's (1939) experimental data of the resistivities of known compositions of dilute copper alloys.

The alloys were examined spectroscopically for trace impurities, and the results of this analysis are presented in table 1.

Table 1.   A spectroscopic analysis of the specimens (in parts per million)

Impurities detected	'Spec Pure' copper	0·05 at. % silver–copper	0·02 at. % cadmium–copper	0·10 at. % beryllium–copper
Fe	1	2	2	5
Ag			40	1
Sn		20	20	
Pb		30	10	
Ni		2	2	
Si		1		1

15 cm of each alloy, in the form of 0·004 in. diameter wire, was wound on a mica frame. Current and potential leads were attached by arc welding in an argon atmosphere, and the whole assembly annealed *in vacuo* for an hour at 550°c. The mica frame was then mounted on a holder for the irradiations and subsequent anneals.

A 4 mev linear accelerator with a maximum beam current of 400 μamp was used for the electron irradiations. Experimentally such an energy is very convenient since the range of electrons is appreciable (about 2 mm in copper); consequently only a small fraction of the energy is dissipated in the sample and the various windows, yet the cross section for defect production is relatively high (about 80 barns).

In order to perform irradiations at $-196°$c, the specimen was continuously bathed in liquid nitrogen inside a pill box. Two thin windows at each end enabled the electron beam to pass right through the box, and so irradiate the specimen. The experimental assembly was rather similar to that used by Meechan and Brinkman (1956).

The resistance of specimens was measured continuously during irradiations to ensure that the temperature did not rise above $-196°$c. Using a steady stream of nitrogen to cool the specimen, beam densities of up to about $50\,\mu$amp/cm^2 could be used.

Since the accelerator delivered a reproducible beam current, it was more convenient to measure the current density immediately after an irradiation. As direct measurement was unreliable owing to secondary emission effects, calorimetric techniques were employed. The beam was allowed to pass through an aperture of known area located in the same position as that of a specimen during irradiation, and then to fall upon a thin-walled calorimeter filled with water. The rise in temperature of the calorimeter for a known irradiation time enabled the current density to be calculated.

All measurements of resistance were performed in liquid helium using standard potentiometer techniques. The relative accuracy of these results was $\pm 10^{-12}\,\Omega$ cm.

Specimens were annealed inside an aluminium block whose temperature could be kept constant to better than $0\cdot1°$c at any predetermined temperature between $-196°$c and $+35°$c.

§ 3. Results

A series of anneals, each of 30 min duration, were performed at successively higher temperatures. The temperature increment between successive anneals was $10°$c, and after each anneal the resistance was measured in liquid helium. This enables the isochronal annealing of the resistivity to be expressed as a function of temperature. However, to depict the annealing stages more clearly it is better to plot the slope of such a curve, dR/dT, as a function of the temperature T. Maximum annealing rates then occur as peaks. In the curves that are presented $\Delta R/\Delta T$, the ratio of the differences in the resistance and temperature measurements between successive anneals rather than dR/dT is plotted as a function of the mean temperature.

Figures 1–4 are these annealing curves for spectroscopically pure copper and dilute alloys of silver, cadmium and beryllium in copper respectively.

Three principal annealing peaks are observed at about $-140°$, $-80°$ and $0°$c in the pure copper. Three peaks are also observed in the dilute alloys, but they are significantly modified.

The exact temperature of the peak occurring around $-140°$c is different for each alloy. The height of this peak is considerably enhanced compared with the others in the silver and cadmium alloys, while with beryllium–copper it is immediately followed by a minimum, with negative values of dR/dT, signifying an increase in resistance as the annealing proceeds.

The $0°$c peak is broadened and occurs at a slightly higher temperature in silver–copper. In cadmium–copper it is broadened so much as to be hardly recognizable. In beryllium–copper the peak is not broadened, but occurs about $20°$ lower; also its size is considerably enhanced.

Fig. 1
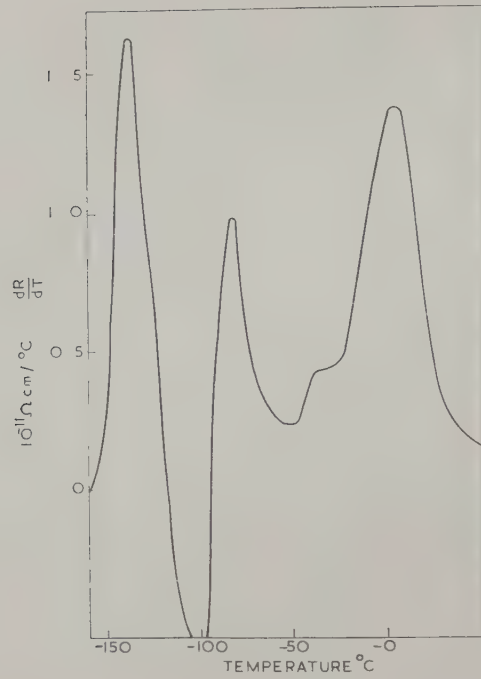
Isochronal annealing of spectroscopically pure copper after electron bombardment at $-196°$c.   Dose $= 3 \times 10^{17}$ electrons/cm².

Fig. 2
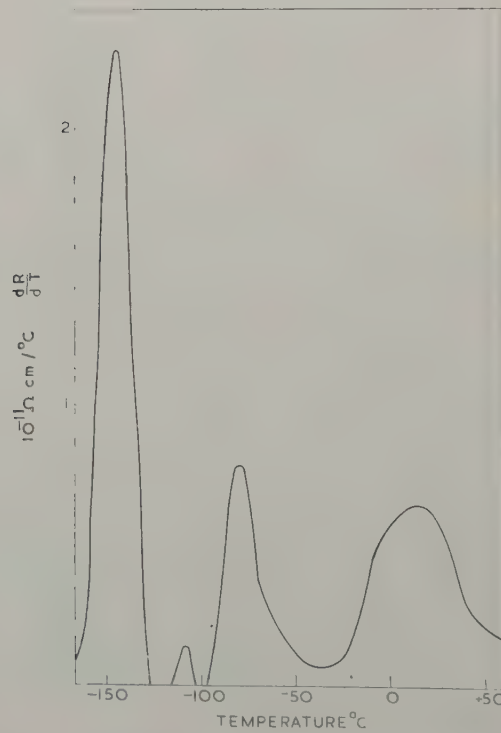
Isochronal annealing of 0·05 atomic % silver–copper after electron bombardment at $-196°$c.   Dose $= 3 \times 10^{17}$ electrons/cm².

Fig. 3
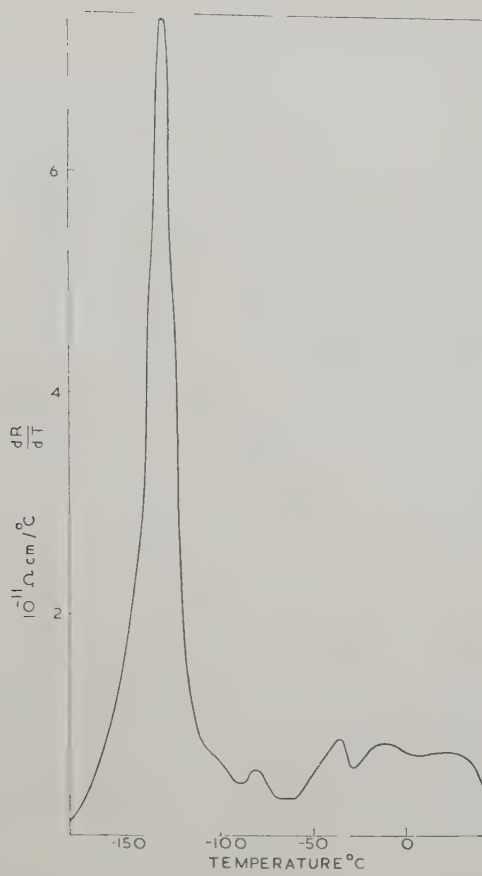
Isochronal annealing of 0·02 atomic % cadmium–copper after electron
bombardment at −196°c.   Dose = 2 × 10¹⁸ electrons/cm².

Fig. 4
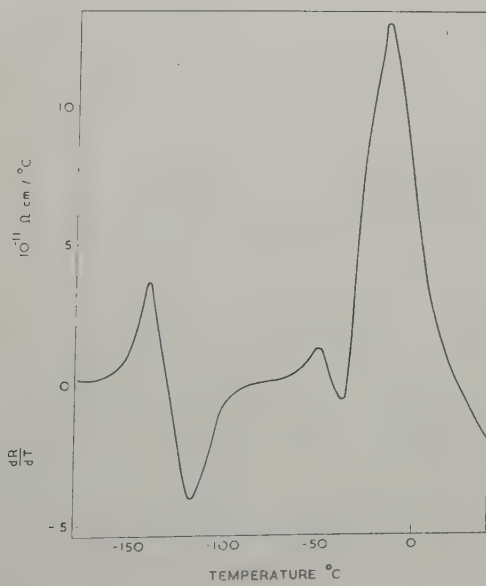
Isochronal annealing of 0·10 atomic % beryllium–copper after electron
bombardment at −196°c.   Dose = 2 × 10¹⁸ electrons/cm².

Certain unsatisfactory features in these experiments should be noted. It was found that the change in resistance introduced in a particular alloy for a certain electron dose was not reproducible. Also many specimens showed little sign during the course of the anneals of recovering to their original pre-irradiation resistance value. It will be observed that in some of the curves the value of dR/dT becomes negative at some temperatures. Apart from the $-120°$C trough in the beryllium–copper these parts of the curves are not reproducible. It is believed that these spurious results are caused by corrosion, even at such low temperatures, for when specimens were removed from the accelerator after an irradiation they were found to be coated with an off-white deposit; after annealing up to room temperature this deposit had disappeared, but the specimens were tarnished. The gaseous product obtained by warming some of this deposit to room temperature was analysed by means of a mass spectrometer. It was found to consist mainly of nitrous oxide, nitrogen peroxide and carbon dioxide and is clearly the result of small quantities of oxygen being present in the liquid nitrogen.

These corrosion effects make detailed comparison in the different alloys uncertain. However, confidence may be placed in the shapes and temperatures of the three principal annealing peaks described above for two reasons. Firstly they are reproducible, and secondly very similar peaks have been observed in the same alloys after neutron irradiation. In these experiments specimens were sealed in an atmosphere of spectroscopically pure helium so that no corrosion effects or anomalies in the resistance were observed.

§ 4. Discussion

The peak which occurs in the region of $-140°$C is sensitive to the presence of small quantities of impurities, the most spectacular effect occurring in the cadmium alloy. It seems reasonable to suggest that this peak is caused by trapping of defects. Since interstitials are believed to anneal at about $40°$K in copper (Holmes *et al.* 1958) they will be highly mobile as soon as they are formed during the irradiation. Many will be annihilated at vacancies and other sinks, but some may be trapped by impurity atoms and only have sufficient energy to be liberated and subsequently annihilated when the temperature is raised to about $-140°$C. Lomer and Cottrell (1955) have discussed such a mechanism whereby defects migrate to sinks via a series of traps. The temperature of the peak maximum is higher in the cadmium than in the silver alloy, indicating that a cadmium atom forms a deeper trap than a silver atom. This is reasonable, since the size difference between a cadmium and a copper atom is half as big again as that between silver and copper. It is, perhaps, not surprising that the appearance of the annealing curve in beryllium–copper is different, because a beryllium atom is smaller than a copper atom, unlike silver and cadmium. The atomic radii of these elements are shown in table 2.

It is by no means obvious whether the release of an interstitial from an impurity trap and its subsequent annihilation will result in a decrease

or an increase in resistivity. If we assume that there is a net increase when the impurity trap is beryllium, then the trough which occurs at $-120°c$ can be compared with the low temperature peaks which occur in cadmium and silver–copper. This leaves unaccounted the peaks which occur in the spectroscopically pure and the beryllium–copper around $-140°c$. In the absence of further experimental evidence these peaks will be attributed tentatively to the release of interstitials from a non-metallic impurity trap, such as oxygen, which occurs in all the copper specimens. A similar sort of explanation is proposed for the $-80°c$ peak, which seems to be little altered in the alloys, apart from beryllium–copper.

Table 2. Atomic radii of elements (from Barrett (1943);
values are for 12-fold coordination)

Element	Radius (Å)
Cu	1·28
Ag	1·44
Cd	1·52
Be	1·13

It is widely believed, and will be assumed here, that the $0°c$ peak is due to the migration of free vacancies (Holmes *et al.* 1958); these will diffuse from lattice sites to impurity traps and sinks. The impurity atoms in the dilute alloys will produce variable strain in the lattice, and consequently the activation energy for migration of a vacancy will depend on its position. Also the number of jumps required for annihilation or trapping will be different in the different alloys. It is not surprising, therefore, that the details of the peak occurring around $0°c$ should differ in the different alloys.

These results can only give a qualitative indication of the influence of impurity atoms on the annealing peaks observed in copper after electron irradiation. A more complete understanding can only be gained by a careful control of various experimental parameters, such as impurity concentration and electron flux. As already mentioned, similar annealing peaks have been observed after neutron irradiation. The greater experimental accuracy and the ease in reproducibility of neutron doses make this type of experiment more feasible with neutrons, and in a future paper the results of such a study will be reported.

REFERENCES

BARRETT, C. S., 1943, *Structure of Metals* (New York: McGraw-Hill), p. 150.

BLEWITT, T. H., COLTMAN, R. R., KLABUNDE, C. E., and NOGGLE, T. S., 1957, *J. appl. Phys.*, **28,** 639.

HOLMES, D. K., CORBETT, J. W., WALKER, R. M., KOEHLER. J. S., and SEITZ, F., 1958, *Proc. Second U.N. Conf. on Peaceful uses of Atomic Energy* (Geneva: United Nations), **6,** 274.

LINDE, J. O., 1939, *Thesis*, Lund. Quoted in *Handbuch der Physik*, 1956, (Berlin: Springer-Verlag), **19,** 210.

LOMER, W. M., and COTTRELL, A. H., 1955, *Phil. Mag.*, **46,** 711.

MEECHAN, C. J., and BRINKMAN, J. A., 1956, *Phys. Rev.*, **103,** 1193.

THOMPSON, M. W., 1958, *Phil. Mag.*, **3,** 421; 1960, *Ibid.*, **5,** 278.

Stress Relaxation in Alpha-Iron at Low Temperatures

By P. Feltham

Department of Metallurgy, The University, Leeds

Abstract

Relaxation of the applied tensile stress σ at strains of up to 2% was studied at 77–358°K in vacuum-annealed iron containing 0·1% of carbon. The relaxation was logarithmic, and the slopes of the curves,

$$s(T) \equiv -d\sigma/d(\log_{10} t),$$

increased from 19·7 kg/cm² at 358°K to 313 kg/cm² at 77°K. The relation

$$Q_j \left(1 - \frac{T}{T_m} \right) = 2·3 \frac{kT}{s} (\sigma_y - \sigma_g),$$

previously derived for stress relaxation in copper, in which T_m is the melting temperature, σ_y the tensile yield stress, and σ_g the temperature independent part of the yield stress, was again found to be applicable, with Q_j, the energy associated with the conservative migration of jogs in edge dislocations, equal to 6·4 kcal/g atom.

§ 1. Introduction

In a recent paper on the stress relaxation and creep of copper and alpha-brasses at low temperatures (Feltham 1961), which we shall subsequently denote by (I), the tensile stress attained after the application of a small plastic strain increment was found to relax from the initial value σ_0 according to the logarithmic law

$$-\Delta\sigma \equiv \sigma_0 - \sigma = s \log_{10} (1 + \nu t), \qquad \cdots \cdots \quad (1)$$

where ν is independent of the time, t. The most characteristic parameter of the relaxation, $s(T)$, given to a good approximation by

$$s = -d\sigma/d \log_{10} t, \qquad \cdots \cdots \cdots \quad (2)$$

increased approximately linearly with decreasing temperature. The relaxation and the associated logarithmic creep were ascribed to slip in which the migration of edge dislocations impeded by the frictional drag of conservatively migrating jogs was rate determining, and the equation

$$Q_j \left(1 - \frac{T}{T_m} \right) = 2·3 \frac{kT}{s} (\sigma_y - \sigma_g) \qquad \cdots \cdots \quad (3)$$

relating Q_j, the energy barrier to jog migration at 0°K, the melting temperature T_m, the tensile yield stress σ_y and the temperature independent part of the yield stress σ_g was derived.

---

† Communicated by the Author.

The main object of the present work was to study the relaxation of stress at low temperatures and small plastic strains in a metal in which the glide dislocations are not dissociated, to examine the applicability of eqn. (3) and, if possible, deduce the magnitude of Q_f.

§ 2. EXPERIMENTAL

It is apparent from eqn. (3) that a high and strongly temperature dependent yield stress could be expected to be associated with comparatively large, easily measurable, values of s at low temperatures, a consideration which prompted the choice of iron containing a small amount of carbon as material for the experiments. Apart from 0·11 wt. % of carbon the principal impurities were 0·5% Mn, 0·02% Si, 0·05% S, 0·03% P and 0·008% N.

Standard specimens with a gauge length of 2·65 cm and 0·317 cm diameter, were machined from rolled rods and annealed *in vacuo* for 8 hours at 1100°C, followed by cooling to room temperature over 24 hours at a nearly constant rate. The resulting grain size was approximately 20 μ.

The cryostat and the coolants used were as in (I); at 85°C a silicon oil bath heated by a tubular immersion heater was employed. Specimens were strained by means of a manually operated Hounsfield tensometer. Stress relaxation was not observed at any given temperature until the (upper) yield-point $\sigma_y(T)$ was reached. Values of σ_y are shown in fig. 1.

In the immediate vicinity of the yield-point, up to about 0·03% of plastic strain, the relaxation of the stress was anomalously rapid and irregular; reproducibility in this range of strains was poor. This behaviour was similar to that exhibited by copper and alpha-brasses at strains within the yield-point elongation, and is exemplified by the broken curve in fig. 2. If, at stresses outside this range, a small strain increment, generally between 0·03 and 0·3% in magnitude, was rapidly applied to the specimen, and the strain subsequently maintained constant, the stress relaxed logarithmically over most of the time over which the relaxation was amenable to observation, i.e. from a few seconds to a few minutes.

After the relaxation due to one strain increment had ceased, a new increment was applied, the relaxation was again recorded, and so on, generally up to total strains of about 2%. Three such characteristic curves, represented as in (1), are shown in fig. 2, in which the lines drawn through the points are parallel; their slope $-\Delta\sigma/d \log_{10} t$ is equal to s at 200°K. Values of s, σ_y and $\sigma_y - \sigma_g$ are shown in the table. The part of the yield stress virtually independent of temperature, σ_g, was taken to be 1420 kg/cm² at all temperatures in the range. This value corresponds to the stress level indicated by the broken horizontal line in fig. 1. Q_f, as well as

$$Q \equiv Q_j [1 - (T/T_m)], \quad . \quad . \quad . \quad . \quad . \quad . \quad (4)$$

evaluated with the aid of the above data, are also given in the table.

Fig. 1
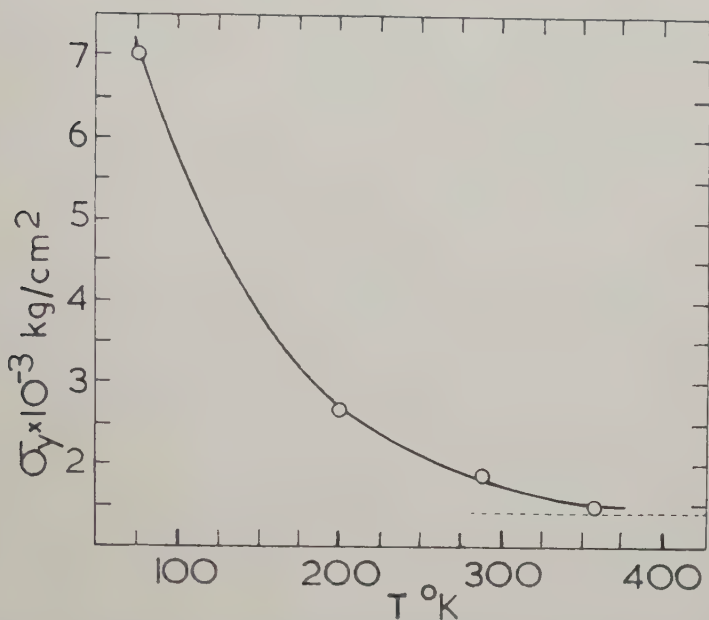
Temperature dependence of the upper yield stress of iron containing 0·11% by weight of carbon.

Fig. 2

Stress relaxation in iron containing 0·11% by weight of carbon (eqn. (1)).
$T = 200°$K.

§ 3. DISCUSSION

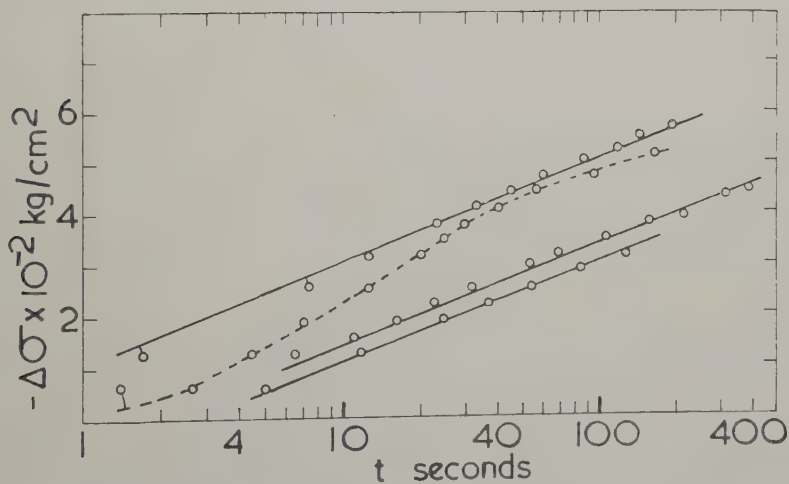The temperature independence of Q_j (table) shows that eqn. (3) is again applicable, as in the case of copper (I). The logarithmic form of the relaxation also suggests that the phenomenon is of the same type in both metals, and is not therefore confined to the face-centred cubic system. Q_j, approximately equal to 6·4 kcal/g atom, is numerically equal to 1·8L, where L is the latent heat of melting (of iron), and thus close to the estimate of 2L proposed for the energy of migration of conservatively moving jogs, on the basis of an analysis of creep data of f.c.c. metals, by Feltham (1957). Activation energies of a similar magnitude, equal to 4·5, 6·4 and 8·0 kcal/g atom for aluminium, silver and platinum, representing 1·8, 2·3 and 1·7 times the latent heats of melting of the respective metals, were also found by Samoilova and Postnikov (1958) to control the rates of decay of the damping capacities in low-frequency torsional oscillations at comparatively low temperatures (e.g. 450°C for Pt), following the removal of tensile loads.

$T°$K	σ_0 kg/cm^2	$\sigma_y - \sigma_g$ kg/cm^2	s kg/cm^2	Q	Q_j
				kcal/gram atom	
77	7000	5580	313	6·30	6·3
200	2650	1230	199	5·68	6·4
288	1860	440	52·3	5·45	6·5
358	1480	60	·19·7	5·00	6·2

These activation energies are too small to be ascribed to the formation or migration of point defects. Similarly, they cannot represent the energy of formation of jogs by the intersection of dislocations, for the usual estimates yield 50–250 kcal/g atom per elementary jog in alpha-iron.

However, the observed values of Q_j could be associated with recovery processes involving limited rearrangements of dislocations, controlled by the frictional drag of conservatively migrating jogs, as proposed in (I).

The results on the effect of alloying on the relaxation in the Cu–Zn system (I) suggest that values of Q_j slightly different from the one obtained in the present work might be deduced from the relaxation in iron of high purity.

ACKNOWLEDGMENT

REFERENCES

FELTHAM, P., 1957, *Phil. Mag.*, **2**, 584 ; 1961, *Ibid.*, **6**, 209.
SAMOILOVA, A. YA., and POSTNIKOV, V. S., 1958, *Fiz. Metal. Metalloved.*, **6**, 124.

The Half-life of Long-lived Lutetium-176†

By A. McNair

Atomic Weapons Research Establishment, Aldermaston, Berkshire

Abstract

The half-life of the odd–odd naturally occurring isotope lutetium-176 is shown to be $(3\cdot6\pm0\cdot1)\times10^{10}$ years, from independent measurements both of the rate of gamma and of electron emission.

§ 1. Introduction

THE mode of decay of naturally occurring ^{176}Lu was first proposed by Goldhaber and Hill (1952) and largely confirmed by more recent work (Arnold and Sugihara 1953, Arnold 1954, Dixon *et al.* 1954, Glover and Watt 1957). The nucleus appears to decay (figure) by negatron emission from the ground state, whose spin has been measured as 6 ± 1 or greater (Schuler and Gollnow 1939, Steudel 1958), to the $6+$ rotational state of the strongly deformed nucleus ^{176}Hf, followed by a gamma cascade successively through the $4+$ and $2+$ rotational states to the ground state. A parallel path by electron capture to ^{176}Yb is theoretically possible but calculations based on the most recent mass formulae of Levy (1957) suggest that the energy available for decay would not permit a transition to other than the first $2+$ excited state of ^{176}Yb. Such a transition would be two orders more forbidden than the negatron decay and would be completely masked by it. The branching ratio is now agreed to be very small (Arnold 1954, Dixon *et al.* 1954, Glover and Watt 1957).

The half-life of ^{176}Lu has been obtained from the rate of gamma ray emission and determined to be near $2\cdot1\times10^{10}$ years (Arnold 1954, Glover and Watt 1957). This appears to be confirmed by Herr *et al.* (1958) who found the half-life to be $(2\cdot17\pm0\cdot35)\times10^{10}$ years by measuring the amount of ^{176}Lu and radiogenic ^{176}Hf in a gadolinite mineral whose age was determined by standard methods. On the other hand, Dixon *et al.* (1954) derived the half-life of ^{176}Lu from the beta particle emission rate and claimed $(4\cdot6\pm0\cdot3)\times10^{10}$ years. This value depended on a rather complex analysis of the beta spectrum, which was measured in 2π geometry from a thick source support, and was later recalculated on the basis of newer values for the saturation back-scattering of electrons from source supports to give a half-life of $(4\cdot1\pm0\cdot2)\times10^{10}$ years (McNair 1956). No reasonable assumptions, however, could bring the half-life as low even as 3×10^{10} years. Glover

---

† Communicated by the Author.

and Watt (1957) indicated that their beta experiments showed evidence
of radioactive contamination in the sample of Lu_2O_3, so that the beta half-
life quoted by them, $2\cdot8 \times 10^{10}$ years, must be regarded as a lower limit.
This is markedly longer than their gamma half-life.

Thus there appears to be a very real discrepancy (which seems to depend
on whether the beta or the gamma radiation is measured) in the half-lives
reported for [176]Lu and the chance that this might indicate an undiscovered
factor in the decay of [176]Lu led us to re-examine the isotope. The possible
use of the isotope as a geochronological marker in special cases is an added
reason for attempting to get an accurate picture of the decay and half-life.

§ 2. METHOD

It was decided that the half-life should be measured by looking both at
the gamma emission and at the particle emission rates to see if any difference
arose. As pointed out by Glover it is difficult to obtain samples of Lu_2O_3
which are radioactively absolutely pure, so the method which was used
to obtain the half-life from gamma emission was chosen to be as specific
for the [176]Lu decay as possible. It depends on the fact (see figure) that
gammas (γ_3) from the $6+$ to $4+$ transition are in coincidence with the
$4+$ to $2+$ transition gammas (γ_2); the $2+$ to ground state transition goes
almost completely by internal conversion and does not affect the argument.
A single well-type sodium iodide crystal was used as a gamma spectrometer
and showed three total absorption peaks corresponding to γ_2, γ_3 and $\gamma_2 + \gamma_3$
(neglecting x-rays from various possible internal conversions). It is
easily shown (Shapiro and Higgs 1957) that if N_3 is the area under the γ_3
photopeak, N_2 the area under the γ_2 peak and N_c the area under the
coincidence ($\gamma_2 + \gamma_3$) peak then the total number of disintegrations N,
assuming the decay scheme in the figure, is given by

$$N = N_c \left(\frac{N_3}{N_c} + \frac{1}{f_2} \right) \left(\frac{N_2}{N_c} + \frac{1}{f_3} \right)$$

where the f factors are the photo fractions for the corresponding gamma ray
energy, i.e. the fraction of the gamma rays actually detected in any particu-
lar experimental arrangement which appears in the total absorption peak.

The use of this particular method of measuring the disintegration rate has
many advantages. The necessary apparatus is simple, one amplifier and a
kick-sorter. No coincidence circuits are required since the coincidences
are automatically distinguished by the scintillation counter itself. It is not
necessary to calibrate the system with standardized gamma sources and the
result is not affected by the existence of a proportion of internal conversion in
the γ_3 and γ_2 transitions nor by absorption in the source or in any absorbers
that may be present. The only subsidiary measurements which are required
are the determinations of f. This factor obviously depends on the source
and absorber and on the size of the crystal. It must be measured in
exactly the same experimental arrangement, but unstandardized sources of
single gamma transitions of various energies are all that are required.

The particle emission rate was determined in a large source area 4π proportional counter described elsewhere (McNair and Wilson 1961). Since each beta particle is followed in coincidence by at least one internal conversion electron (from the γ_1 transition) the effective absorption of the source and its supporting foil is negligible provided the total thickness is small relative to the range of the conversion electron of lowest energy.
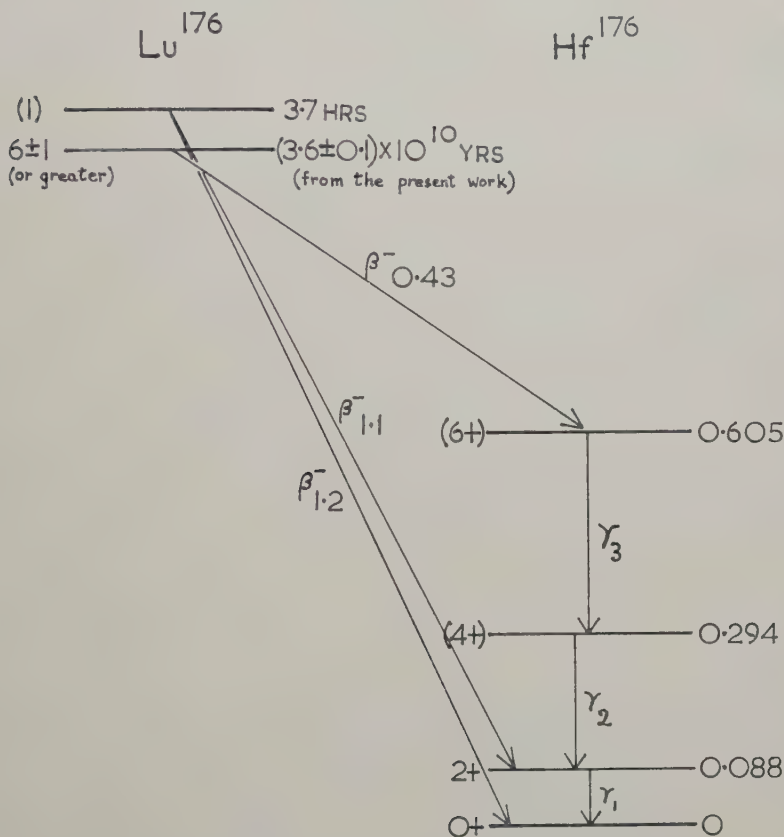
The decay scheme of ^{176}Lu (after Goldhaber and Hill 1952).

§ 3. APPARATUS

The scintillator was a $2\frac{1}{2}$ in. $\times 2\frac{1}{2}$ in. cylinder of NaI (Tl) with a $\frac{1}{2}$ in. diameter well. The source material was lutetium oxide of Johnson Matthey "Specpure" grade and was contained in a 1/10 in. thick copper crucible to absorb the K x-rays of Hf arising from internal conversion transitions, since the presence of peaks from these x-rays complicates the analysis of the gamma spectrum. The photo fractions were determined using the gamma rays from ^{141}Ce (142 kev), ^{203}Hg (279 kev), ^{51}Cr (323 kev) and ^{137}Cs (662 kev). The sources were contained in similar copper absorbers and mixed with tungsten metal powder to simulate scattering in the lutetium oxide source. f_2 and f_3 were then found by interpolation to the correct energies.

§ 4. Results

Four separate measurements using the γ–γ single crystal coincidence technique were made on two different types of kicksorter. These experiments gave half-lives which agreed to within 2% of their mean value of $3 \cdot 6 \times 10^{10}$ years. This is itself considerably higher than previous measurements of the half-life from gamma ray intensities.

Two 4π beta measurements were made on two different sources, one $\sim 400 \, \mu\mathrm{g/cm^2}$ and the other $\sim 200 \, \mu\mathrm{g/cm^2}$ both deposited on $\sim 200 \, \mu\mathrm{g/cm^2}$ aluminium foil. Both sources gave count rates which corresponded to a beta half-life of $(3 \cdot 2 \pm 0 \cdot 1) \times 10^{10}$ years.

A third measurement was made when, at a later date, a $4\frac{1}{2}$ in. $\times$ $4\frac{1}{2}$ in. sodium iodide well crystal became available. The efficiency of this crystal for either of the two gamma rays from ^{176}Lu is very high and when both gammas are in coincidence as in this case the effective efficiency is greater than 99%. In this experiment the source was contained in a thin-walled glass phial to allow the escape of K x-rays from the source providing for even higher detection efficiency. The high probability of detecting each decay was confirmed by the complete absence of a singles peak of Hf K x-rays whose emission would be expected in some of the internal conversion events. This proved that one or other of the gamma transitions was always observed. The half-life calculated from this experiment, simply by totalling the number of counts recorded in the gamma spectrum span, was $(3 \cdot 57 \pm 0 \cdot 02) \times 10^{10}$ years. This was in excellent agreement with the previous γ–γ measurement of the half-life.

§ 5. Discussion

Both methods which depend on measuring the rate of emission of gamma rays from the source give the same value for the half-life of ^{176}Lu viz. $(3 \cdot 6 \pm 0 \cdot 1) \times 10^{10}$ years, assuming $2 \cdot 6\%$ isotopic abundance and allowing a generous estimation of the error to cover all possible contingencies. However, the half-life obtained from the 4π beta measurements is lower by an amount which is statistically significant. The difference is almost certainly to be explained by very slight alpha-active impurities which were noted, even in Specpure material, by Glover and Watt (1957) and also in one of our samples. So, we can say only that the beta experiment shows that the half-life of ^{176}Lu cannot be less than $3 \cdot 2 \times 10^{10}$ years. This would confirm Glover and Watt's beta half-life of $2 \cdot 8 \times 10^{10}$ years as a minimum value†. Our gamma measurements are much more specific against contaminants than are the beta measurements, which were based on integral count rates.

---

† Some, if not all, of the alpha contamination comes from the thorium radioactive series. It can readily be shown that the amount of alpha and beta activity required to reduce the apparent beta half-life of ^{176}Lu from 3·6 to $3 \cdot 2 \times 10^{10}$ years will have associated with it too few gamma rays in the 100–600 kev range to have any appreciable effect on the half-life calculated from the gamma ray measurements.

Therefore we feel that the gamma half-life is the true value and the discrepancy between the present beta and gamma measurements requires no other explanation.

The difference between the new value $(3 \cdot 6 \pm 0 \cdot 1) \times 10^{10}$ years and the value quoted by Dixon *et al.* (1954), later revised downwards (McNair 1956) to $(4 \cdot 1 \pm 0 \cdot 2) \times 10^{10}$ years is not thought to be significant because of the rather complicated analysis which was required to derive the half-life in these former investigations. It is rather more difficult to see why there is such a difference between the present value and that of Glover and Watt $(2 \cdot 1 \pm 0 \cdot 2) \times 10^{10}$ years, and Arnold $(2 \cdot 15 \pm 0 \cdot 10) \times 10^{10}$ years, both of which were obtained from the gamma ray intensities. In the former the efficiency of the crystal for the gamma rays of ^{176}Lu was calculated from a measured efficiency for the $1 \cdot 46$ mev gammas of ^{40}K. This is rather a large extrapolation and could be expected to introduce some error. In Arnold's work the geometrical efficiency was rather low ($5 \cdot 4\%$) and was derived from a calculated standard geometry. Source self-absorption was estimated by interpolation from tables and the stopping power of the crystal and photo peak efficiency were obtained from published work rather than from direct measurement. As pointed out earlier, the detection efficiency of the system is not required in the present gamma measurement.

Herr *et al.* (1958) in their determination of the half-life from geological samples arrived at a half-life of $(2 \cdot 17 \pm 0 \cdot 35) \times 10^{10}$ years which is also low compared with the present value. In principle the geological method is the perfect way of obtaining these long half-lives, but in practice, for Lu and Hf, the procedures are extremely difficult and there exists the possibility of introducing errors in the many stages in the experiment. It will be interesting to await the results of future geological measurements of this isotope.

The $\log ft$ value for the negatron decay of ^{176}Lu is $\sim 18 \cdot 8$, which would normally classify the transition as third forbidden (3 or 4, yes). However, it seems likely on theoretical considerations (Gallagher and Moszkowski 1958) that the ground state of ^{176}Lu is $7-$, which would imply a (1, yes) first forbidden transition to the $6+$ state of ^{176}Hf. The large retardation factor is now generally attributed to the high order of K-forbiddenness ($K = 7$ to $K = 0$) involved in the transition (Gallagher 1960).

§ 6. Conclusions

We conclude that the half-life of the naturally occurring odd–odd isotope ^{176}Lu is

$$(3 \cdot 6 \pm 0 \cdot 1) \times 10^{10} \text{ years}$$

determined by two different gamma ray measurement techniques and confirmed by a lower limit of $3 \cdot 2 \times 10^{10}$ years from 4π beta counting.

Acknowledgments

REFERENCES

ARNOLD, J. R., 1954, *Phys. Rev.*, **93,** 743.

ARNOLD, J. R., and SUGIHARA, T., 1953, *Phys. Rev.*, **90,** 332.

DIXON, D., MCNAIR, A., and CURRAN, S. C., 1954, *Phil. Mag.*, **45,** 683.

GALLAGHER, C. J., 1960, *Nucl. Phys.*, **16,** 215.

GALLAGHER, C. J., and MOSZKOWSKI, S. A., 1958, *Phys. Rev.*, **111,** 1282.

GLOVER, R. N., and WATT, D. E., 1957, *Phil. Mag.*, **2,** 699.

GOLDHABER, M., and HILL, R. D., 1952, *Rev. mod. Phys.*, **24,** 222.

HERR, W., MERZ, E., EBERHARDT, P., and SIGNER, P., 1958, *Z. Naturf.* A, **13,** 268.

LEVY, H. B., 1957, *Phys. Rev.*, **106,** 1265.

MCNAIR, A., 1956, Thesis, University of Glasgow.

MCNAIR, A., and WILSON, H. W., 1961, *Phil. Mag.*, **6,** 563.

SCHULER, H., and GOLLNOW, H., 1939, *Z. Phys.*, **113,** 1.

SHAPIRO, P., and HIGGS, R. W., 1957, *Rev. sci. Instrum.*, **28,** 939.

STEUDEL, A., 1958, *Z. Phys.*, **152,** 599.

Some Electrical Resistivity Measurements on a Series of Iron-Chromium Alloys

By R. W. Powell, R. P. Tye and Margaret J. Woodman

National Physical Laboratory, Teddington

Abstract

Results are presented for the electrical resistivities of iron and five iron–chromium alloys of up to 5·58% chromium content, at temperatures ranging from that of liquid helium to above the alpha–gamma transformation of each sample. Both the temperature of transformation and the consequent decrease in apparent electrical resistivity (neglecting dimensional changes) are approximately linear functions of the chromium content. For the series studied the transformation temperature decreases from about 910°c to 850°c, whilst the decrease in resistance increases from about 0·8 to 2·2%. Hysteresis is observed on cooling.

Arising from an enquiry by Professor N. F. Mott, F.R.S., concerning the electrical resistivity of binary alloys of iron in the transformation region, the determinations now reported for some iron–chromium alloys have been carried out.

The pure iron and alloys of iron with chromium used in this work were rods of 1·24 to 1·35 cm diameter and approximately 10 cm long prepared in the Metallurgy Division of the National Physical Laboratory at the time when studies were being made of the tensile and impact properties of iron and iron alloys (Rees *et al.*, 1951, 1954). The samples were cut from rods 25 cm long, leaving specimens of a suitable length for subsequent thermal conductivity determinations. Their chemical analyses are given in table 1.

The conventional potential-drop method was used for the electrical resistivity determinations; the two thermocouples, which were welded on to each rod at points about 4 cm apart, provided the potential leads and heavy copper current leads were joined to the free ends of each rod. For the range above room temperature the samples were connected in pairs and enclosed in an evacuated ceramic tube which was mounted centrally within a horizontal wire-wound furnace. In some initial runs the measurements were made at a series of steady temperatures during heating to about 850°c to 900°c and at a few temperatures whilst cooling back to room temperature. In each instance the initial and final values of the electrical resistivity at room temperature agreed closely. The transformation region was later explored by a similar method, but with the temperature slowly varying at the rate of about 1°c in 4 min and with

Table 1. Chemical analyses in weight per cent of iron and five iron–chromium alloys

Element	Identification Number: 18AF3	38AF3	38AF2	38AF1	37AF3	37AF2
Carbon	0·0058	0·0028	0·0038	0·0046	0·0042	0·0030
Silicon	0·004	0·003	0·003	0·004	0·003	0·014
Manganese	0·004	<0·005	n.d.	n.d.	n.d.	n.d.
Sulphur	0·003	0·0048	0·0045	0·0048	0·0039	0·0042
Phosphorus	<0·001	<0·001	n.d.	n.d.	n.d.	0·001
Nickel	0·007	0·006	n.d.	n.d.	n.d.	0·005
Chromium	0·002	1·20	2·32	3·37	4·12	5·58
Copper	0·007	0·003	n.d.	n.d.	n.d.	0·003
Aluminium	<0·001	0·001	0·001	0·001	0·001	0·0015
Molybdenum		n.d.†	n.d.†	n.d.†	n.d.†	n.d.†
Oxygen	0·0008	0·002	0·0024	0·0021	0·0032	0·0022
Nitrogen	0·0023	0·0008	0·0014	0·0012	0·0013	0·0016
Hydrogen	<0·000005	<0·000005	<0·000005	<0·000005	<0·000005	<0·000005

n.d. = not determined.

n.d.† = not determined, but no molybdenum was detected spectrographically in the Swedish-iron base or the chromium from which these alloys were made.

observations being continuously made. Care was taken to ensure that the specimens were so placed that the two attached thermocouples indicated temperatures agreeing to within about 0·1°C of the mean recorded temperature.

All measurements were made on a vernier potentiometer reading to microvolts, and the sequence observed alternately for each specimen was, emf of each thermocouple, emf across standard resistance, e.m.f. across the platinum limbs of each thermocouple, and e.m.f. across the platinum–rhodium limbs of each thermocouple. These readings were then repeated in the reverse order but with the direction of the measuring currents reversed. The sum of the e.m.f.'s obtained for the two current directions for the different thermocouple limbs usually agreed to within about 4 μv in 2000 μv. This procedure enabled values of the electrical resistivity to be obtained for each rod at temperature intervals of about 2°C.

Subsequently the diameters of the specimens were reduced and the work was extended to lower temperatures, measurements being made with the specimens immersed in melting ice, liquid helium, liquid hydrogen and liquid nitrogen and during warming up after immersion in the nitrogen.

In deriving electrical resistivities from these measurements the room temperature dimensions of the rods have been used and no attempt has been made to allow for temperature variations of these dimensions.

Table 2. Variation of electrical resistivity (microhm cm²/cm) of iron–chromium alloys with temperature

Metal / Temperature °C	−269	−252·8	−195·8	0	200	400	600	800
Iron	0·25	0·26	0·82	9·1	21·4	41·0	68·2	106·4
Iron +1·2% Cr	2·62	2·72	4·06	14·1	27·0	46·6	71·9	107·0
,, +2·32% Cr	4·65	4·71	6·45	18·4	32·4	51·0	75·9	107·4
,, +3·37% Cr	6·61	6·65	8·56	22·0	37·4	56·2	80·0	108·9
,, +4·12% Cr	8·08	8·08	10·09	25·4	40·4	59·8	81·4	109·8
,, +5·58% Cr	10·57	10·56	12·47	28·7	45·4	64·4	85·7	110·6

Table 2 contains the results at the four low temperatures and from 200° to 800°C as read at 200°C intervals from curves drawn through the observational points on a resistance–temperature plot. It will be seen that the resistivity of the two alloys of highest chromium content had attained constant values by liquid hydrogen temperature, but that the resistivities of the other samples decreased by from 0·6% for the alloy of 3·37% chromium content to 4% for the pure iron on further cooling to the temperature of liquid helium. The residual resistance would

appear to be an approximately linear function of the chromium content,
except that the value for the alloy of 5·58% chromium content is some
5% below the linear prediction.   At most other temperatures the alloys
of lower chromium content obey a fair linear correlation, whereas the
point for the alloy of 5·58% chromium content is again displaced below
the line.   The experimental points obtained during heating and cooling
through the alpha-gamma transformation regions are plotted in the figure.
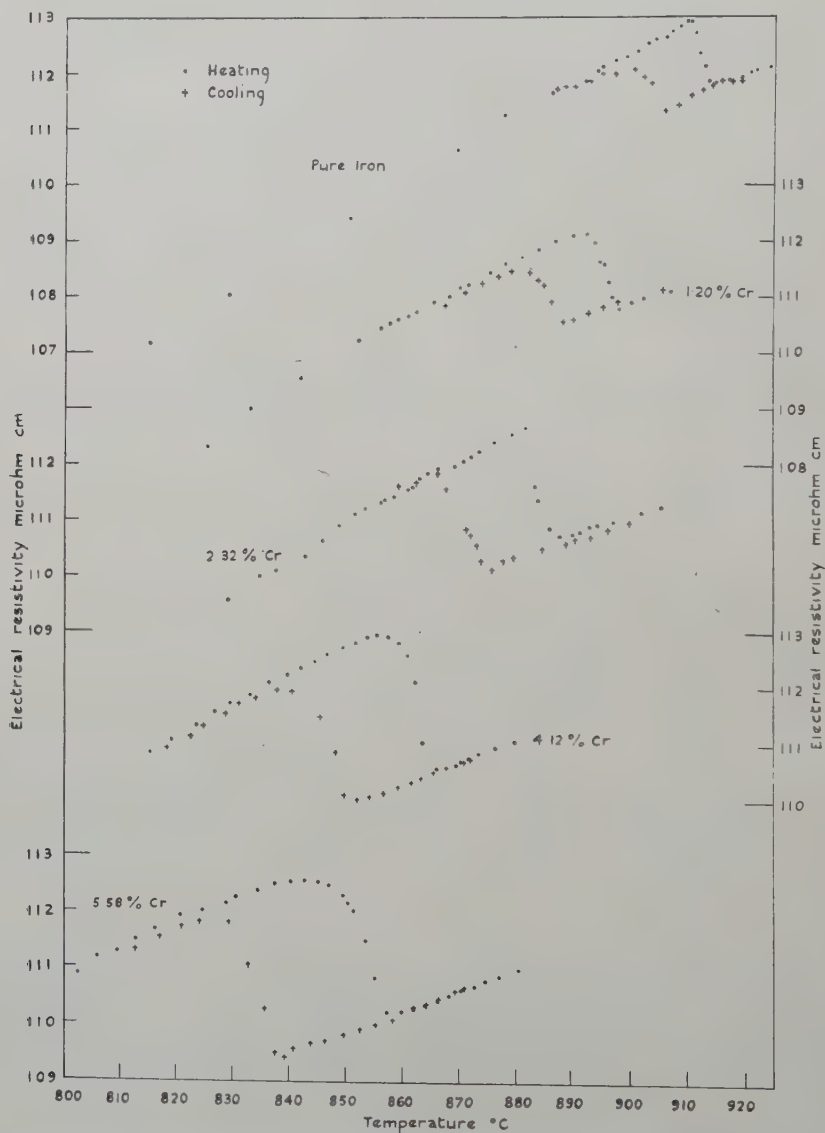
Electrical resistivity versus temperature for a pure iron and four iron-chromium
binary alloys in the transformation region.

On heating, the resistivities for the alpha-phase are seen to attain maximum values which all lie between 112 and 113 microhm cm²/cm, and, on transformation, fall sharply by amounts which increase approximately linearly with chromium content from about 0·8% for iron to about 2·2% for the alloy containing 5·58% of chromium. The temperature at which the change occurs decreases approximately linearly with chromium content from about 910°c for iron to about 850°c for the alloy of 5·58% chromium content.

On cooling, the resistivity curves all show clear evidence of hysteresis, and this also tends to become more pronounced as the alloy content is increased. In each instance the cooling curve ultimately agrees closely with the heating curve. That this should be true for the sample of high purity iron would appear to be somewhat fortuitous since other workers have reported the occurrence of varying length changes on cooling back through the transformation. These have in the main been increases in length (Benedicts 1914, Austin and Pierce 1934, Wells *et al.*, 1936) but a decrease has also been noted (Souder and Hidnert 1922).

In this connection, one of the present authors (R.W.P.), when studying the electrical resistivity of another sample of pure iron, observed positive displacements of the resistivity curve after each cooling through the gamma to alpha transformation. Each such temperature cycle was found to cause the length of the sample to increase by about ½% and the diameter to suffer a corresponding reduction.

Note by Professor Mott.—The small change, about 0·8%, in the electrical resistance of iron at the α–γ transition leads one to suppose that the form of the Fermi surface, which is one factor affecting the electrical resistance, is relatively independent of crystal structure. Since the wave-functions at the Fermi surface may well contain a considerable admixture of 3d orbitals so that a dependence of amplitude on direction in the cubic lattice is possible, such a conclusion would be of considerable interest. It would also imply that the mean vibrational frequency and also the magnetic moment per atom are unchanged.

Dr. Powell's measurements show that the admixture of 5·58% of chromium increases the change in the electric resistance to 2·2%. This suggests that the very small change for pure iron is perhaps accidental and that one cannot in general conclude that the change in the form of the Fermi surface is very small.

REFERENCES

AUSTIN, J. B., and PIERCE, JR., R. H. H., 1934, *Trans. Amer. Soc. Metals*, **22,** 447.
BENEDICTS, C., 1914, *J. Iron St. Inst.*, **89,** 419.

REES, W. P., HOPKINS, B. E., and TIPLER, H. R., 1951, *J. Iron St. Inst.*, **169,** 157; 1954, *Ibid.*, **177,** 93.
SOUDER, W., and HIDNERT, P., 1922, *Sci. Pap. U.S. Bur. Stand.*, **17,** 611.
WELLS, C., ACKLEY, R. A., and MEHL, R. F., 1936, *Trans. Amer. Soc. Metals*, **24,** 46.

Reinterpretation of Discordant X-ray Results for the Debye Temperature of Silver

By F. H. Herbstein

National Physical Research Laboratory, Council for Scientific and Industrial Research, Pretoria, South Africa

Abstract

The values given in the literature for the Debye temperature of silver as a function of temperature have been derived from measurements of elastic constants and from the temperature variation of Bragg intensities. The results from the different experimental techniques are not in good agreement. However, it is shown that reinterpretation of the x-ray measurements (by a method due to Chipman (1960)) gives new values which agree satisfactorily with the elastic-constant values.

THE Debye temperature of silver has been determined as a function of temperature by a number of workers, using different experimental methods. These results are summarized in fig. 1, where the values are given in terms of Θ_D, the Debye temperature appropriate to specific-heat or elastic-constant measurements[†]. The results from measurements of Young's modulus (Koster 1948) and single-crystal elastic constants (Neighbours and Alers 1958) are in good agreement over the temperature range where comparison is possible. In addition Alers and Neighbours (1959) have shown that the specific-heat and elastic-constant values of Θ_D are in excellent agreement at $0°\text{K}$. On the other hand the values reported from four independent sets of x-ray measurements (Andriessen 1935, Boskovits *et al.* 1958, Spreadborough and Christian 1959, Haworth 1960) are not all in good mutual agreement and also differ appreciably from the results of the other methods. The purpose of the present note is to show that three of these sets of x-ray results can be reinterpreted to give new values of Θ_D which are in reasonably good agreement with those from other sources.

The same general experimental procedures were used in all four sets of x-ray measurements, the intensities of selected Bragg reflections being measured over a range of temperatures. The most reliable results appear to be those of Haworth, who used a diffractometer, measured integrated as well as peak intensities and allowed for the temperature-diffuse contributions to the Bragg peaks (Chipman and Paskin 1959). For a monatomic

---

† Θ_M, the Debye temperature appropriate to diffraction measurements, is converted to Θ_D by the equation $\Theta_D = 0\cdot964\ \Theta_M$ (see Zener and Bilinsky 1936, James 1950, Chapter V).

Fig. 1
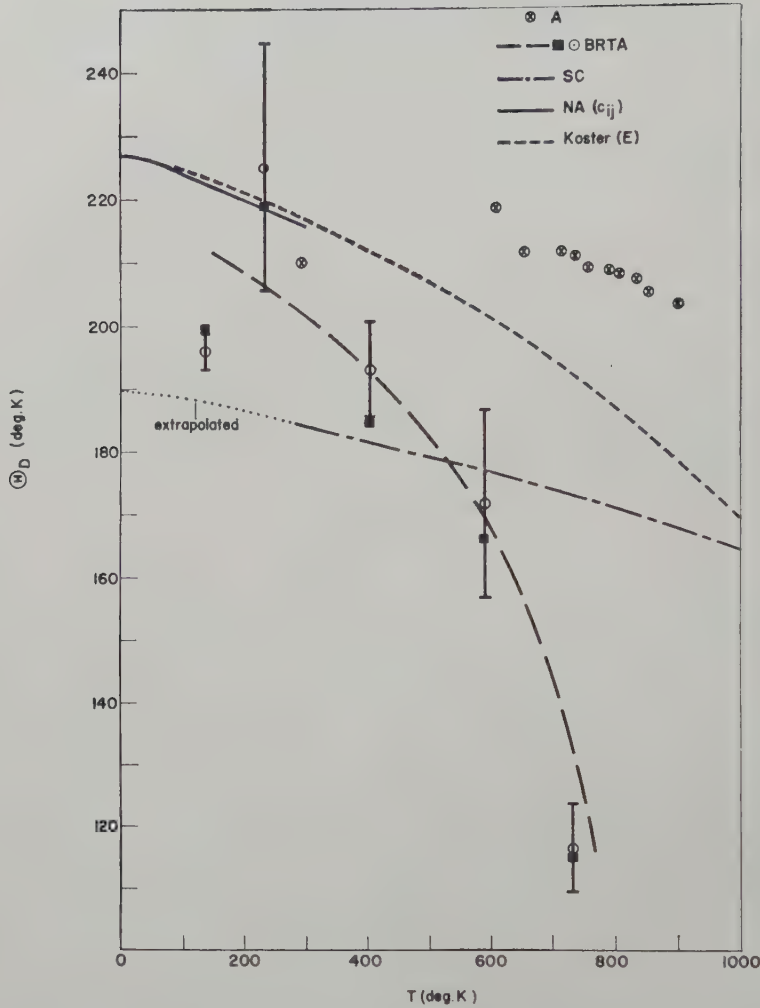
Variation of Debye temperature Θ_D with temperature according to various
workers (A, Andriessen 1935; BRTA, Boskovits *et al.* 1958; SC, Spread-
borough and Christian 1959; NA Neighbours and Alers 1958, Koster
1948). Haworth's results (1960) run parallel to the SC curve but with
$\Theta_D = 190°$K at $T \sim 300°$K; they have been omitted to preserve clarity.

cubic crystal the Debye–Waller theory leads to the following expression
for the ratio of the integrated intensities of a particular reflection at two
temperatures T_1, T:

$$\frac{\lambda^2}{\sin^2\theta}\ln\frac{\rho(T_1)}{\rho(T)} = \frac{12h^2}{mk}\left\{\frac{T\psi(x)}{\Theta_M{}^2(T)} - \frac{T_1\psi(x_1)}{\Theta_M{}^2(T_1)}\right\}. \quad \cdot \quad \cdot \quad \cdot \quad (1)$$

Here $x = \Theta_M/T$ and $\psi(x)$ is the Debye function

$$\frac{1}{x}\int_0^x \frac{u\,du}{e^u - 1} + \frac{x}{4}.$$

The other symbols have their usual meanings. Equation (1) does not take into account changes in geometrical correction factors, etc. due to thermal expansion. The equation has been given here in its approximate form because the effects of thermal expansion were neglected in the papers considered; errors from this source would be expected to be small compared with errors of measurement. The published results have been used to calculate $(\lambda^2/\sin^2\theta)\ln[\rho(T_1)/\rho(T)]$ at a set of convenient values of T, T_1 being kept fixed at $300°$K. These results are shown in fig. 2,

Fig. 2
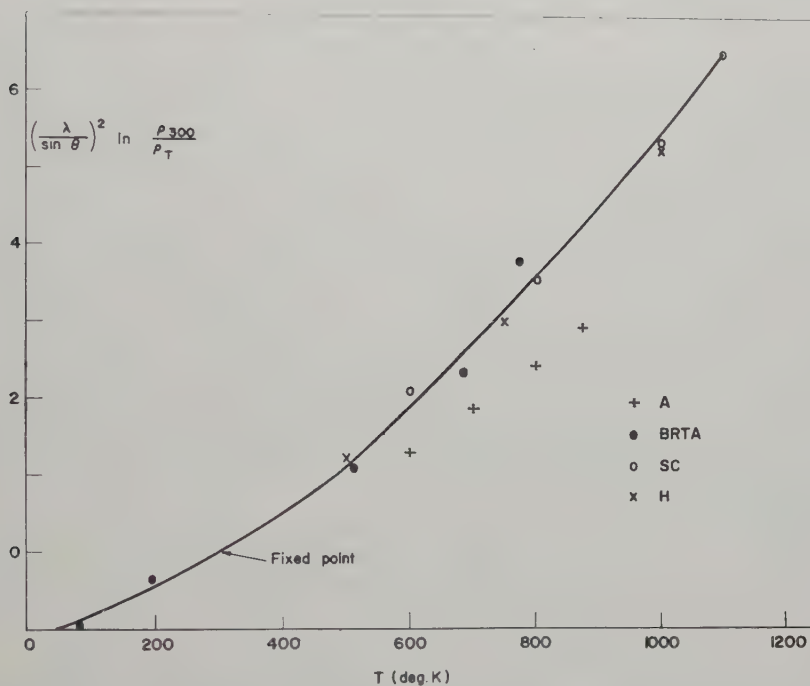
Comparison of results of x-ray intensity measurements by various workers. The results plotted here were recalculated from those given in the original papers (H, Haworth 1960; otherwise see caption of fig. 1 for references).

where it will be seen that a smooth curve can be drawn through the points from the measurements of Boskovits *et al.*, Spreadborough and Christian, and Haworth. Andriessen's results lie systematically below this curve and have not been included in the calculations described below.

Equation (1) contains two unknowns $\Theta_M(T_1)$ and $\Theta_M(T)$ and can thus be solved only with the aid of additional information or special assumptions. Boskovits *et al.* and Andriessen derived Θ_M by comparing intensities at small temperature intervals and assuming that Θ_M was constant over the

temperature range considered.   The success of this method is critically dependent on the accuracy of the intensity measurements used: for example the very low value given by Boskovits *et al.* for Θ_M at 730°K (see fig. 1) is due to the cumulative effects of inaccuracies in the intensity measurements at 685°K and 775°K (see fig. 2).

An alternative method is to assume a particular temperature dependence for $\Theta_M(T)$ and thus eliminate one of the unknowns of equation (1).   This method was first proposed by Zener and Bilinsky (1936), who derived an expression for the temperature dependence of Θ_M assuming that changes of Θ_M with T were due to thermal expansion only.   Zener and Bilinsky's expression contains some rather inaccessible quantities and a more convenient equation, using the same assumption, has been given by Paskin (1957).   This is:

$$\frac{\Theta_M(T)}{\Theta_M(T_1)} = \left[\frac{V(T_1)}{V(T)}\right]^{\gamma} \qquad . \quad . \quad . \quad . \quad . \quad . \quad (2)$$

where $V(T_1)$, $V(T)$ are the atomic volumes at T_1 and T respectively and γ is Gruneisen's constant ($= 2 \cdot 40$ for silver).   Haworth has used Paskin's method to recalculate values of Θ_D at 300°K from the x-ray diffraction results listed previously and obtained the values given in the table.   The last three values agree well among themselves, as would be expected from the comparison of the experimental data in fig. 2, but differ appreciably from the values derived from elastic-constant and specific-heat measurements.   Although the value derived from Andriessen's x-ray data is in good agreement with the values from specific-heat and elastic-constant measurements, it has already been indicated that his experimental data are unreliable.   These facts strongly suggest that a method is needed for analysing the experimental data without forcing a particular temperature dependence on Θ_M.   Such a method has recently been proposed by Chipman (1960).

Values of Θ_D derived from different sets of x-ray measurements by use of eqn. (2) (Haworth 1960)

Θ_D at 300°K	Reference
°K	
230 ± 5	Andriessen (1935)
181 ± 12	Boskovits *et al.* (1958)
184 ± 8	Spreadborough and Christian (1959)
190 ± 6	Haworth (1960)

Chipman pointed out that the curve of Θ_M against T obtained by solving equation (1) for a particular set of experimental results depended on the value assumed for $\Theta_M(T_1)$ (the value of Θ_M at some standard reference temperature, here taken as 300°K).   Curves plotting Θ_M against T are calculated for a range of values of Θ_M (300) and that value of

Θ_M (300) chosen which gives the curve with the most reasonable shape (see Chipman (loc. cit.) for discussion of this point). Experimental data at fairly low temperatures are required for the method to work satisfactorily, as the curves differ appreciably in shape only in the region where $T < \Theta_M$. The results of such a calculation are shown in fig. 3, the experimental results having been taken from the smooth curve of fig. 2. A value of Θ_M (300) = 218°K was chosen from fig. 3. Values of Θ_M (300) from the table give curves of quite unreasonable shape. The curve of Θ_D against T obtained from these calculations is shown in fig. 4 together with the results derived from elastic constants: the two curves agree reasonably well over the whole temperature range investigated. These results show that for Ag the temperature variation of Θ_M is not due to volume changes alone. Similar behaviour is found for Al (Chipman, loc. cit.), the only other element for which satisfactory experimental measurements are available over a wide range of temperature.

Fig. 3
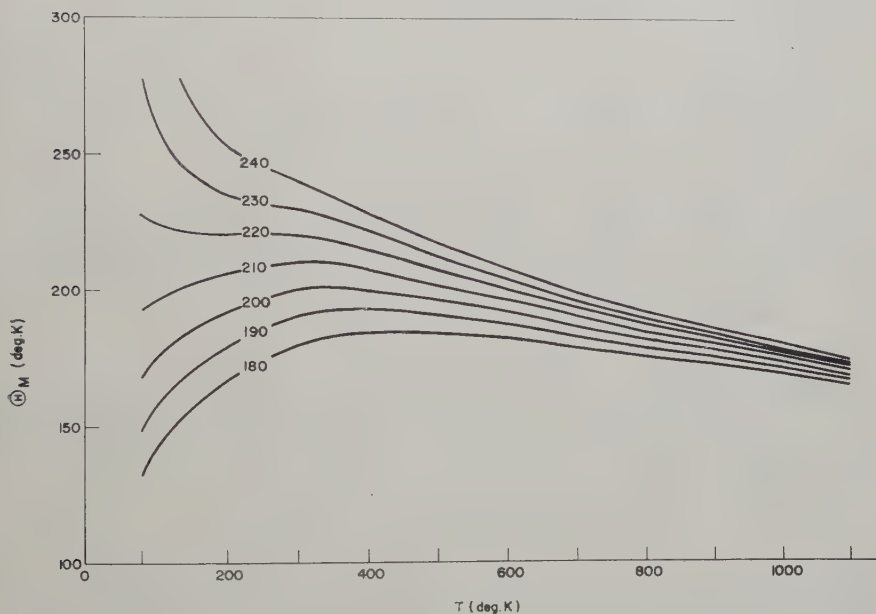
Variation of Θ_M with T calculated from smoothed curve of fig. 2. This shows how the curves of Θ_M against T depend on the values assumed for Θ_M (300) (attached to the relevant curves).

The Θ_D values from single-crystal elastic constants (fig. 1) were calculated by programming the method of Quimby and Sutton (1953) (see also Sutton 1955) for the Stantec Zebra electronic computer in our laboratory. The calculations of Debye temperatures summarized in fig. 3 were done by an iterative procedure on the computer using the rational approximation to the Debye integral given by Thacher (1960).

Fig. 4
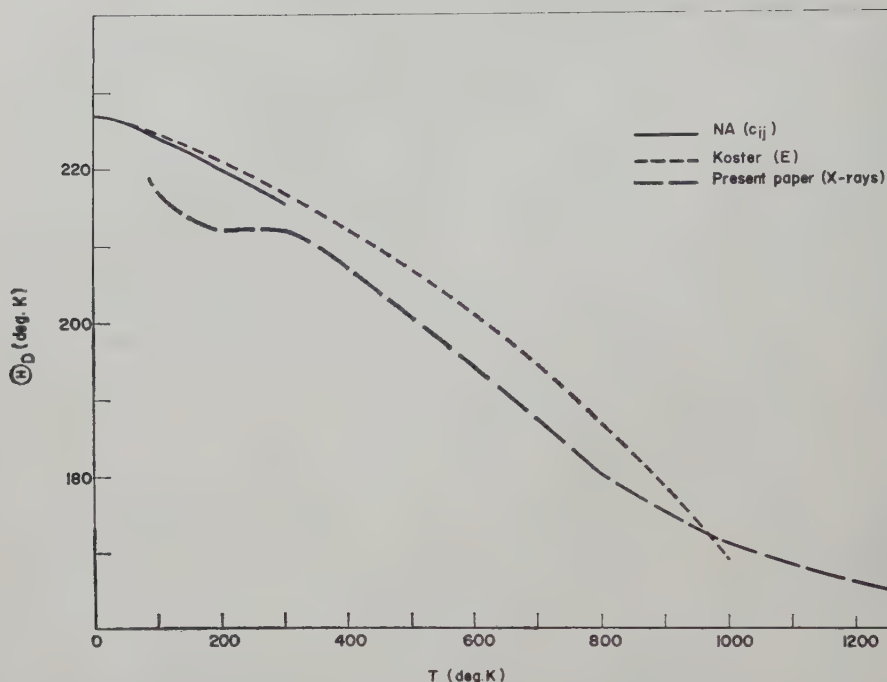
Comparison of x-ray values of Debye temperature (converted to Θ_D) derived in this paper with values reported previously from measurements of elastic constants.

Acknowledgments

References

ALERS, G. A., and NEIGHBOURS, J. R., 1959, *Rev. mod. Phys.*, **31**, 675.
ANDRIESSEN, R., 1935, *Physica*, **2**, 417.
BOSKOVITS, J., ROILOS, M., THEODOSSIOU, A., and ALEXOPOULOS, K., 1958, *Acta cryst., Camb.*, **11**, 845.
CHIPMAN, D. R., 1960, *J. appl. Phys.*, **31**, 2012.
CHIPMAN, D. R., and PASKIN, A., 1959, *J. appl. Phys.*, **30**, 1998.
HAWORTH, C. W., 1960, *Phil. Mag.*, **5**, 1229.
JAMES, R. W., 1950, *The Optical Principles of the Diffraction of X-rays* (London: G. Bell and Sons).
KOSTER, W., 1948, *Z. Metallk.*, **39**, 1.
NEIGHBOURS, J. R., and ALERS, G. A., 1958, *Phys. Rev.*, **111**, 707.
PASKIN, A., 1957, *Acta cryst., Camb.*, **10**, 667.
QUIMBY, S. L., and SUTTON, P. M., 1953, *Phys. Rev.*, **91**, 1122.

Spreadborough, J., and Christian, J. W., 1959, *Proc. phys. Soc. Lond.*, **74,** 609.

Sutton, P. M., 1955, *Phys. Rev.*, **99,** 1826.

Thacher, H. C., 1960, *J. chem. Phys.*, **32,** 638.

Zener, C., and Bilinsky, S., 1936, *Phys. Rev.*, **50,** 101.

The Effect of Ordering on the Strength and Dislocation Arrangements in the Ni₃Mn Superlattice

By M. J. Marcinkowski and D. S. Miller

Edgar C. Bain Laboratory for Fundamental Research,
United States Steel Corporation Research Centre,
Monroeville, Pennsylvania

Abstract

The dislocation configurations in thin foils of Ni₃Mn have been examined by transmission electron microscopy for various intermediate states of long-range order as well as for complete long-range disorder. It has been found that, as long-range order commences, pairs of ordinary dislocations, i.e. superlattice dislocations, are formed. The spacing between these pairs decreases as the order becomes more perfect.

Due to its relatively low stacking-fault energy, a high density of stacking-fault ribbons has been found to be present in the disordered alloy. Upon ordering, however, these faults are completely eliminated. This behaviour has been associated with an effective increase in the stacking-fault energy due to long-range order.

In addition, measurements of the flow stress show a pronounced increase in strengthening for the intermediate states of order. This behaviour has been discussed in conjunction with the present theories of order strengthening, all of which fail in one way or another to account suitably for the observed results. Another mechanism has been proposed which is associated with the destruction of the component of short-range order co-existing with long-range order, and is found to account qualitatively for the present results.

§ 1. Introduction

THE purpose of the present investigation is to analyse in detail the manner in which the transformation from disorder to order affects the yield and flow stress of a crystal lattice of the type A₃B (Cu₃Au). The particular alloy chosen was Ni₃Mn. This choice was made because of previous knowledge obtained by Marcinkowski and Brown (1961) for this system using both neutron diffraction and magnetic measurements. Their findings indicate that the ordering transformation in Ni₃Mn is somewhat more complicated than that of the classical Cu₃Au alloy; nevertheless there are many features of ordering common to both systems. We therefore expect that many of the results obtained for the alloy Ni₃Mn will also apply to other Cu₃Au type alloys and to a lesser extent, to other ordering systems in general.

A number of investigators have shown that ordering can lead to appreciable increases in strengthening, and they have proposed various theories to account for these changes (Ardley 1955, Brown 1959, Cottrell 1954,

Fisher 1954, Flinn 1960, Sumino 1958). All of these theories depend, in rather diverse ways, on the possible modes of behaviour of dislocations in an ordered lattice, and account satisfactorily for several important aspects of order strengthening. On the other hand, many of these theories fail to account for a number of important features of order strengthening, particularly at large plastic strains.

The method of approach used in this investigation has been first to measure the actual yield and flow stresses of polycrystalline wire specimens in the disordered state and in various configurations of order. The nature of the dislocations in these various states of order was then studied by examining thin foils of the alloy, corresponding to the ordered configurations in the wires, by employing the powerful techniques of transmission electron microscopy (Hirsch 1959). Marcinkowski *et al.* (1960, 1961) were the first to show directly that the dislocations in the ordered Cu$_3$Au alloy consisted of coupled pairs of ordinary dislocations or superlattice dislocations. Preliminary experiments by Marcinkowski and Fisher (1960) have also revealed their presence in ordered Ni$_3$Mn alloys. From the arrangements of these superlattice dislocations in the alloy after various states of order and strain, it should be possible to deduce the manner in which these arrangements may have given rise to changes in the yield and flow stresses of the wire samples as a function of the degree of order.

§ 2. Experimental Procedure

A vacuum-melted ingot containing 22·7 atomic % manganese was prepared as described in a previous paper (Marcinkowski and Brown 1961). Foils approximately 0·003 in. thick were then obtained by cold rolling a portion of the ingot. Tensile specimens with a gauge length of 0·303 in. and 0·240 in. wide were subsequently cut from these foils with the aid of a form shaped to the size of the specimen. In order to obtain large enough grains suitable for transmission electron microscopy, the foils were then annealed in evacuated vycor capsules for about two hours at 1000°c. The specimens were in turn disordered by quenching from 600°c and then given various ordering anneals in a low-temperature salt bath in a manner to be described more fully in the following sections. The specimens were subsequently strained plastically by various amounts in an Instron tensile testing machine. The gauge sections were cut from the specimens and then electropolished into thin foils suitable for electron transmission microscopy. The techniques for electropolishing the specimens and the elesctropolishing solution used are the same as those for Cu$_3$Au and have been described previously (Fisher and Marcinkowski 1961, Fisher and Szirmae 1959). All of the electron microscopy was carried out with a Siemens Elmiskop I operating at 100 kv.

A second portion of the ingot was swaged and drawn into wires 0·040 in. in diameter. These wires were then annealed for two hours at 900°c

to produce a mean grain diameter of 0·10 mm. This figure is based only on the large angle boundaries and does not take into account the large number of annealing twins which were present in the specimen. If the twin boundaries are considered along with the large angle boundaries, then the mean grain diameter is reduced to 0·06 mm.

The threaded portion of small brass bolts, with holes drilled through their centres, were then silver soldered onto each end of the wire specimens in such a manner that the gauge length of the specimens was 0·250 in. The wires were given various ordering anneals similar to those of the foils, and in all cases the strain rate used was 0·08 in./in.-min. In addition all of the plastic deformation was carried out at room temperature. Upon reaching stresses of about 100 000 lb/in.², the silver soldered joint holding the threaded grips to the wire specimen broke, nevertheless the joint was sufficiently strong to allow plastic strains of up to 14%.

§ 3. RESULTS AND DISCUSSION

3.1. *Variation of the Superlattice Dislocation Extension with Changes in the Degree of Long-range Order*

Marcinkowski *et al.* (1960, 1961) have considered in detail the equilibrium configuration of superlattice dislocations in the Cu_3Au type superlattices. The detailed arrangement is shown schematically in fig. 1 (*b*) as compared to the ordinary dislocations shown in fig. 1 (*a*)†, and is seen to consist of four bound partials of the type $\frac{1}{6}a\langle112\rangle$. Partials 1–2 and 3–4 are each separated from one another by the distance r_1, and enclose a stacking fault (S.F.) whereas the area enclosed by partials 1 and 4 consists of a slip-produced antiphase boundary (A.P.B.). Marcinkowski *et al.* (1960, 1961) have found that in most cases, r_1 and r can be expressed analytically, for a dislocation whose Burgers vector makes an arbitrary angle to the dislocation line, as follows

$$r_1 = \frac{G|\mathbf{b}|^2}{2\pi\left(E_F + \frac{E_{OR}}{2}\right)}\left[\left\{\cos\theta\cos\left(\theta+\frac{\pi}{3}\right)\right\}\frac{1}{1-\nu} + \sin\theta\sin\left(\theta+\frac{\pi}{3}\right)\right],$$

$$\cdots \quad (1)$$

$$(r - r_1) = \frac{G|\mathbf{b}|^2}{2\pi E_{OR}}\left[\left\{\cos\theta + \cos\left(\theta+\frac{\pi}{3}\right)\right\}^2\frac{1}{1-\nu} + \left\{\sin\theta + \sin\left(\theta+\frac{\pi}{3}\right)\right\}^2\right]$$

$$\cdots \quad (2)$$

where E_F is the stacking-fault energy, E_{OR} the energy of the A.P.B., G is the shear modulus, $\mathbf{b}$ the Burgers vector of the partial dislocation, ν is Poisson's ratio, and θ is the angle between $\mathbf{b}$ and the x-axis as shown in fig. 1. In general, the spacing r_1 will be much too small to be resolved by transmission electron microscopy, and one therefore sees only a single

---

† Figures 2–7, 9, 10 and 13 are shown as plates.

Fig. 1
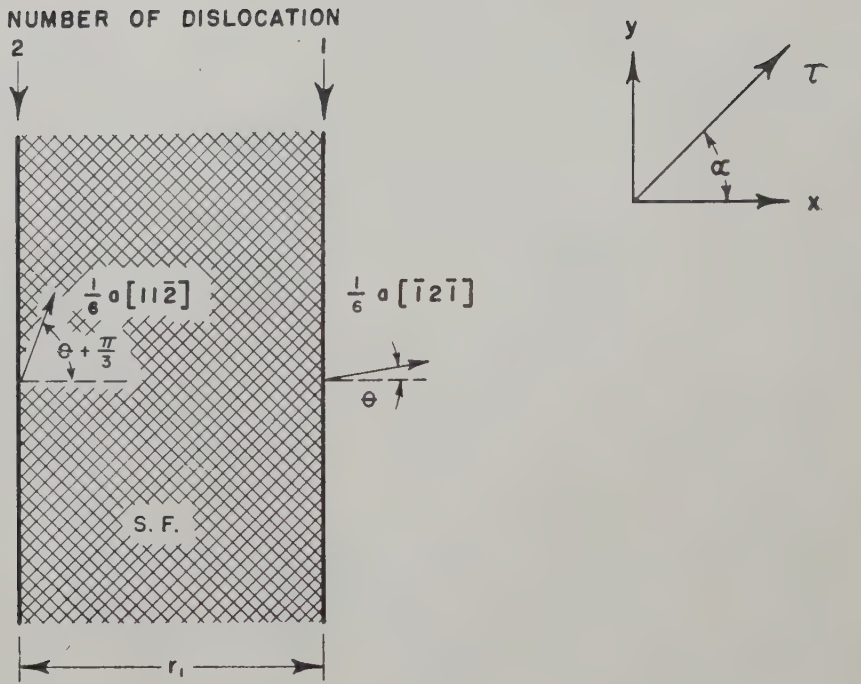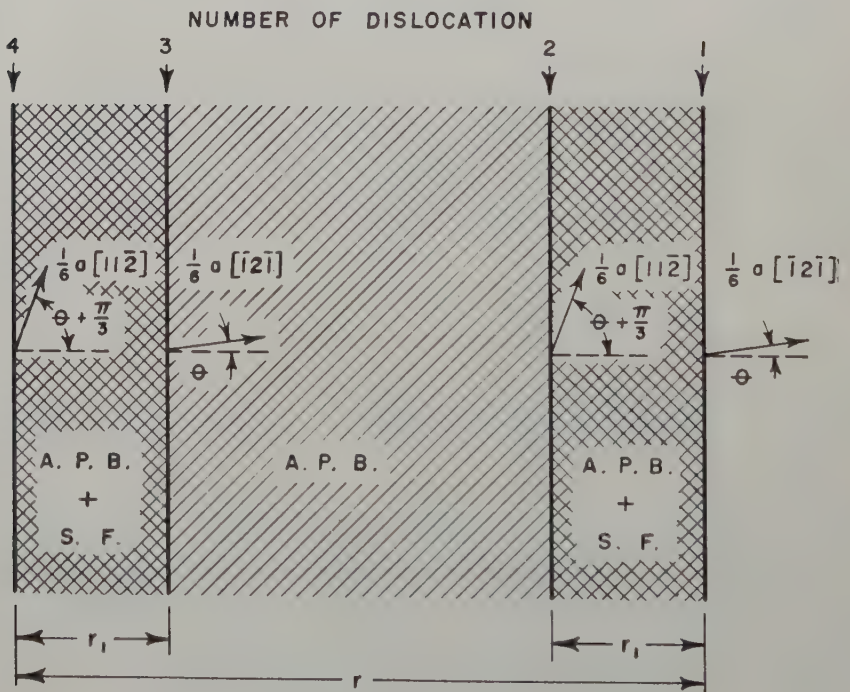
(a) Ordinary dislocation in the disordered Ni₃Mn alloy. (b) Superlattice dislocation in the ordered Ni₃Mn alloy.

dislocation pair consisting of 1–2 and 3–4. The spacing between these pairs is therefore essentially a measure of r.

These predictions have been confirmed for the particular case of the Cu_3Au superlattice (Marcinkowski *et al.* 1960, 1961). The transmission electron micrograph of fig. 2 obtained from a Ni_3Mn alloy possessing nearly perfect order and strained 5% shows that these predictions also hold in the present case. The nearly constant spacing r between the dislocations was found to be about 179 Å. In order to compare these results with the theoretical predictions of eqns. (1) and (2), the values of G and ν were obtained from the data of Köster and Rauscher (1948) and found to be 7×10^{11} dynes/cm² and 0·31, respectively. $|b|^2$ was obtained from the lattice constants determined by x-rays as $2·18 \times 10^{-16}$ Å². The value of E_F is assumed to be about 20 ergs/cm² and will be considered in greater

Table 1. Equilibrium separation of partial dislocations in Ni_3Mn for various degrees of long-range order

r_1^e†	r^e†	r_1^s†	r^s†	r‡
		$S=1$		
35 Å	176 Å	17 Å	114 Å	179 Å
		$S=0·68$		
55 Å	359 Å	25 Å	234 Å	286 Å
		$S=0·45$		
74 Å	771 Å	34 Å	513 Å	714 Å
		$S=0$		
102 Å	∞	48 Å	∞	—

† Theoretical.
‡ Experimental.

detail in a following section. E_{OR}, on the other hand, can be obtained using either the Peierls (1936) approximation for the ordering energy or that of Yang (1945). Both approximations give nearly the same value for E_{OR} or about 95 ergs/cm². However, if these values are used in eqns. (1) and (2), r is found to be about 25% smaller than the observed value. This may be due partly to the approximate nature of the ordering theories and partly to the fact that the alloy used in the present investigation was not at the exact stoichiometric composition Ni_3Mn. If however we assume a value of $E_{OR} = 75$ ergs/cm², the results shown in table 1 are

obtained. The superscripts e and s above r_1 and r refer to pure edge and screw dislocations, respectively; i.e. $\theta = 60°$ and $-30°$, respectively, and were chosen since they give rise to maximum and minimum values of r, respectively. The agreement between theory and experiment is good if pure edge dislocations are assumed to be present in fig. 2; however, this can only be assumed with the techniques now available. Because of the smaller repulsive forces between screws as compared to edges, r^s is found to be smaller than r^e.

As the long-range order S decreases, the energy of the A.P.B. holding the superlattice dislocations together will decrease rapidly, since E_{OR} for any S is given by $S^2 E_{OR}^{(S=1)}$. The separation between the dislocation pairs due to their mutual repulsive forces will then increase. Figure 3 shows a micrograph of a partially ordered Ni_3Mn alloy after attaining equilibrium at 465°C, where S as determined by neutron diffraction (Marcinkowski and Brown 1961) is 0·68, so that E_{OR} in this case is 34·8 ergs/cm². The increase in spacing r is apparent in fig. 3 and is found to be about 286 Å as compared to the value of 355 Å calculated from eqns. (1) and (2) and shown in table 1. The value of r measured from fig. 3 is an average value, since as can be seen from this figure, the dislocation pairs exhibit an undulated appearance. According to Marcinkowski and Brown (1961), the state of partial long-range order in Ni_3Mn is probably not homogeneous, but consists of regions of long-range order in a matrix of short-range order. The pair of bound ordinary dislocations constituting the superlattice dislocation will then be held together tightly when it lies within a region of long-range order while being strongly repelled in the matrix of short-range order.

The long-range order was then decreased to 0·45 by allowing equilibrium to be reached at 475°C, just 5°C below the critical ordering temperature and therefore corresponds to an A.P.B. energy of 15 ergs/cm². The very large increase in r can be seen in fig. 4 and is about 714 Å compared to the calculated value of 771 Å for a pure edge dislocation shown in table 1. The A.P.B. energy in fig. 4 is now sufficiently low so that in some cases the two ordinary dislocations constituting the superlattice dislocation encounter difficulty in moving as a unit. This can be noted in fig. 4 where a large portion of the leading ordinary dislocation of the super-lattice dislocation at A has been separated far beyond its equilibrium distance from the trailing dislocation at B. This is thought to arise in part from the pinning of the trailing dislocation B by the stress field of the superlattice dislocation in the vicinity of B.

Figure 5 shows another region of the same grain from which fig. 4 was obtained. Here it will be noted that the stress concentrations set up by the inclusion labelled A are sufficient to generate dislocations at the interface between the matrix and the inclusion. This can be seen by the distinct loops emanating from both the right and left sides of this inclusion. Another interesting feature of this figure is that the dislocations are nucleated as superlattice dislocations. If the extension of the superlattice

dislocation is not too large, then the applied stress τ necessary to maintain them at a given radius of curvature R is the same as for ordinary disloca- tions or

$$\tau = \frac{G|\mathbf{b}|}{2R}. \qquad \cdot \quad \cdot \quad \cdot \quad \cdot \quad \cdot \quad \cdot \quad \cdot \quad \cdot \quad (3)$$

The value of R obtained from fig. 5 is 857 Å, which when used in eqn. (3) gives $\tau = 10 \cdot 5 \times 10^8$ dynes/cm² or about 15 100 p.s.i. The stress concentra- tion actually needed to nucleate the superlattice dislocation however is expected to be appreciably larger than this value because of the relatively small initial value of R.

A second interesting feature of fig. 5 is that a large number of the dislocations are strung out in the direction of the slip plane trace. Part of this behaviour may be accounted for by the pinning of portions of the dislocation line by inclusions such as those at A and also by other dis- locations on other slip systems. This pinning may be sufficiently strong so that the applied stress is sufficient to overcome the line tension of the dislocation $G\mathbf{b}^2/2$ and thus elongate the dislocation in a direction almost parallel to the slip trace. Above 480°c, the long-range order disappears, (Marcinkowski and Brown 1961), with the result that r increases to infinity, while r_1 increases to its equilibrium value in the disordered alloy as shown in table 1.
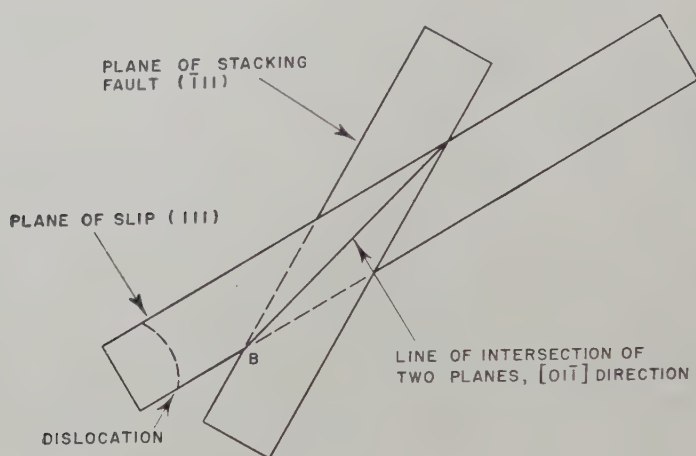
3.2. *Stacking Faults in the Disordered Alloy*

The frequency with which stacking faults were observed in the dis- ordered alloy was relatively high indicating that their energy is relatively low. This can be seen by referring to fig. 6 which shows a region near the edge of the foil containing a high density of faults. An interesting feature of this micrograph is that the stacking faults, particularly those near A, appear to be more resistant to electrochemical attack than the matrix similar to what Swann and Nutting (1959–60) have found in other alloys. In order to obtain an estimate of this energy, the radius of curvature of the partial dislocations at extended nodes in several hexagonal networks was measured using a procedure previously described in detail by Whelan (1958). A stacking-fault energy $E_F \simeq 20$ ergs/cm² was determined by this method, but because of the small extension at the nodes, E_F should be considered only as an estimate.

It is of interest next to consider to what extent the numerous faults may interfere with the motion of dislocations and thus contribute to work hardening. Figure 7 clearly shows that dislocations are able to cut through stacking faults, with the result that the stacking fault has become segmented in a large number of places. Consider first the slip plane outlined by the dotted lines in fig. 7 on which dislocations give rise to the displacement of the stacking fault shown at A. The details of the

process taking place on this slip plane are shown schematically in fig. 8 (*a*), (*b*). Dislocations travelling on the plane (111) intersect a stacking fault lying on the plane ($\bar{1}$11) and cut through it along the direction [011]. The Burgers vectors of the cutting dislocations are such that they displace the lower portion of the stacking fault downward and toward the right

Fig. 8

PLANE OF STACKING
FAULT ($\bar{1}$11)

PLANE OF SLIP (111)

B

LINE OF INTERSECTION OF
TWO PLANES, [01$\bar{1}$] DIRECTION

DISLOCATION

(*a*)

n b C

D
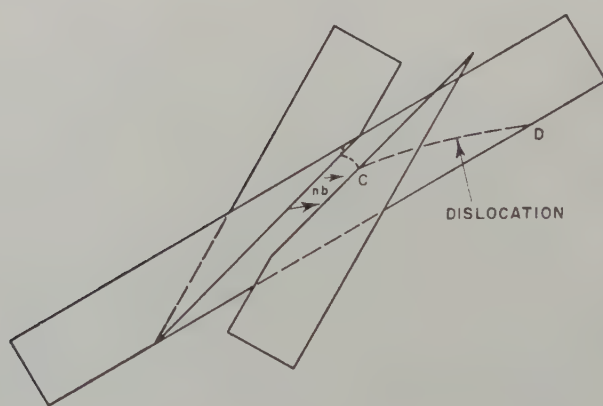
DISLOCATION

(*b*)

(*a*) Before intersection of dislocations with stacking fault. (*b*) After intersection of dislocations with stacking fault.

with respect to the upper portion of the stacking fault. The obvious choice of the Burgers vector to accomplish this displacement is $\frac{1}{2}$[10$\bar{1}$]. Thus, when *n* dislocations cut through the fault, the total displacement of the bottom part with respect to the top will be *n***b** as shown in fig. 8 (*b*).

It is apparent from fig. 7 that the dislocations cut through the stacking fault only with considerable difficulty. Referring to fig. 8 (*a*), (*b*), before the dislocations have cut through the fault, they are essentially perpendicular to the line of intersection of the slip plane and the surface in order to minimize their line energy. Under a suitable pile-up of dislocations at the fault, the leading dislocation is driven through a portion of the fault. For convenience, fig. 8 (*a*) shows that the dislocation first breaks through the stacking fault at B, similar to those in the slip plane A, in fig. 7. Figure 8 (*b*) shows a later stage of the cutting process. The segment of the dislocation line C–D that has already passed through the fault is elongated in a direction nearly parallel to the trace of the slip plane. This occurs because that portion of the dislocation C–D that has already cut through the fault is relatively mobile, but is held back to a certain extent by that portion of the dislocation line that has not yet passed through the fault, and therefore it rotates about C. Figure 7 also shows in detail three dislocation lines which are in the process of passing through the fault.

In order to account for the difficulty in passing a dislocation through a stacking fault, it is necessary to consider in detail the change in configuration of the atoms before and after the passage of the dislocation. Heidenreich and Shockley (1947) were the first to carry out this analysis and concluded therefrom that it should be a difficult process. They show that after the dislocation has passed through the fault, a number of the atoms in the fault are brought very close to one another. It is therefore expected that the stress to drive a dislocation through the fault would be on the order of the theoretical shear stress given by

$$\tau = \frac{|\mathbf{b}|}{a} \frac{G}{2\pi}, \qquad \cdots \cdots \quad (4)$$

and upon substituting the values of the constants gives $\tau = 4 \cdot 6 \times 10^{10}$ dynes/cm² or 660 000 lb/in.². Since this stress is very much higher than the applied stress, it is obvious that some suitable stress concentration, such as that arising from a pile-up of dislocations, must be present. We therefore expect that stacking faults will contribute significantly to a high rate of work hardening in the crystal. As a consequence of this cutting process the stacking-fault separations created by the intersecting dislocations in fig. 7 are each bounded by partial dislocations of equal and opposite sign (Heidenreich and Shockley 1947).

Figure 9 shows some other interesting features of stacking faults in the disordered alloy. These faults are seen to lie on intersecting (111) and (Ī11) planes, and in all cases, are not simple, but consist of a number of faults on overlapping parallel planes. This is obvious from the change in contrast over various portions of their length. According to Whelan and Hirsch (1957), depending on whether two or three faults, or multiples thereof, overlap on closely spaced slip planes, the contrast may either reverse sign as at A in fig. 9 or else vanish as at B in this same figure.

A second interesting feature of fig. 9 are those portions of the stacking fault above and below c which appear very dark. Close examination shows that these faults have associated with them, Moirè patterns. Similar observations have been made by Swann (private communication) with copper alloys, who ascribes this behaviour to the segregation of solute atoms to the faults. This segregation in turn alters the lattice constant of the crystal in the vicinity of the fault with respect to the matrix, and thus gives rise to a Moirè pattern similar to that obtained from overlapping crystals of slightly varying d spacing (Menter 1958).

It will also be noted in fig. 9 that the stacking faults do not intersect one another. At D for example, the faults on the (111) plane go completely around the one lying on $(\bar{1}11)$. Also at E, the faults on the (111) plane terminate upon meeting those on the $(\bar{1}11)$ plane. This difficulty in intersection arises for two reasons. In the first place, the stress required to pass one fault through the other will require a stress on the order of magnitude of that calculated from eqn. (4). Secondly, the dislocations in fig. 9 have probably been split by the stress concentrations within the foil, which are much smaller than those necessary to give rise to stresses of the magnitude given by eqn. (4).

Figure 10 shows that in the disordered alloy, ordinary dislocations can also be generated at stacking-fault interfaces. This is vividly illustrated in the region A of fig. 10 where a large number of dislocation loops are seen to originate at the interface of the stacking fault or faults lying on the $(\bar{1}1\bar{1})$ plane. Furthermore, these loops are seen to result in the formation of a slip band at B containing a number of dislocations. The smallest loop that can be detected at A has a radius of curvature of about 400 Å which from eqn. (3) implies a stress concentratoin on the order of $22 \cdot 2 \times 10^8$ dynes/cm² or 32 300 lb/in.². Thus, we have the interesting result that stacking faults not only contribute to increased work hardening but also provide numerous sources for dislocations.

3.3. *The Effect of Order on the Splitting of Partial Dislocations in an Externally Applied Stress Field*

The splitting of the ordinary dislocations beyond their equilibrium values given in table 1 is thought to arise from stress concentrations set up within the foils from carbon contamination or reaction with the surface of the foil. Upon ordering, this splitting is eliminated, and the following sections will attempt to explain how this comes about. In the disordered state it is only necessary to consider a single pair of partial dislocations such as 1 and 2 in fig. 1 (a) which are held together by a stacking fault and which lie in the x–y plane. Upon application of an externally applied stress, the force on dislocation 1 will be given by

$$F_1 = \tau |\mathbf{b}| \cos (\alpha - \theta) \qquad \cdots \cdots (5\,a)$$

where τ is the externally applied shear stress on the z plane acting in a direction α degrees to the x axis, while $\mathbf{b}$ is the Burgers vector of the

partial dislocation which makes an angle of θ with the x axis. This force acts at right angles to the dislocation line and may be either positive or negative, driving the dislocation to the right or to the left respectively. In a similar manner the force on dislocation 2 is found to be

$$F_2 = \tau |\mathbf{b}| \cos \left(\alpha - \theta - \frac{\pi}{3} \right). \qquad \qquad (5\ b)$$

It is obvious from eqns. (5 a) and (5 b) that in the disordered alloy, dislocations 1 and 2 have unbalanced forces exerted upon them due to τ. In addition, there is a mutual elastic repulsive force F_R that contributes to the separation. Thus, the total force tending to split the dislocations from one another must overcome the attractive force due to the stacking fault E_F, so that

$$(F_1 - F_2) + F_R = E_F. \qquad \qquad (6)$$

For convenience, the dislocation line is considered to lie along the y axis in fig. 1 (a), and F_R for arbitrary θ is given by

$$F_R = \left(\frac{1}{r_1} \right) \left(\frac{G|\mathbf{b}|^2}{2\pi} \right) \left[\frac{\cos (\theta + \pi/3) \cos \theta}{1 - \nu} + \sin (\theta + \pi/3) \sin \theta \right]. \qquad (7)$$

Combining eqns. (5 a), (5 b), (6) and (7), we obtain for τ

$$\tau = \frac{E_F - \left(\dfrac{1}{r_1} \right) \left(\dfrac{G|\mathbf{b}|^2}{2\pi} \right) \left[\dfrac{\cos (\theta + \pi/3) \cos \theta}{1 - \nu} + \sin (\theta + \pi/3) \sin \theta \right]}{|\mathbf{b}|[\cos (\alpha - \theta) - \cos (\alpha - \theta - \pi/3)]}. \qquad (8)$$

Now it is of interest to determine the most favourable conditions under which splitting will occur, i.e. smallest applied τ, since this turns out to be an interesting configuration geometrically; and furthermore, it is expected that this arrangement will be encountered in a few cases experimentally. This can be done by maximizing eqn. (7) along with the term $(F_1 - F_2)$, and it turns out that such is the case when $\theta = 150°$, i.e. when the full dislocation is pure edge, and when $\alpha = 90°$. The detailed plot of τ versus r_1 is shown in fig. 11. As the separation increases, the repulsive forces F_R contributing to the splitting fall off as $1/r_1$ so that at a distance $r_1 \simeq 1000$ Å, the second term in eqn. (8) becomes negligible so that τ need be sufficient to overcome only E_F. It is also of interest to note that in the specific case considered, the forces on dislocations 1 and 2 of fig. 1 (a) will be equal and opposite so that dislocation 1 will move to the right while dislocation 2 will move to the left.

Consider now the changes brought about when the alloy becomes perfectly ordered, i.e. $S = 1$, while still keeping $\theta = 150°$ and $\alpha = 90°$, for comparison with the previous result. Referring to fig. 1 (b), it will be noted that the force on partial No. 2 due to τ will drive it to the left, while that on partial No. 3 will drive it to the right with an equal force. This pair of dislocations can thus be thought of as essentially being bound together, while partial No. 1 will be driven to the right and partial No. 4 will be driven to the left. The applied stress necessary to drive partials Nos. 1 and 4 away from the centre two must obviously now overcome

both the stacking fault energy E_F and the A.P.B. energy E_{OR}. This stress will be aided by the repulsive forces between the dislocations. In the disordered alloy, this stress was simply given by eqn. (10); however, in the case of the ordered alloy, there are now the mutual repulsive forces between four dislocations to contend with. A reasonable approximation to F_R can be obtained for large values of r_1 (≥ 100 Å) by assuming dislocations 2 and 3 are pushed sufficiently close together so that they act as a single dislocation on either 1 or 4. This contribution for F_R thus obtained is

$$F_R{}^1 = \frac{1}{r_1}\left(\frac{G|\mathbf{b}|b_1}{2\pi}\right)\left(\frac{\cos 150°}{1-\nu}\right) \quad \cdot \quad \cdot \quad \cdot \quad \cdot \quad \cdot \quad (9)$$

where b_1 is the sum of the Burgers vectors of partial dislocations number

Fig. 11
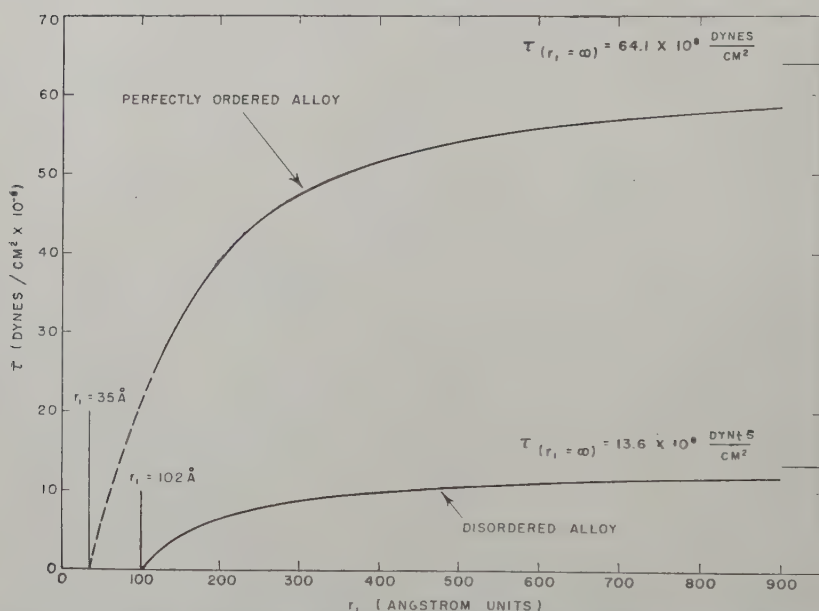
Stresses required to separate partial dislocations by various amounts in both the ordered and disordered Ni$_3$Mn alloy obtained from eqn. (11) and (8) respectively for $\theta = 150°$ and $\alpha = 90°$.

2 and 3 and is therefore of the type $\frac{1}{2}a_0 \langle 110 \rangle$. Also, dislocation 1 or 4 sees the repusive stress field from the other given by:

$$F_R{}^2 = \left(\frac{1}{2r_1}\right)\left(\frac{G|\mathbf{b}|^2}{2\pi}\right)\left[\frac{\cos(210°)\cos(150°)}{1-\nu} + \sin(210°)\sin(150°)\right]$$
$$\cdot \quad \cdot \quad \cdot \quad (10)$$

By replacing E_F by $E_{OR} + E_F$ in eqn. (6) and substituting eqns. (5 *a*), (5 *b*), (9) and (10) in this same equation, we obtain the following stress

to split the superlattice dislocation between partials Nos. 1 and 2, and 3 and 4:

$$\tau = \frac{(E_{OR} + E_F) - (F_R{}^1 + F_R{}^2)}{|\mathbf{b}|[\cos(90° - 150°) - \cos(90° - 150° - 60°)]} \cdot \quad \cdot \cdot \quad (11)$$

This stress is plotted in fig. 11 where again it is noted that at the equilibrium value of $r_1 = 35$ Å, a vanishingly small stress is needed to cause a small splitting. At about $r_1 = 1000$ Å on the other hand, the applied stress reaches its limit-value of 64.5×10^8 dynes/cm^2, which is the stress necessary to move both end partials in fig. 1 (b) to infinity.

Thus, we see that even in the most favourable case, the stress to split a superlattice dislocation is about five times that for an ordinary dislocation. From the curvature of the dislocation lines in thin metal foils, Hirsch (1959), using eqn. (3), has found the local stresses within most foils to be on the order of $G/1000$. For the Ni$_3$Mn alloy, this amounts to 7×10^8 dynes/cm^2, which is close to that value necessary to cause splitting of ordinary dislocations; however, this stress is only 1/9 that required to separate the partials of a superlattice dislocation by an infinite amount. We expect therefore that even in those cases where the Burgers vector of the dislocation is located in the most favourable position with respect to the stress field, τ, that the splitting of a superlattice dislocation into widely separated partials should not in general be observed, in agreement with the present observations.

Thus far, detailed consideration has been given only to the case where $\theta = 150°$, since this was an interesting arrangement geometrically. Curves similar to those in fig. 11 can be calculated for various other values of θ, however in the case of the ordered alloy, somewhat more involved expressions are necessary for the total elastic repulsive forces between the four partial dislocations, and will not be considered in detail here. On the other hand, most of the important features associated with a variation in θ can be observed by considering only that stress necessary to separate the partial dislocations by an infinite amount, so that the second term in eqn. (8) vanishes. The results obtained for the disordered alloy using eqn. (8), and for the ordered alloy obtained by replacing E_F by $E_F + E_{OR}$ in this same equation, are shown in fig. (12), where here again α, for convenience, is kept constant at 90°†. This figure shows that even with an infinite applied stress, it is only for values of θ lying between 60 and 240° that it is possible to separate the partial dislocations of either ordinary or superlattice dislocations by an infinite amount. This phenomenon arises because outside of this range of θ, the forces on the dislocations are such as to contract the individual partial dislocations below their equilibrium spacing instead of separating them.

---

† Since τ, as can be seen from the denominator in eqn. (8), depends only on the relative orientation of $\mathbf{b}$ with respect to τ, there is no loss of generality by keeping α constant and varying θ; i.e. all of the possible values of τ with respect to its orientation to $\mathbf{b}$ are accounted for.

The relative motions of the partials with respect to one another under a sufficiently high externally applied stress vary widely with θ, and are shown in table 2 for the case of the superlattice dislocation. This table can also be readily used for the ordinary dislocations in the disordered alloy by merely deleting all those quantities associated with the numbers 3 and 4. Finally, as fig. 12 shows, departures from $\theta = 150°$ make the splitting of superlattice dislocations even more difficult with respect to ordinary dislocations.

Fig. 12
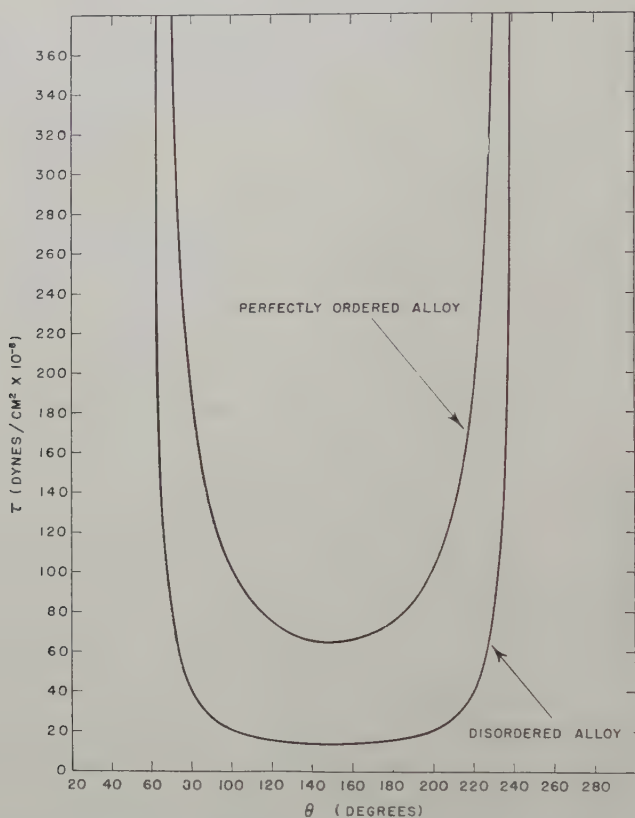
Stresses required to separate partial dislocations by an infinite amount in both the ordered and disordered Ni_3Mn alloy obtained from eqn. (8) for $\alpha = 90°$.

3.4. *Variation of the Yield and Flow Stress with Order*

Before considering in detail the manner in which order affects the flow stress of the Ni_3Mn alloy, it is of interest to examine further the nature of the dislocation arrangements in both the ordered and disordered alloys. Figure 13 shows the arrangement of ordinary dislocations in the disordered alloy after a strain of 5%. As will be noted, many dislocations are

concentrated on a relatively small number of slip planes.   From measurements made on several different areas similar to that shown in fig. 13, the average spacing between the slip planes containing dislocations is found to be about 3000 Å.   On the other hand, referring again to the micrograph of the fully ordered alloy shown in fig. 2, which was also deformed 5%, it will be noted that the dislocations are no longer concentrated into widely spaced slip bands; instead, a relatively small number of dislocations lie on many closely spaced planes.   It is estimated that their average distance is below 500 Å, and in many cases less than 200 Å. This decrease in spacing between slip planes upon ordering has also been observed using surface replica techniques for Cu_3Au, Ni_3Mn, and Pt_3Co

Table 2.   Detailed nature of the splitting of a superlattice dislocation under an applied stress.   (Table can also be used for ordinary dislocations by omitting those quantities associated with partial dislocations 3 and 4)

θ	Relative Magnitudes of forces on dislocations	Direction of forces on dislocation line	Nature of splitting of superlattice dislocation
0–60° 60–120°	$F_2 = F_4 > F_1 = F_3$ $F_1 = F_3 > F_2 = F_4$	All + All +	Contraction occurs Split occurs between 4 and 3. 3, 2 and 1 move in + direction w r t 4
120–150°	$F_1 = F_3 > |F_2| = |F_4|$	1 and 3 are + 2 and 4 are −	Split occurs between 4 and 3. 3, 2 and 1 move in + direction w r t 4
150–180°	$|F_2| = |F_4| > F_1 = F_3$	1 and 3 are + 2 and 4 are −	Split occurs between 4 and 3. 4 moves in − direction w r t 3, 2 and 1
180–240°	$|F_2| = |F_4| > |F_1| = |F_3|$	All −	Split occurs between 4 and 3. 4 moves in − direction w r t 3, 2 and 1
240–300° 300–330°	$|F_1| = |F_3| > |F_2| = |F_4|$ $|F_1| = |F_3| > F_2 = F_4$	All − 1 and 3 are − 2 and 4 are +	Contraction occurs Contraction occurs
330–360°	$F_2 = F_4 > |F_1| = |F_3|$	2 and 4 are + 1 and 3 are −	Contraction occurs

(Taoka and Honda 1957, Taoka and Sakata 1957, Taoka *et al.* 1959), and thus appears to be fundamental to at least the ordered structures based on the face-centered cubic lattice.   Flinn (1960) has accounted for this behaviour in terms of the interaction of dislocations with short-range order.   On the other hand, there is still another possible mechanism

that could account for this behaviour which makes use of an expected difference in the frequency of cross-slip between the ordered and disordered alloy. As explained in detail by Seeger (1957), for disordered alloys, the critical quantity determining the ease with which cross-slip will occur is the stacking-fault energy holding the pair of partial dislocations together. In the disordered Ni_3Mn alloy, the stacking-fault energy is relatively low, i.e. 20 ergs/cm²; and as can be seen from table 1, leads to a value for r_1 of 48 Å for the pure screw dislocation. Upon ordering, however, r_1 begins to decrease and finally reaches a value of 17 Å after nearly perfect long-range order is attained. In other words, ordering produces an apparent increase in the stacking-fault energy between the two pairs of partial dislocations of the superlattice dislocation in fig. 1 (b). The manner in which this comes about can be seen from eqn. (1). For the disordered alloy, the energy term in parentheses in the denominator of eqn. (1) is merely E_F, and the value of r_1 is simply that distance between the two partials of the ordinary dislocation in fig. 1 (a). Upon ordering however the additional surface tension due to the A.P.B. between partial dislocations Nos. 1 and 4 in fig. 1 (b) gives an apparent increase in the stacking-fault energy of $E_{OR}/2$. The effective stacking-fault energy between partials 1–2 and 3–4 for the superlattice dislocation now becomes for any S,

$$E_F{}^S = \left(E_F + S^2 \frac{E_{OR}}{2} \right). \qquad \cdots \cdots \quad (12)$$

For the Ni_3Mn alloy in the case where $S = 1$, this expression leads to a value of 58 ergs/cm² or about three times the value of 20 ergs/cm² obtained for the disordered alloy. This result has far-reaching consequences. In the first place it is expected that cross-slip and double cross-slip in the ordered alloy could be made relatively simple compared to that of the disordered alloy, resulting in the occupation of a large number of slip planes by a given number of dislocations as shown in fig. 2. On the other hand, the effective stacking-fault energy in the disordered alloy is low, making cross-slip much more difficult and thus leading to the occupancy of a small number of slip planes by a given number of dislocations as shown in fig. 14. The details of these processes will be considered in a future paper. Thus far, we have not yet made a sufficiently extensive investigation to substantiate these hypotheses by direct observation with thin foils; however, this work is continuing. It is of interest next to consider some general features of the stress–strain curves obtained for the ordered and disordered alloys. Two of these are shown in fig. 14 where it will be noted that both curves show rather sharp yield points. The yield point in the disordered alloys is thought to be due to the destruction of short-range order by the first few dislocations, while that in the ordered alloy can be explained by at least two theories based on the pinning of dislocations by order (Brown 1959, Sumino 1958). In addition, the yield strength of the fully ordered alloys is higher by about 6000 lb/in.² than

in the disordered alloy.   The most interesting feature of the curves shown
in fig. 14 is that the rate of work hardening in the ordered alloy is almost
twice as great as that for the disordered alloy.   Similar behaviour has
been found by Flinn (1960) for an alloy based on the Ni_3Al superlattice
and by Biggs and Broom (1954) for Cu_3Au.   Flinn has suggested that
the high rate of work hardening in the ordered alloys is due to the decrease
in size of the antiphase domains with increasing amounts of deformation.

Fig. 14
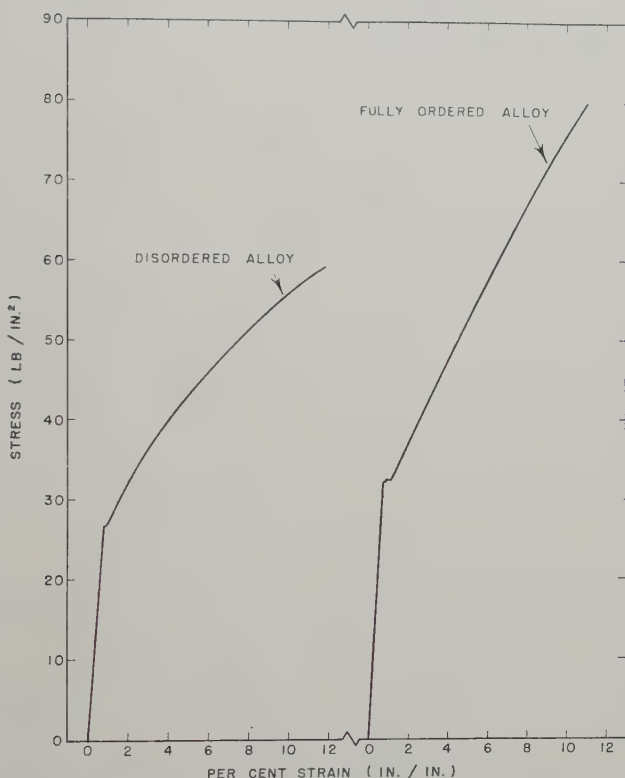
Stress–strain curves for disordered and fully ordered Ni₃Mn alloy.

Figure 15 shows in detail the manner in which the flow stress is altered
as the Ni_3Mn alloy is slowly cooled through the critical ordering tempera-
ture.   The specimens were in the form of wires described previously and
were cooled from 500°c at a rate of 2·78°c per day, quenched from the
temperatures indicated in fig. 15 and tested at room temperature
The four curves represent the flow stresses for the plastic strains
indicated at the right of the figure, while each data point represents the
average value of three measurements.   For convenience, the values of
the long-range order parameters as determined by neutron diffraction

measurements (Marcinkowski and Brown 1961) are shown at the bottom of the figure.

3.5. *Variation of the Yield and Flow Stress with Order*

An interesting feature of all the curves in fig. 15 is the increase in flow stress above that of either the disordered or fully ordered alloy between 480°c and 375°c, resulting in a maximum at 465°c. Maxima of a very similar nature have been previously observed in superlattices of CuZn (Brown 1959), Cu_3Au, CuAu, Cu_3Pd, Cu_3Pt (Köster 1940), Ni_3V, Pd_3V, Co_3V (Köster and Gmöhling 1960) and Fe_3Al (Lawley 1961). The position of these maxima varies from one alloy system to another and may lie at or below the critical ordering temperature. This

Fig. 15
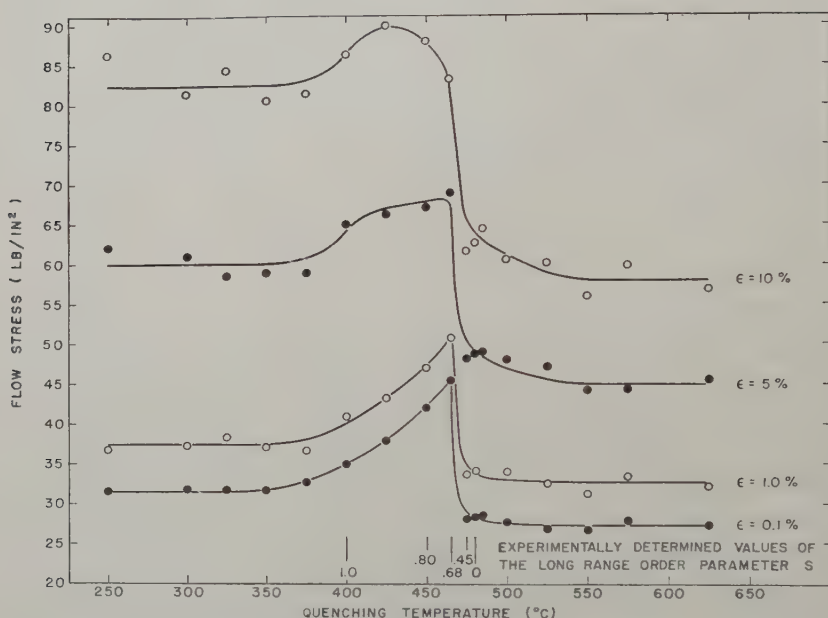
Flow stress as a function of quenching temperature for the plastic strains indicated. Measurements made at room temperature.

phenomenon is independent of the type of ordered lattice, and therefore appears to be a very general feature associated with ordering systems. Clearly then, any satisfactory theory of order strengthening should adequately account for this maximum in flow stress.

The earliest theory was that suggested by Cottrell (1954) in which the interaction of dislocations and antiphase boundaries may give rise to marked strengthening when the domains are about 50 Å in diameter. However, previous neutron diffraction results (Marcinkowski and Brown 1961) show that the domains in the alloys of fig. 15 are at least as great

as 500 Å. In addition, recent transmission electron microscopy with thin foils of $AuCu_3$ (Fisher and Marcinkowski 1961) and Fe_3Al (Marcinkowski and Brown 1961) show that the domains rapidly grow to sizes of several hundred angstroms at temperatures not too far below their critical ordering temperatures. Flinn (1960) has also proposed a theory to account for a similar maximum in yield strength observed in a Ni_3Al superlattice based on the climb of superlattice dislocations out of their slip planes. Because of the relatively low testing temperatures used in the present experiment, as well as the sluggishness of the transformation in Ni_3Mn, it is highly doubtful that this model would be valid in the present case. Another theory advanced by Brown (1959) makes use of the difference in energy between the equilibrium configuration of the antiphase boundary holding the pairs of ordinary dislocations of the superlattice dislocation together, and its higher energy state after it has been forced from this position by an applied stress. However, this theory encounters difficulty in attempting to account for the maximum that persists even up to strains as large as 10% since at these high strains we would expect most of the initially pinned dislocations to be freed from their equilibrium antiphase boundary configurations, with the result that the maximum should disappear. Sumino (1958), on the other hand, attributes this maximum to the interaction of the stress field of an edge dislocation with the lattice distortion due to ordering. However, no detectable change in lattice constants with ordering in Ni_3Mn has been observed (Hahn and Kneller 1958, Marcinkowski and Brown 1961), and if a difference is present, it is indeed very small, so that little or none of this type of interaction is to be expected.

In view of these difficulties, it is of interest to postulate another model which might account in part for the maximum in flow stress in fig. 15, based on Fisher's (1954) theory of short-range order hardening. As we have seen in figs. 4 and 5, superlattice dislocations are present up to at least 475°c. It would be expected therefore that these dislocations will move under little or no resistance from the long-range order since the antiphase domains are large. This is indeed the case when the degree of long-range order is high; however as Marcinkowski and Brown (1961) have shown, there is a considerable degree of short-range order co-existing with the long-range order for the partially ordered alloys in the region of 480°c to 400°c. Thus, the superlattice dislocations, even though they are unaffected by the long-range ordered component, must still overcome the resistance offered by the short-range order component. On the other hand, above the critical temperature, the degree of short-range order decreases. A maximum in strengthening is therefore to be expected in the vicinity of the critical temperature. Increasing ease of cross-slip may contribute to the strengthening by forcing a given number of dislocations to travel over a greater number of slip planes, resulting in the destruction of larger amounts of short-range order. These conclusions are quite general for all strains. The details of this process will be

discussed in a future paper, but qualitatively we see that it leads to a satisfactory explanation for the maximum in fig. 15.

The pronounced increase in the rate of work hardening with increasing order can be seen in fig. 15 by comparing the flow stresses between the curves after 1, 5 and 10% strain, and as previously discussed is probably due to the decrease in the size of the antiphase domains with increasing plastic deformation. There is a negligible difference in the rate of work hardening between the 0·1 and 1% curves, which is to be expected since these small strains are insufficient to reduce the domain size significantly. The small increase in strength of the fully ordered alloy compared to the disordered alloy has already been mentioned. A possible explanation for this may be that the Ni_3Mn alloy used in this investigation was not at the exact stoichiometric composition so that perfect long-range order was not obtained. Also, the antiphase domain size although large, may still contribute a small amount to the yield stress. A further possibility is that the lattice friction stress for a superlattice dislocation may be larger than that for an ordinary dislocation, although at the present time it is difficult to see how this difference could arise.

In order to gain insight into the mechanisms leading to order strengthening, two sets of wire specimens were allowed to relax isothermally at 400 and 465°C toward their equilibrium values of order for these temperatures. After various time intervals, the specimens were rapidly quenched and tested at room temperature. The results obtained for the various flow stresses are shown in figs. 16 and 17.

Figure 16 for the 400°C anneal shows that the flow stresses increase continuously, reach a slight maximum at 200 hours, and finally attain an equilibrium value after 590 hours. According to Cottrell (1954). this maximum may be related to the attainment of a critical domain size ($\cong 50$ Å) after these times. However, neutron diffraction measurements (Marcinkowski and Brown 1961) indicate that the antiphase domains are appreciably larger than 50 Å after 200 hours of annealing. On the other hand, the model proposed previously to explain the results in fig. 15 should also be applicable in the present case, namely, that the maxima in fig. 16 arise because of a critical combination of long- and short-range order. Figure 16 also shows a marked increase in the rate of work hardening with increasing annealing time, and presumably arises from the decrease in antiphase domain size with increasing strain, as has been previously discussed. This figure also shows that after annealing times of about 140 hours, the alloy becomes relatively brittle, so that plastic strains of only slightly over 5% can be obtained.

Finally, fig. 17 illustrates the manner in which the flow stress varies with time at 465°C. The flow stress continuously increases to a small maximum value at about 8 hours. This maximum is thought to be associated with the resistance offered to dislocation motion by short-range order. As has been previously shown by magnetic measurements (Marcinkowski and Brown 1961), these alloys consist almost completely
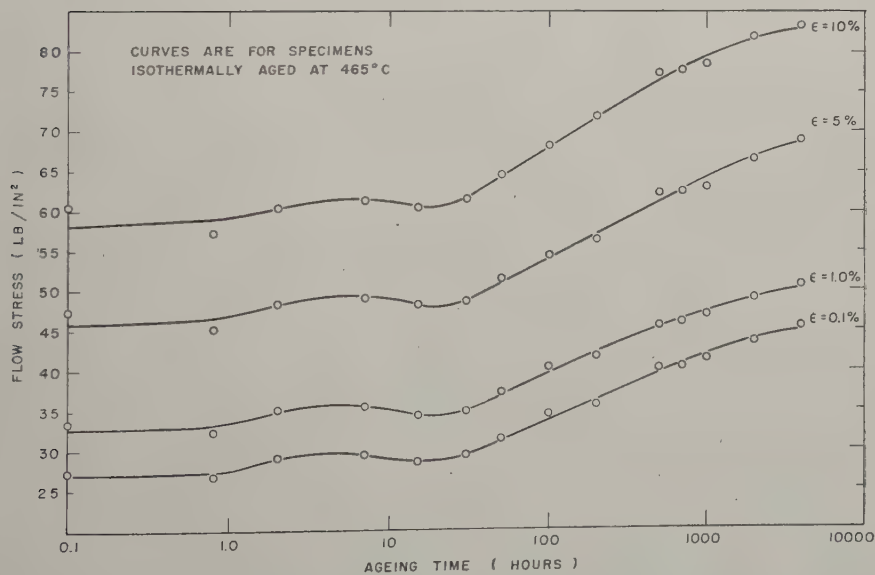
Fig. 16
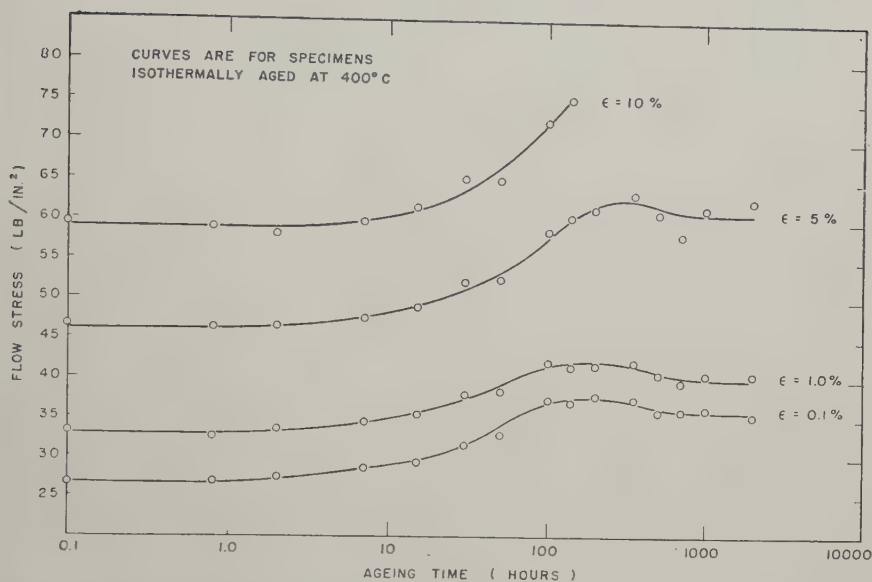
Flow stress as a function of time at 400°c for the plastic strains indicated. Measurements made at room temperature.

Fig. 17

Flow stress as a function of time at 465°c for the plastic strains indicated. Measurements made at room temperature.

of short-range order up to about 10 hours. After longer annealing times, long-range order commences; however, large amounts of short-range order continue to persist, along with long-range order, even after equilibrium is attained (Marcinkowski and Brown 1961), and presumably accounts for the failure of the flow stress to decrease after longer annealing times as was the case in fig. 16.

§ 4. Summary and Conclusions

Using transmission electron microscopy techniques, dislocations in the Ni_3Mn alloy have been found to persist as superlattice dislocations up to temperatures just below the critical temperature for long-range order. In addition the spacing between the dislocation pairs constituting the superlattice dislocation has been found to increase from 179 Å for perfect long-range order to 714 Å just below the critical ordering temperature. This is due to the decrease in the antiphase boundary energy with decreasing degrees of long-range order, and is in good agreement with the results predicted theoretically.

The disordered Ni_3Mn alloy has also been found to possess a relatively low stacking-fault energy of about 20 ergs/cm², which results in wide separations between the pair of partial dislocations constituting the ordinary dislocation when stresses are applied to the thin foils. It has been shown that these widely extended stacking faults act as strong obstacles to the passage of ordinary dislocations. Upon ordering, however, the widely extended stacking faults observed in the disordered alloy are no longer present. This has been shown to result from an effective increase in the stacking-fault energy, which in the ordered alloy has added to it the energy of the antiphase boundary.

In contrast to the disordered alloy, it is found that dislocations in the ordered alloy are generally arranged at random on many closely spaced slip planes. Here again, this phenomenon is postulated to be associated with an effective increase in the stacking-fault energy between the partial dislocations of the superlattice dislocation. In particular, this effective stacking-fault energy is higher by a factor of three than that of the disordered alloy. This increased stacking-fault energy in the ordered alloy in turn allows the superlattice dislocations to cross-slip with relative ease, and thus results in the formation of very fine slip lines.

Finally, measurements of the flow stress with temperature show that it passes through a maximum at about 15°c below the critical ordering temperature. The maximum flow stress at low plastic strains is about twice that value for the flow stress of either the fully ordered or disordered alloys. All of the theories of order strengthening have been considered in an attempt to explain this behaviour; however, they encounter serious difficulties when applied to Ni_3Mn. In view of these difficulties another mechanism for order strengthening has been considered which is associated with the destruction of short-range order that co-exists with long-range order in the partially ordered alloys.

REFERENCES

ARDLEY, G. W., 1955, *Acta Met.*, **3,** 525.

BIGGS, W. D., and BROOM, T., 1954, *Phil. Mag.*, **45,** 246.

BROWN, N., 1959, *Phil. Mag.*, **4,** 693.

COTTRELL, A. H., 1954, *Relation of Properties to Microstructures* (American Society for Metals).

FISHER, J. C., 1954, *Acta Met.*, **2,** 9.

FISHER, R. M., and MARCINKOWSKI, M. J., 1961, *Phil. Mag.* (to be published).

FISHER, R. M., and SZIRMAE, A., 1959, *Special Technical Publication* No. 262 (American Society for Testing Materials), p. 103.

FLINN, P. A., 1960, *Trans. Amer. Inst. min. (metall.) Engrs*, **218,** 145.

HAHN, R., and KNELLER, E., 1958, *Z. Metallkde.*, **49,** 426.

HEIDENREICH, R. D., and SHOCKLEY, W., 1947, *Report of a Conference on Strength of Solids* (The Physical Society), p. 57.

HIRSCH, P. B., 1959, *Metallurg. Rev.*, **4,** 101.

KÖSTER, W., 1940, *Z. Metallkde.*, **32,** 145.

KÖSTER, A., and GMÖHLING, W., 1960, *Z. Metallkde.*, **51,** 385.

KÖSTER, W., and RAUSCHER, W., 1948, *Z. Metallkde.*, **39,** 178.

LAWLEY, A., VIDOZ, E. A., and CAHN, R. W., 1961, *Acta Met.*, **9,** 287.

MARCINKOWSKI, M. J., and BROWN, N., 1961, *J. appl. Phys.*, **32,** 375.

MARCINKOWSKI, M. J., BROWN, N., and FISHER, R. M., 1961, *Acta Met.*, **9,** 129.

MARCINKOWSKI, M. J., FISHER, R. M., and BROWN, N., 1960, *J. appl. Phys.*, **31,** 1303.

MARCINKOWSKI, M. J., and FISHER, R. M., 1960, *Proceedings of the European Regional Conference on Electron Microscopy*, Delft, Holland, **1,** 400.

MENTER, J. W., 1958, *Advanc. Phys.*, **7,** 328.

PEIERLS, R., 1936, *Proc. roy. Soc.* A, **154,** 213.

SEEGER, A., 1957, *Dislocations and Mechanical Properties of Crystals* (John Wiley and Sons Inc.), p. 243.

SUMINO, K., 1958, *Sci. Rep. Res. Insts Tôhoku Univ.* A, **10,** 283.

SWANN, P. R., and NUTTING, J., 1959–60, *J. Inst. Met.*, **88,** 478.

TAOKA, T., and HONDA, R., 1957, *J. Electronmicroscop.*, **5,** 19.

TAOKA, T., and SAKATA, S., 1957, *Acta Met.*, **5,** 61.

TAOKA, T., YASUKOCHI, K., and HONDA, R., 1959, *Trans. nat. Res. Inst. Met.*, **1,** 1.

WHELAN, M. J., 1958, *Proc. roy. Soc.* A, **249,** 114.

WHELAN, M. J., and HIRSCH, P. B., 1957, *Phil. Mag.*, **2,** 1121, 1303.

YANG, C. N., 1945, *J. chem. Phys.*, **13,** 66.

The Precipitation of Lead during Decomposition of Lead Iodide by Electron Irradiation†

By A. J. Forty

H. H. Wills Physics Laboratory, University of Bristol

Abstract

Crystals of lead iodide decompose under electron irradiation into metallic lead and iodine gas. This paper describes the observations which have been made on the mode of decomposition, particularly on the way in which precipitates of lead nucleate and grow inside the parent crystal. At low rates of decomposition the lead precipitates almost uniformly in the form of very small (100 Å–1000 Å in diameter) misoriented crystallites. There is some slight tendency for deposition to occur along dislocations. At high rates of decomposition the lead precipitates in larger platelet form with a definite degree of orientation between the precipitate and the lead iodide. These platelets appear to nucleate and grow within cavities which are produced inside the parent crystal by the electron bombardment. The observations suggest an interesting mechanism for the growth and spreading of decomposition throughout the crystal.

§ 1. Introduction

There have been several reports in recent years of attempts to study the decomposition of crystals by electron microscopy. Those in which decomposition is produced by the electron beam in the microscope itself are particularly interesting, for this allows the progress of the reaction to be followed directly. For example, Sawkill (1955) used the beam of the electron microscope to decompose crystals of silver azide and he was able to follow the process in some detail by electron diffraction and microscopy. A very similar investigation of the structural changes associated with the thermal decomposition of magnesium hydroxide into magnesium oxide and water has been made by Goodman (1958). More recently, Horne and Ottewill (1958) have studied small crystals of silver iodide in a high resolution microscope and have noted some interesting contrast changes in the crystals which might be associated with decomposition.

In all these investigations the resolution of detail in the crystals and their products of decomposition has not been as high as might have been anticipated, chiefly because of difficulties in preparing specimens with suitable dimensions. The specimens should be thin enough for direct transmission microscopy and yet broad enough to allow full use of the resolution of the electron microscope. In an earlier paper (Forty 1960)

---

† Communicated by the Author.

the author has described how crystals of lead iodide can be prepared by growth from solution in the form of very thin platelets, about 1 mm in diameter and a few hundred angstroms in thickness. These are perfectly suitable for this kind of study. Some preliminary observations showed that crystals prepared in this way decomposed during examination in the microscope under high beam densities and high operating voltages. The observations suggested the possibility of making a detailed study of decomposition under electron irradiation, and the results of this study are now reported in the present paper.

One of the most interesting problems associated with the chemical decomposition of crystals is that of explaining how the products of decomposition are accommodated within the parent crystal. In many cases this involves the formation of a new solid phase and the disposal of a gas. It is usually supposed that the solid phase can be accommodated more readily at structural imperfections in the parent crystal, at grain boundaries and dislocations. The work of Mitchell and his colleagues (Hedges and Mitchell 1953, for example) on the photolytic decomposition of silver halides certainly supports this idea. They find that the photolytic silver separates preferentially on dislocations, and this decorating effect can be put into good use for the detection of dislocations. The disposal of gas released by decomposition presents a more difficult problem and in many systems this is thought to restrict the processes of decomposition to such an extent that they occur only in the region of the free surfaces of the crystals.

In the case of transparent crystals direct observations with the optical microscope can lead to some understanding of the mode of decomposition. The work on the photographic process in silver halides provides a good example of this kind of approach. It is possible, however, to gain more detailed information from the use of the electron microscope. For this clearly allows greater resolution for the identification of the habit or morphology of the products of decomposition, and provides the additional technique of electron diffraction which can be invaluable for determination of orientation of precipitates and parent crystal and also, to a limited extent, for chemical identification of new phases.

In the present investigation it has been found that metallic lead formed by decomposition can appear in two forms. At low rates of decomposition the lead precipitates as discrete particles throughout the parent crystal with some preferential deposition on dislocations. Electron diffraction suggests that the precipitates in these cases are in a misoriented or finely divided polycrystalline state. At higher rates of decomposition the lead precipitates inside cavities in the parent crystal. The cavities are created during the electron bombardment and spread out from the centre of decomposition to allow precipitation to take place in the surrounding crystal. In this case the lead separates in the form of well developed platelets with the (111) plane of the f.c.c. lattice parallel to the (0001) plane of lead iodide. These observations are described in detail in the following section.

§ 2. The Observations

The rate of decomposition of a crystal can be controlled fairly easily by varying the intensity of the electron bombardment. This can be done most readily by adjusting the condenser lens to concentrate or spread the electron beam striking the specimen. In the case of the microscope in which the present observations were made (the Philips E.M. 100) it is also possible to apply some coarse control on the rate of decomposition through the operating voltage. The rate of decomposition at normal beam currents varies from very slow at 60 kv, moderate at 80 kv, to very high (often catastrophic) at 100 kv. This is not necessarily an indication of some direct effect of the energy of the incident electrons as it may simply be a result of interaction between the condenser system and accelerating voltage.

Decomposition starts from a point in the crystal, usually defined by the centre of the patch illuminated by the electron beam which is presumably where the beam is most intense. This seems to confirm the idea that the rate of decomposition depends on the flux of electrons striking the crystal. The microstructure of the crystal has no detectable influence on the initiation of the process.

The decomposition of a crystal is a dynamic process, steadily evolving and spreading throughout the whole specimen. In the earlier paper in which the preliminary observations were reported (Forty 1960) it was found convenient to describe the progress of decomposition in a number of stages. In this sense, at any instant, the crystal may be divided into zones of activity. The central, completely decomposed zone is surrounded by a zone in some intermediate state, and this by an outer zone in which the crystal is still in the initial stage of decomposition. These zones gradually spread over the whole crystal.

In the initial stage the crystal undergoes structural rearrangement, by the climb of existing dislocations and the formation of new loops of dislocation. This rearrangement can be associated with the creation of molecular vacancies as a result of the heating produced in the specimen by the electron bombardment. The molecular vacancies are probably created at the centre of the patch illuminated by the beam but subsequently condense in the cooler parts of the crystal. The characteristic features of this climb process have been described elsewhere (Forty 1961).

Chemical decomposition begins in the intermediate stage and reaches completion in the final stage. These two stages are very closely related, since the spreading of the final decomposition proceeds by precipitation of lead in the intermediate zone. The detailed mechanism by which the precipitation develops depends on the rate at which the crystal is forced to decompose. For this reason the observations are best described separately for high rates and low rates in the following way.

2.1. *Precipitation of Lead at Low Rates of Decomposition*

At low beam intensities the crystals decompose very slowly. In this case there is no real distinction between the intermediate and final stages.

A characteristic speckle develops at the centre of illumination and this
eventually spreads over the whole crystal.   Figure 1† is an electron
micrograph of part of a crystal which is decomposing in this way.   The
black speckle is distributed very uniformly through the crystal.   This
part of the specimen contains no dislocations and there are no other obvious
singularities which could account for such a uniform distribution.   Some
confirmation that the speckle represents a precipitation of metallic lead
has been provided by electron diffraction from the area enclosed by fig. 1.
The diffraction pattern, shown in fig. 2, is basically that expected for lead
iodide in the (0001) orientation with additional spots whose radial
displacements correspond to the presence of metallic lead in the (111)
orientation (ref. fig. 9).   These additional spots are streaked into diffraction
rings which might be considered to indicate that the lead is present in a
finely divided and disordered state.   It can be concluded that the speckle
represents a precipitation of metallic lead in the form of very small
discrete particles which are generally misoriented, but have a preference
to lie with the {111} planes in contact with the basal planes of the parent
crystal and with the close-packed directions parallel.

Figure 3 shows part of a crystal which contains dislocations and shows
clearly that the speckle is developing with some preferential growth
along these.   The zig-zag configuration of the dislocations has been
explained by considering that they are screw dislocations which have
climbed into flattened helical form (Forty 1961), and clearly the segments
of the zig-zags must lie predominantly in the edge orientation.   Thus it
is reasonable to assume that the precipitation of lead develops preferentially
along the edge components of dislocations.   After a more prolonged exposure
to the electron beam this form of precipitation produces the cross-hatched
distribution of elongated platelets shown in fig. 4.   The electron diffraction
pattern for this particular area (fig. 5) consists of an array of diffuse spots
superimposed on a series of concentric rings.   Such a pattern can again
be interpreted as that due to a crystalline matrix of lead iodide (spots)
containing a distribution of finely-divided misoriented lead (rings).   It
will be noticed that the principal spots are arranged in pairs having the
same radial displacement from the centre of the pattern.   This has a
trivial explanation : a second crystal lying near that which is decomposing
is producing a second family of spots, and the angular separation in the
pairs simply indicates the rotation between the two lattices.   The
appearance of diffuse spots on the diffraction rings is more significant,
however, since it indicates some degree of preferred orientation for the
small particles of lead.

2.2. *Precipitation of Lead at High Rates of Decomposition*

At higher beam intensities there is a striking change in the mode of
decomposition.   Large, dense crystallites of a new phase appear and grow

---

† With the exception of fig. 9, all figures are shown as plates.

very rapidly at the centre of illumination. It is often difficult to resolve the shapes of these clearly from the mass of crystallites growing in this central region. Figure 6 provides one example, however, where it is possible to see definite triangular or hexagonal platelet forms. This shows an overall distribution of irregular crystallites and a number of larger, sharply defined platelets. The latter are surrounded by highly transparent zones which represent local thinning of the lead iodide, presumably occurring as a result of the extra growth of the crystallites in these regions. This suggests that the final stage of decomposition proceeds by the growth of a large number of small crystallites, followed by the development of large platelets from these by merger and by enhanced decomposition of the lead iodide surrounding them.

The platelets can be identified as metallic lead by electron diffraction. For example, fig. 7 shows part of a decomposing crystal and fig. 8 shows the diffraction pattern obtained for this particular region. The platelets are clearly oriented similarly in the lead iodide and a comparison of the micrograph and the diffraction pattern indicates that their edges follow the close-packed directions $\langle 11\bar{2}0 \rangle$ in the basal plane of the parent crystal. Moreover, the diffraction pattern can be separated into two distinct patterns which are similar but have slightly different radial spacings. These may be identified as a pattern for f.c.c. lead in the (111) orientation superimposed on that for hexagonal lead iodide in the (0001) orientation. An analysis is shown diagrammatically in fig. 9. It can be concluded that the dense crystallites are f.c.c. lead growing in platelet form with a (111) plane in contact with the (0001) plane of lead iodide, and with close-packed directions in the two lattices parallel.

There is an additional feature of some interest in fig. 8. This is the appearance of streaks between $\{11\bar{2}0\}$ spots and $\{10\bar{1}0\}$ spots, producing a six-pointed star. The streaking is most pronounced for the pattern corresponding to lead iodide, but there is a similar though less intense star outside this for the pattern produced by the precipitates. This observation can be considered to indicate some strain in the two lattices, possibly resulting from relative misfit. Such a conclusion requires confirmation, however, by a more detailed analysis of the patterns†.

The growth of crystallites of lead at the centre of decomposition is accompanied by the appearance of sharply defined bright patches having similar lateral dimensions (that is, about one micron across). These, unlike the crystallites, are extremely mobile inside the crystal and rapidly migrate into the intermediate zone. They have a crystallographic outline with edges following $\langle 10\bar{1}0 \rangle$ directions when they are first formed and when they are stationary, but tend to round off and elongate when moving. The patches are generally uniformly bright and remain bright in dark field

---

† *Note added in proof.*—It is now considered that a more likely interpretation would be that the star is formed by streaking from the $\{11\bar{2}0\}$ reflections due to higher order reflection from the edges of the lead platelets and the edges of the cavities in which they grow.

illumination. Two overlying patches have correspondingly increased brightness. This kind of study of the contrast in the image and the behaviour of this as the crystal is tilted into various diffracting conditions indicates that, although there are some diffraction effects controlling the degree of brightness, the greater part of the contrast arises from lack of absorption inside the patches. Therefore the patches probably represent

Fig. 9

(a)   (b)

(c)
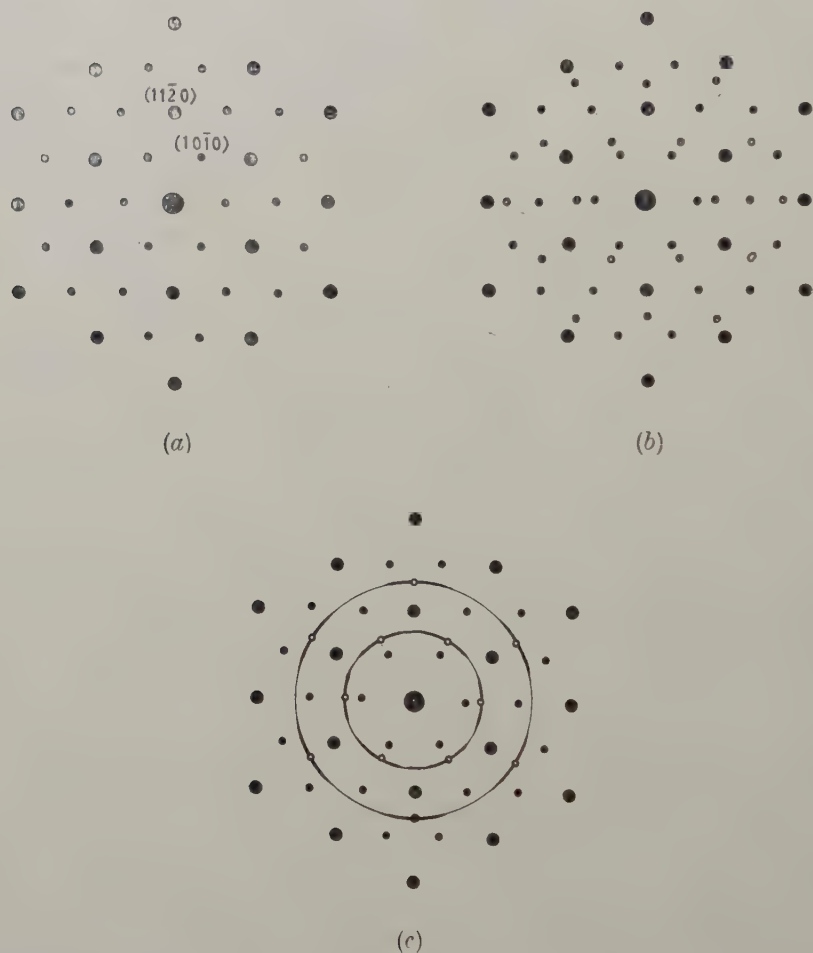
Diffraction patterns for lead iodide and metallic lead. (a) Basic pattern for undecomposed lead iodide in (001) orientation. (b) Pattern for lead iodide in (0001) orientation containing platelets of f.c.c. lead in (111) orientation (black circles represent spots for lead iodide; open circles represent spots for lead). (c) Pattern for lead iodide in (0001) orientation containing crystallites of metallic lead in (111) orientation misoriented about the c-axis of the parent crystal (black circles represent spots for lead iodide; open circles represent spots for lead).

cavities inside the crystal, which show predominantly bright absorption contrast with some lesser diffraction contrast arising from local elastic distortion of the surrounding material. It is estimated from the contrast that the thickness of the cavities is about 50 Å on average, with large variations above and below this value.

The mobility of the cavities can be explained by assuming that they contain some iodine gas which assists an electrolytic transfer of lead iodide under the electric potential gradient impressed on the crystal by the electron bombardment. The crystal is likely to be charged positively during irradiation as a result of secondary emission, and the magnitude of this charge increases with the intensity of the primary electron beam. Thus a positive potential gradient extends radially over the platelet from the centre of decomposition. This can induce an electrolytic flow of lead iodide towards the centre and in this way move the cavities outwards. The potential gradient can exist only under the non-equilibrium conditions associated with intense bombardment and this probably explains why the movement of cavities can be controlled so very readily by adjusting the intensity of the electron beam.

It is difficult to determine the order in which the cavities and crystallites appear at the centre because of the intense activity in this region. Observations made on the spreading of decomposition into the intermediate zone show, however, that the prior presence of cavities is essential for the nucleation of new crystallites in this region. Although the precipitation of lead at low rates of decomposition occurs generally throughout the crystal, with some preferential deposition on dislocations, nucleation and growth appears to occur more readily inside the cavities when these are present at the higher rates.

Figure 10 is an electron micrograph of an area on the fringe of a centre of decomposition which illustrates this mode of precipitation. The centre lies in the upper right-hand corner of the photograph. This contains the characteristic, large, dense crystallites surrounded by denuded bright zones. It is also possible to see some of the bright patches which are thought to represent cavities. These are created in the central zone and then drift outwards through the crystal to form the intermediate zone. Many of the patches expand and elongate during this stage. The micrograph shows a wide range of sizes in the intermediate zone but the large elongated cavities are most noticeable. The movement of the cavities slows down in the intermediate zone and many of them interact with dislocations or other obstacles and remain attached to these. At this stage a new dense phase appears inside them and many examples of this can be seen in fig. 10 (at the places marked A, for example). As this phase grows the cavities tend to move away (as at B) and eventually become completely detached (as at C). The cavities are then free to move away through the crystal and the filling-in process may be repeated elsewhere. The breakaway of a cavity from an associated precipitate is illustrated in more detail in fig. 11 (*a*), (*b*).

The density of the new phase inside the cavities suggests very strongly that this represents a precipitation of lead. It is difficult to confirm this

unambiguously by electron diffraction because the crystallites in the nearby centre of decomposition also contribute to the diffraction pattern. However, if the new phase really represents metallic lead, the observations described above suggest an interesting mechanism for the spreading of the completely decomposed zone through the crystal. Cavities are created at the centre of the illuminated patch. These provide sites for the nucleation and easy growth of platelets of lead. The cavities continue to grow during irradiation and eventually become detached from the platelets. They are then free to move, together with other newly created cavities, into the intermediate zone to provide new sites for the further deposition of lead. In this way the central zone spreads behind a wave of cavities into newly created intermediate zones.

The form of the precipitate depends to some extent on the mobility of the cavities and this, in turn, depends on the microstructure of the crystal. If the crystal contains dislocations the cavities are frequently arrested by these through some mutual elastic interaction. This interaction has been described in detail in the earlier paper (Forty 1960). Cavities which have been arrested in this way appear to grow more rapidly and fill in with lead more easily. The large cavities in fig. 10, for example, are attached to dislocations although these latter are barely visible in the photograph. Figure 12 is a micrograph which shows the attraction of cavities to dislocations more clearly. This part of the crystal contains an array of dislocations which has become distorted into the present configuration by the wave of cavities migrating through it from the upper left-hand corner. It will be noticed that many of the cavities are filling in with lead at this stage.

Figure 13 illustrates the form of precipitation which occurs in the intermediate zone when no dislocations are present in the crystal. The cavities are more mobile in this case and the growth of precipitates is therefore more transient and less complete. The small crystallites left behind by the cavities eventually grow into large platelets in the manner described at the beginning of this section.

One very striking feature of the precipitation in stationary cavities is the smoothness of the interface between the bright and dark phases. This suggests that the lead is precipitated in a highly mobile state so that interfacial equilibrium can readily be attained. The black phase can be caused to shrink or grow by varying the intensity of the electron beam incident on the crystal. For example, fig. 14 (*a*) shows cavities containing lead, whilst fig. 14 (*b*) shows the same field in which the lead has disappeared after a slight displacement of the electron beam to increase the intensity of irradiation locally. Thus the stability of the precipitate appears to depend on the local intensity of irradiation.

This kind of behaviour might be explained if the cavities contain some iodine gas, as suggested earlier to account for their high mobilities. For this will tend to react with lead so that the interface between the two phases represents an equilibrium between lead, iodine gas and lead iodide.

This equilibrium is likely to be disturbed by the changes in pressure of iodine gas in the cavities which might be expected to follow changes in intensity of illumination if the gas is created directly by irradiation.

§ 3. Discussion

The most interesting and perhaps most unexpected result of this investigation is the finding that dislocations play a relatively unimportant part in the precipitation processes. At low rates of decomposition there is some preferential deposition on dislocations, particularly on helical dislocations which provide long edge segments where the lead can be accommodated most readily, but other sites with no obvious singularity occur almost as frequently. At high rates of decomposition the precipitation of lead is controlled principally by the presence of cavities. Dislocations play only a secondary role in this case, through hindering the movement of the cavities and thereby leading to more coherent precipitation. A more pronounced decoration of dislocations by the metallic phase might occur after annealing, but no attempt has been made so far to heat the crystals beyond the temperature reached during electron bombardment.

The larger cavities ($1\,\mu$ in diameter or greater) are most evident in the micrographs illustrating this paper, but a closer inspection reveals many smaller ones ($1000\,\text{Å}$ in diameter or smaller). Small cavities are often found in crystals which contain none of the larger ones. Precipitation of lead can occur in these and this could be responsible for the speckle which appears over the crystals after prolonged periods of less intense irradiation. It is interesting in this connection to note the occurrence of a 'conditioning' effect in such cases. Figure 15 shows a crystal which was torn as it was being mounted on the specimen holder of the microscope. The two parts of this crystal have been subjected to the same form of irradiation but the upper one has developed a speckle whilst the lower one remains undecomposed. This suggests that the nuclei for precipitation are created in one part of the crystal and are free to move within this to produce the uniform distribution found here, but they are not able to cross the tear into the other part. These mobile nuclei might well be very small cavities created at the centre of decomposition which is not shown in the present field of view.

There is no doubt that metallic lead is formed during the decomposition of lead iodide and the observations on cavities in the intermediate stage have provided a very complete picture of the way in which this is accommodated in the parent crystal. There is good reason to believe also that iodine gas is produced at the same time. Some gas probably becomes trapped in the cavities whilst the remainder presumably escapes from the free surfaces of the crystal. It remains to be explained how the lead and iodine are created initially, and how this dissociation is controlled by the intensity of electron irradiation. This is considered below, but any such discussion at this stage must be regarded as purely tentative until more experimental support is available.

One way in which the electron beam might induce decomposition is through the heating of the crystal by the high energy bombardment. That is, the breakdown might be a form of thermal decomposition. Undoubtedly the temperature of the specimen is raised by the electron beam, but estimates of the heating effect produced under the conditions of illumination employed in the microscope indicate that it is unlikely that a temperature of $100\,°c$ is exceeded. No attempt has been made to measure the temperature of the specimen during normal irradiation but some observations have been made with crystals on a heated specimen holder at about $100\,°c$. At low beam intensities where the effect of irradiation is minimized no form of decomposition was found. It can be inferred that decomposition is not due solely to the heating produced during irradiation, but that some more subtle form of interaction is responsible for the chemical changes. This conclusion is necessary also if the bright patches really represent cavities since the creation of these implies a rate of formation of vacancies in excess of that expected for thermal activation.

A form of interaction between the electron irradiation and the crystal which seems satisfactory in a qualitative sense is that of ionization. This idea has been discussed at some length by Groocock and Tompkins (1954) in connection with their study of the decomposition of barium azide under low energy electron bombardment. A more elaborate form of ionization has also been used by Varley (1954) in an attempt to account for the formation of colour centres in alkali halides by x-irradiation. The idea of an ionizing interaction will be examined here mainly in connection with the formation of cavities since this seems to be the most important stage leading to final decomposition.

The most readily produced ionizing interaction in lead iodide is that which converts iodine ions into iodine atoms by the release of electrons. It is interesting to note in this connection that the radius of the iodine atom is about one-half of that of the iodine ion ($1\cdot33\,$Å compared with $2\cdot2\,$Å). The neutral atom should therefore be able to move with great freedom through the lead iodide lattice, especially between adjacent layers of iodine atoms where none of the octahedral interstitial positions is filled by lead ions (see Forty 1960 for a discussion of the structure of lead iodide). Thus, provided there is no recombination between secondary electrons and the iodine atoms, the latter can migrate under thermal activation and diffuse to the free surfaces of the crystal to form iodine gas. This, of course, depends on the recombination time and the jump frequency for the iodine atoms. The iodine ion vacancies produced in this way can trap free electrons to form electron/vacancy complexes and it is possible for these to aggregate into layers one ionic diameter in thickness. Before these can develop into the deep form of cavity which has been observed it is necessary for lead ions as well as iodine atoms to be displaced into the lead iodide lattice. The displaced lead ions will eventually trap electrons of course to produce the lead atoms which ultimately precipitate as metallic lead in the cavities and at the free surface of the crystal.

It is conceivable that lead ions will be displaced into interstitial positions by thermal activation more readily from sites adjacent to newly created iodine ion vacancies. Thus lead ion and iodine ion vacancies might be created simultaneously by a single primary electron. Cavity formation can then proceed by the aggregation and further growth of the lead ion vacancy/iodine ion vacancy complexes. The heating effect of the electron bombardment must play some part in this mechanism in determining the ease with which ions, atoms and vacancies can migrate. This might well account for the strong dependence of the mode of decomposition on the intensity of the electron beam.

Such a model cannot be examined quantitatively at this stage since so many uncertainties exist. It is possible, however, to demonstrate some degree of correlation between the electron flux incident on the crystal and the rate at which vacancies must be produced to account for the observed formation of cavities. The electron flux passing through the crystal is about 10^{17} electrons/cm^2/sec. That is, each ion in the surface layer is in a position to interact with between one hundred and one thousand electrons each second. The rate of production of vacancies necessary to account for the initial formation of cavities at the observed rate is of order 10^{15} vacancies per second per square cm of surface irradiated. Clearly, this can be related to the incident flux of electrons if 1% of the primary electrons produce a single effective ionization.

REFERENCES

FORTY, A. J., 1960, *Phil. Mag.*, **5**, 787; 1961, *Ibid.*, **6**, 587.
GOODMAN, J. F., 1958, *Proc. roy. Soc.* A, **247**, 346.
GROOCOCK, J. M., and TOMPKINS, F. C., 1954, *Proc. roy. Soc.* A, **223**, 267.
HEDGES, J. M., and MITCHELL, J. W., 1953, *Phil. Mag.*, **44**, 223.
HORNE, R. W., and OTTEWILL, R. H., 1958, *J. photogr. Sci.*, **6**, 39.
SAWKILL, J., 1955, *Proc. roy. Soc.* A, **229**, 135.
VARLEY, J. H. O., 1954, *Nature, Lond.*, **174**, 886.

The Critical Temperatures of Binary Alloys with One Magnetic Component

By G. M. Bell and W. M. Fairbairn

Department of Mathematics,
Manchester College of Science and Technology

Abstract

Binary alloys with N_A atoms of component A and N_B atoms of component B on $N_A + N_B$ lattice sites are considered. Component A is ferromagnetic or anti-ferromagnetic with an arbitrary number of Bohr magnetons per atom while B is without magnetic properties. There is a Heisenberg exchange interaction between nearest-neighbour A–A pairs and interaction energies for nearest-neighbour A–B and B–B pairs are introduced. The effect of the local order in the lattice distribution of the A and B atoms on the Curie or Néel temperature is examined both for equilibrium (annealed) alloys where the local order is temperature dependent and for quenched alloys where the lattice distribution is fixed (though not necessarily random). A Bethe-pair (first-order quasi-chemical) statistical approximation is used. It is shown that even though magnetic moments are taken as constant on the A atoms and zero on the B atoms the curves of Curie or Néel temperature against composition vary widely according to the value of the A–B interaction energy and the heat treatment. For quenched alloys there is a critical mole-fraction of A below which there is no spontaneous magnetization; this critical mole-fraction depends on the temperature from which the alloy is quenched. For equilibrium alloys there is also a critical mole-fraction for some values of the A–B interaction parameter but for others a Curie temperature exists for all finite mole-fractions of A. Where A is anti-ferromagnetic there is always a critical mole-fraction below which no Néel temperature exists but its value varies widely. Some relevant experimental results are discussed.

§ 1. Introduction

We shall consider binary mixtures (alloys) of a component A which is ferromagnetic or anti-ferromagnetic in its pure state and a component B which is neither. Numbers N_A of A atoms and N_B of B atoms are distributed on $N = N_A + N_B$ lattice sites and the composition of the mixture will be characterized by either α or c where

$$\alpha = N_B/N_A, \quad c = N_A/N = 1/(1+\alpha). \qquad . \quad . \quad . \quad (1.1)$$

Each A atom has a magnetic moment $2\mu s$, where μ is the Bohr magneton, corresponding to an unpaired spin quantum number s and there is a Heisenberg exchange interaction between nearest-neighbour A atoms on

the lattice. Thus, if the total spin quantum number for a nearest-neighbour pair of A atoms is S and if $e_{AA}{}^{(S)}$ is the interaction energy of such a pair

$$e_{AA}{}^{(S)} - e_{AA}{}^{(0)} = -JS(S+1). \qquad \cdots \cdots (1.2)$$

When the constant J is positive A is a ferromagnetic component (FM) and when J is negative A is an anti-ferromagnetic component (AFM). The exchange interaction between B atoms is zero so that each nearest-neighbour B–B pair has the same energy e_{BB} and each nearest-neighbour A–B pair has the same energy e_{AB}. The interactions between all atoms at distances greater than that of nearest-neighbours are taken to be zero. Also s and J will be taken to be independent of the composition. The assumption that the magnetic moments are independent of composition is applicable to a number of binary alloys (Hoselitz 1952, Crangle and Parsons 1960, Lomer and Marshall 1958) but in many others the electronic structure of both components is affected by the mixing. However, it does seem well worth while to investigate possible effects on the intrinsic magnetization and the critical temperature due to mixing alone and that will be done in this paper.

The properties of the mixture depend on whether the positions of the A and B atoms are fixed on the lattice (frozen distribution) as in a quenched alloy or on whether they can exchange sites on the lattice to reach the equilibrium distribution for the given temperature. In the former case the free energy minimum is attained by re-orientating the spins of the A atoms while in the latter case the degree of short-range order in the positions of A and B atoms will also be affected. Both of these possibilities will be examined (§ 4 and § 5).

The well-known Ising model is obtained from our model by putting $s = \frac{1}{2}$ and by replacing the factor $S(S+1)$ in (1.2) by the more tractable but incorrect expression $4s_{1x}s_{2x}$, where s_{1x} and s_{2x} respectively are the components along a crystal axis of the spin vectors of the atoms of a nearest-neighbour pair. The effects of diluting an Ising model component A by a component B with no exchange interaction have been discussed previously by one of the authors. (Bell 1953, 1958. The case treated at length in the earlier reference is that of super-lattice ordering with addition of a third 'inactive' component; this is equivalent to the dilution of an Ising model.) It was found that for positive values of an energy parameter (equivalent to $e_{AB} - \frac{1}{2}e_{AA}{}^{(0)} - \frac{1}{2}e_{BB}$ of this paper) the curves of critical temperature against atomic concentration c pass through the origin. However, for a frozen distribution the critical temperature becomes zero at a non-zero value of c (Bell 1958). If the frozen distribution is random this value of c is given by $1/(z-1)$, where z is the number of nearest neighbours of an atom on the lattice, and for smaller values of c there is no spontaneous magnetization at any temperature. This result was obtained independently by Sato *et al.* (1959), and we shall show in § 4 that it is true also for the Heisenberg model. Mixtures where the component A is a three-orientation extension of the Ising model corresponding to $s = 1$,

for $z = 12$ and a frozen distribution were also investigated by Bell (1958), and it was found that the curve of critical temperature against c is very close to that obtained for the ordinary (two-orientation) Ising model with $z = 12$.

The results of the statistical method developed by Bethe using a group of $z + 1$ sites were shown by Guggenheim to be obtainable using a group of only two sites and are equivalent to those obtained by the quasi-chemical method (see Fowler and Guggenheim, § 608). The Bethe method, using only two sites, will be termed the 'Bethe-pair method' and applied to the problems treated here, starting in § 2 with a treatment of the pure A component with a general value of s and positive or negative J. The results obtained in § 2 are equivalent to those of the constant coupling method of Kasteleijn and von Kranendonk (1956) (see also Kikuchi 1958). However, the method used here is preferable since it leads to a very much more concise treatment which is suitable for the subsequent extension in § 3 to A–B mixtures.

§ 2. Critical Temperature for the Magnetic Component

In order to include the AFM case it will be assumed that the crystal lattice consists of two sub-lattices (labelled 1 and 2) such that the z nearest neighbours of each atom on sub-lattice 1 all lie on sub-lattice 2 and vice-versa. For a single atom the effect of the rest of the atoms is taken into account by an internal magnetic field which has magnitude H_1 for atoms on 1 and H_2 for atoms on 2. In the FM case $H_1 = H_2$ and in the AFM case $H_1 = -H_2$.

If $Z_1(H)$ denotes the partition function for a single atom then

$$\langle m_1 \rangle_{H_1} = \frac{kT}{2\mu} \frac{d}{dH_1} \{\log Z_1(H_1)\}$$

$$= \frac{kT}{2\mu} \frac{d}{dH_1} \left\{ \log \sum_{m=-s}^{s} \exp (2\mu H_1 m/kT) \right\}, \quad (2.1\,a)$$

where $\langle m_1 \rangle_{H_1}$ denotes the average value of the magnetic quantum number m of the atoms on 1. Similarly

$$\langle m_2 \rangle_{H_2} = \frac{kT}{2\mu} \frac{d}{dH_2} \{\log Z_2(H_2)\}. \quad \cdots \cdots (2.1\,b)$$

We have $\langle m_1 \rangle_0 = \langle m_2 \rangle_0 = 0$.

For a nearest-neighbour pair of atoms, one on each sub-lattice, the corresponding Hamiltonian is

$$\mathcal{H} = \text{constant} - 2J(\mathbf{s}_1 . \mathbf{s}_2) - 2\mu(s_{1x}H_1' + s_{2x}H_2').$$

Since we are interested only in relative energies the constant can be chosen arbitrarily. For FM, $J > 0$, $H_1' = H_2'$ and we choose the constant to be $2Js(2s + 1)$: for AFM, $J < 0$, $H_1' = -H_2'$ and we take the constant to be zero. The internal fields H_1' and H_2' take into account the effect on each

atom of all atoms outside the pair considered. A complete set of states of the pair of atoms is defined by

$$|SM\rangle = \sum_{m_1, m_2} C^{SM}_{sm_1\, sm_2} \;|sm_1\rangle|sm_2\rangle$$

where S takes values from 0 to $2s$, and the coefficients C are the normal vector-coupling coefficients. Then

$$\langle SM|\mathscr{H}|S'M'\rangle = \delta_{MM'}\{[\text{constant} - JS(S+1)]\delta_{SS'}$$
$$-\mu[H_1' + (-1)^{S+S'}H_2']F(S, S', M)\}$$

where $F(S, S', M)$ is non-zero only when $S' = (S-1)$, S or $(S+1)$ and when $S \geqslant 0$, $S' \geqslant 0$. Also $F(S, S', M) = F(S', S, M)$: these relationships, together with

$$F(S, S, M) = M$$

and

$$F(S, S-1, M) = \sqrt{\{(S^2 - M^2)[(2s+1)^2 - S^2]/(4S^2 - 1)\}},$$

determine all the non-zero values of $F(S, S', M)$.

For FM the states $|SM\rangle$ are eigenstates, but for AFM the Hamiltonian in the $|SM\rangle$ representation is diagonal in M but not in S. We must introduce a new quantum number Σ and define the eigenstates

$$|\Sigma M H_1' H_2'\rangle = \sum_{S=|M|}^{2s} \alpha_\Sigma^S(MH_1'H_2')|SM\rangle, \quad M = -2s, \dots, +2s, \text{ and}$$

$\Sigma = |M|, \dots, 2s$, with eigenvalues $E(\Sigma M H_1' H_2')$ of $\mathscr{H}$. Then for FM the quantum numbers Σ and S are identical for all values of the internal fields and

$$\alpha_\Sigma^S(MH_1'H_2') = \delta_{S\Sigma}$$
$$E(\Sigma M H_1' H_2') = \{2Js(2s+1) - J\Sigma(\Sigma+1) - \mu(H_1' + H_2')M\}\delta_{S\Sigma};$$

with $H_1' = H_2'$. For AFM, when $H_1' = -H_2' = H'$, we can expand $\alpha_\Sigma^S(MH', -H')$ and $E(\Sigma M H', -H')$ in powers of H' to obtain

$$\alpha_\Sigma^S(MH', -H') = \left\{\delta_{S\Sigma} \mp \frac{2\mu H' F(\Sigma, \Sigma\pm 1, M)}{J(2\Sigma + 1 \pm 1)}\delta_{S, \Sigma\pm 1} + O(H'^2)\right\} N(H')$$

and

$$E(\Sigma M H', -H') = -J\Sigma(\Sigma + 1) + O(H'^2),$$

where $N(H')$ is a normalizing factor, $N(0) = 1$. Thus when $H' = 0$ the quantum numbers Σ and S are identical.

The partition function for the pair states is

$$Z_2(H_1', H_2') = \text{trace exp}\,(-\mathscr{H}/kt)$$
$$= \sum_{\Sigma M} \exp\,\{-E(\Sigma M H_1' H_2')/kT\},$$

and

$$\langle m_1\rangle_{H_1'} = \frac{kT}{2\mu}\frac{\partial}{\partial H_1'}\{\log Z_2(H_1', H_2')\}, \qquad . \quad . \quad (2.2\,a)$$

$$\langle m_2\rangle_{H_2'} = \frac{kT}{2\mu}\frac{\partial}{\partial H_2'}\{\log Z_2(H_1', H_2')\}. \qquad . \quad . \quad (2.2\,b)$$

To be consistent we require that the average values obtained from (2.1) must equal those obtained from (2.2). Formulae (2.1 a) and (2.2 a) give

$$\frac{\sum_{m=-s}^{s} m \exp\left(2\mu H_1 m/kT\right)}{\sum_{m=-s}^{s} \exp\left(2\mu H_1 m/kT\right)} = \frac{\sum_{\Sigma M} \langle \Sigma M|s_{1x}|\Sigma M\rangle \exp\left\{-E(\Sigma M H_1' H_2')/kT\right\}}{\sum_{\Sigma M} \exp\left\{-E(\Sigma M H_1' H_2')/kT\right\}}$$

. . . (2.3)

where $\langle \Sigma M|s_{1x}|\Sigma M\rangle = \frac{1}{2}\sum_{S,S'} \alpha_{\Sigma}^{S}(MH_1'H_2')\alpha_{\Sigma}^{S'}(MH_1'H_2')F(S,S',M).$

Formulae (2.1 b) and (2.2 b) give an equivalent condition for consistency. Since $\langle m_1\rangle_0 = \langle m_2\rangle_0 = 0$ in either definition this consistency condition is satisfied identically when $H_1 = H_1' = 0 = H_2 = H_2'$. The critical temperature T_1 is obtained by determining that value of T for which the zero internal field solution of the consistency condition is a repeated root. It will, in fact, be a triple root but it is sufficient, because of the symmetry, to require the root to be double: it is then automatically a triple root.

To determine the critical temperature by this procedure a relation is needed between the internal fields for the single atom states and those for the pair states. Since the absolute activities and the partition function contributions due to non-interaction terms are equal for all A atoms the application of the Bethe pair approximation to this situation gives eqn. (2.3) with

$$H_1 = zH_0, \quad H_1' = (z-1)H_0, \quad H_2 = \pm zH_0, \quad H_2' = \pm (z-1)H_0$$

with the + sign for FM, the − sign for AFM. Thus we require

$$\frac{d}{dH_0}\left\{\langle m_1\rangle_{H_1=zH_0}\right\} = \frac{d}{dH_0}\left\{\langle m_1\rangle_{H_1'=-(z-1)H_0,\ H_2'=\pm(z-1)H_0}\right\}$$

when $H_0 = 0$, and a similar equation for $\langle m_2\rangle$ which is satisfied by symmetry. After some simplification we obtain

$$\frac{2\mu z}{kT}\frac{1}{3}s(s+1)\left\{\sum_{\Sigma M}\exp\left[-E(\Sigma M H' \pm H')/kT\right]\right\}_{H'=0}$$

$$= (z-1)\left\{\sum_{\Sigma M}\left[\langle \Sigma M|s_{1x}|\Sigma M\rangle\langle \Sigma M|s_{1x}\pm s_{2x}|\Sigma M\rangle + \frac{d}{dH'}\langle \Sigma M|s_{1x}|\Sigma M\rangle\right]\right.$$

$$\left. \exp\left[-E(\Sigma M H' \pm H')/kT\right]\right\}_{H'=0}.$$

On inserting the expressions obtained previously for $(E\Sigma M H' \pm H')$ and $\alpha_{\Sigma}^{S}(MH' \pm H')$ and remembering that Σ can be replaced by S when $H' = 0$ we obtain

(i) $\quad zs(s+1)\sum_{S=0}^{2s}(2S+1)\exp\left\{[S(S+1)-2s(2s+1)]J/kT\right\}$

$$= 3(z-1)\sum_{SM}\tfrac{1}{2}M^2\exp\left\{[S(S+1)-2s(2s+1)]J/kT\right\}$$

for FM,

(ii) $s(s+1) \sum\limits_{S=0}^{2s} (2S+1) \exp \{S(S+1)J/kT\}$

$$= \frac{3kT}{2\mu}(z-1)\sum_{\Sigma M}\frac{\mu}{J}\left\{-\frac{[F(S,S+1,M)]^2}{S+1}+\frac{[F(S,S-1,M)]^2}{S}\right\}\exp\{S(S+1)J/kT\}$$

for AFM.

Substituting the expression found for $F(S\,S,'M)$ and summing over M gives an equation which determines the Curie temperature in the case of FM and the Néel temperature in the case of AFM. The equation will be written in the form

$$Q(T_1)=0 \qquad \cdot \quad \cdot \quad \cdot \quad \cdot \quad \cdot \quad (2.3)$$

where (i) for FM:

$$2s(s+1)(2s+1)Q(T)=\sum_{S=0}^{2s}\{(z-1)S(S+1)-2s(s+1)\}(2S+1)$$

$$\exp\{[S(S+1)-2s(2s+1)]J/kT\}, \qquad \cdot \quad \cdot \quad \cdot \quad (2.4\,a)$$

and (ii) for AFM:

$$2s(s+1)(2s+1)Q(T)=-s(s+1)\{2z+4(z-1)kT/J\}$$

$$+\sum_{S=1}^{2s}\{(z-1)kT/J-2zs(s+1)\}(2S+1)\exp\{S(S+1)J/kT\}. \quad (2.4\,b)$$

§ 3. The Equilibrium Conditions for Mixtures

We shall now derive the modifications in eqn. (2.3) for the critical temperature of the pure FM or AFM component A which result from mixing with the component B.   Let N_{BB} and $N_{AA}^{(S)}$ denote respectively the total number of B–B nearest-neighbour pairs and the number of A–A nearest-neighbour pairs with spin quantum number $S(S=0,\ 1,\ 2,\ \dots\ 2s)$.   Also let N_{AB} denote the number of A–B nearest-neighbour pairs: it will be assumed that there is no long-range order in the A–B distribution so that $\frac{1}{2}N_{AB}$ of these pairs have the A atom and $\frac{1}{2}N_{AB}$ have the B atom on sub-lattice 1.   As long as the number N of sites is large enough for statistically significant results to be obtained we can neglect boundary effects and assume that

$$\tfrac{1}{2}zN_A=\tfrac{1}{2}N_{AB}+\sum_{S=0}^{2s}N_{AA}^{(S)};\ \tfrac{1}{2}zN_B=\tfrac{1}{2}N_{AB}+N_{BB}. \qquad \cdot \quad \cdot \quad (3.1)$$

The configurational energy is given by

$$E_C=N_{AB}e_{AB}+N_{BB}e_{BB}+\sum_{S=0}^{2s}N_{AA}^{(S)}e_{AA}^{(S)}.$$

Using (1.2), (3.1) and the energy zero defined in § 2

$$E_C(\text{FM})=\tfrac{1}{2}zN_{AA}e_{AA}^{(2s)}+\tfrac{1}{2}zN_{BB}e_{BB}+N_{AB}(e_{AB}-\tfrac{1}{2}e_{AA}^{(2s)}-\tfrac{1}{2}e_{BB})$$

$$+J\sum_{S=0}^{2s-1}[2s(2s+1)-S(S+1)]N_{AA}^{(S)} \quad \cdot \quad \cdot \quad (3.2\,a)$$

and $$E_C(\text{AFM})=\tfrac{1}{2}zN_{AA}e_{AA}^{(0)}+\tfrac{1}{2}zN_{BB}e_{BB}+N_{AB}(e_{AB}-\tfrac{1}{2}e_{AA}^{(0)}-\tfrac{1}{2}e_{BB})$$

$$-J\sum_{S=1}^{2s}S(S+1)N_{AA}^{(S)}. \qquad \cdot \quad \cdot \quad \cdot \quad \cdot \quad \cdot \quad (3.2\,b)$$

At any given concentration the equilibrium conditions are derived for fixed N_A and N_B so that the first two terms on the right of (3.2) are constant and do not appear in the equilibrium equations. Also we shall denote the coefficient of N_{AB} in (3.2) by $-\gamma|J|$. Thus for FM,

$$-\gamma J = e_{AB} - \tfrac{1}{2}e_{AA}^{(2s)} - \tfrac{1}{2}e_{BB} \qquad . \quad . \quad . \quad . \quad (3.3\,a)$$

and for AFM,

$$+\gamma J = e_{AB} - \tfrac{1}{2}e_{AA}^{(0)} - \tfrac{1}{2}e_{BB}. \qquad . \quad . \quad . \quad . \quad (3.3\,b)$$

It follows from (3.2) that in considering probabilities a Boltzmann factor $\beta = \exp\{+\gamma|J|/kT\}$ must be introduced for each A–B pair and for each A–A pair with spin S a factor $\exp\{[S(S+1) - 2s(2s+1)]J/kT\}$ for FM, and $\exp\{S(S+1)J/kT\}$ for AFM (as was done in § 2). Further, due to the internal magnetic field H_1' on sites of sub-lattice 1, the probability of an A–B pair with the A atom on sub-lattice 1 and spin component m must also contain the factor $\exp(2\mu H_1'm/kT)$. When the A atom of the A–B pair is on sub-lattice 2 we must replace H_1' by H_2'. It is therefore convenient to introduce a factor of proportionality ρ defined by

$$\tfrac{1}{2}N_{AB}/N_{AA} = \rho\beta Z_1(H_1')/Z_2(H_1', H_2')$$
$$= \rho\beta Z_1(H_2')/Z_2(H_2', H_1'). \qquad . \quad . \quad . \quad (3.4)$$

This last relation follows because $Z_2(H_1', H_2') = Z_2(H_2', H_1')$ and $Z_1(H_1') = Z_1(H_2')$ for $H_1' = \pm H_2'$.

Since there is no long-range order in the A–B distribution the proportion of A atoms will be the same on each sub-lattice and in place of (2.1 a) and (2.1 b) we have

$$\langle m_1 \rangle_{H_1} = \frac{N_A}{N}\frac{kT}{2\mu}\frac{d}{dH_1}\{\log Z_1(H_1)\} \qquad . \quad . \quad . \quad (3.5\,a)$$

and

$$\langle m_2 \rangle_{H_2} = \frac{N_A}{N}\frac{kT}{2\mu}\frac{d}{dH_2}\{\log Z_1(H_2)\}. \qquad . \quad . \quad (3.5\,b)$$

Other expressions for $\langle m_1 \rangle$ and $\langle m_2 \rangle$ are deduced from the probabilities of the various types of nearest-neighbour pair. In deriving the equations analogous to (2.2 a) and (2.2 b) the A–B pairs as well as the A–A pairs must be considered. Thus

$$\langle m_1 \rangle_{H_1'} = \frac{kT}{2\mu}\left\{\frac{N_{AA}}{\tfrac{1}{2}zN}\frac{\partial}{\partial H_1'}[\log Z_2(H_1', H_2')] + \frac{\tfrac{1}{2}N_{AB}}{\tfrac{1}{2}zN}\frac{d}{dH_1'}[\log Z_1(H_1')]\right\}.$$

From (3.1) and (3.4)

$$\frac{N_{AA}}{N_{AA} + \tfrac{1}{2}N_{AB}} = \frac{N_{AA}}{\tfrac{1}{2}zN_A} = \frac{Z_2(H_1', H_2')}{Z_2(H_1', H_2') + \rho\beta Z_1(H_1')}$$

and

$$\frac{\tfrac{1}{2}N_{AB}}{N_{AA} + \tfrac{1}{2}N_{AB}} = \frac{\tfrac{1}{2}N_{AB}}{\tfrac{1}{2}zN_A} = \frac{\rho\beta Z_1(H_1')}{Z_2(H_1', H_2') + \rho\beta Z_1(H_1')}$$

so that by equating the two expressions for m_1

$$\frac{d}{dH_1}\{\log Z_1(H_1)\} = \frac{\partial Z_2(H_1{'}, H_2{'})/\partial H_1{'} + \rho\beta d Z_1(H_1{'})/dH_1{'}}{Z_2(H_1{'}, H_2{'}) + \rho\beta Z_1(H_1{'})}. \qquad (3.6)$$

An equation which gives the consistency condition for m_2 is obtained from (3.6) by replacing H_1 by H_2 and $H_1{'}$ by $H_2{'}$. It can be proved that when $H_1 = \pm H_2$ and $H_1{'} = \pm H_2{'}$ the two conditions are equivalent so that (3.6) is sufficient.

Using the Bethe pair approximation with

$$H_1 = zH_0, \quad H_1{'} = \pm H_2{'} = (z-1)H_0$$

we can write (3.6.) in the form

$$Z_2(H_1{'}, H_2{'})\frac{dZ_1(H_1)}{dH_1} - Z_1(H_1)\frac{\partial Z_2(H_1{'}, H_2{'})}{\partial H_1{'}}$$

$$+ \rho\beta\left\{ Z_1(H_1{'})\frac{dZ_1(H_1)}{dH_1} - Z_1(H_1)\frac{dZ_1(H_1{'})}{dH_1{'}} \right\} \equiv \mathscr{F}(H_0) = 0.$$

It will be shown (§§ 4 and 5) that $\rho(-H_0) = \rho(H_0)$ so that $\rho'(0) = 0$. From the symmetry properties of Z_1 and Z_2 it follows that $\mathscr{F}(H_0)$ is an odd function and hence $\mathscr{F}'(0) = \mathscr{F}''(0) = 0$. Thus the condition $\mathscr{F}'(0) = 0$ gives a triple root and this is the condition for the critical temperature, T_C. After some simplification this reduces to

$$Q(T_C) = \rho(0)\beta. \qquad \cdots \cdots \cdots (3.7)$$

When A is FM we define $Q(T)$ by (2.4 a) and the exponent γ in $\beta = \exp(\gamma|J|/kT)$ by (3.3 a): when A is AFM, $Q(T)$ is defined by (2.4 b) and γ by (3.3 b). The function $\rho(0)$ is obtained from $\rho(H_1{'}, H_2{'})$ defined in (3.4) by putting $H_1{'} = H_2{'} = 0$. Because of the difference in the energy zero the partition function $Z_2(H_1{'}, H_2{'})$ in (3.4) is different for FM and AFM (see (6.2 a) and (6.2 b)).

§ 4. The Frozen Distribution

When the mixture is cooled rapidly (quenched) the A–B distribution on the lattice is frozen and in this case the numbers N_{AA}, N_{BB} and N_{AB} are temperature independent. It is convenient to define

$$\kappa = \tfrac{1}{2}N_{AB}/N_{AA}. \qquad \cdots \cdots \cdots (4.1)$$

From (3.4)

$$\rho\beta = \kappa Z_2(H_1{'}, H_2{'})/Z(H_1{'}), \qquad \cdots \cdots (4.2)$$

thus bearing out, for the frozen distribution, the previous contention that $\rho(-H_0) = \rho(H_0)$. At the critical temperature $H_0 = 0$ and

$$\rho(0)\beta = \kappa Z_2(0,0)/(2s+1). \qquad \cdots \cdots (4.3)$$

This expression is now substituted in (3.7), and we obtain

(i) for FM:

$$(1+\kappa) \sum_{S=0}^{2s} 2s(s+1)(2S+1) \exp \{[S(S+1) - 2s(2s+1)]J/kT_C\}$$

$$+ (z-1) \sum_{S=0}^{2s} \{2s(s+1) - S(S+1)\}(2S+1) \exp \{[S(S+1)$$

$$- 2s(2s+1)]J/kT_C\} = 0, \quad . \quad . \quad (4.4)$$

(ii) for AFM:

$$2s(s+1)\{(1+\kappa) + (z-1)(1+2kT_C/J)\}$$

$$+ \sum_{S=1}^{2s} \{(1+\kappa)2s(s+1) + (z-1)[2s(s+1) - kT_C/J]\}$$

$$(2S+1) \exp \{S(S+1)J/kT_C\} = 0. \quad . \quad . \quad (4.5)$$

The corresponding results for pure A (2.3 and 2.4) can be derived by putting $\kappa = 0$.

It can be seen by comparing (4.4) with (2.4 a) and (4.5) with (2.4 b) that the critical temperature for a frozen A–B mixture will be the same as that for pure A with lattice coordination number z' given by

$$(z'-1) = (z-1)/(1+\kappa). \quad . \quad . \quad . \quad . \quad (4.6)$$

If the temperature from which the mixture is quenched is high enough for the frozen distribution to be effectively a random one

$$\kappa = N_B/N_A = \alpha = (1-c)/c$$

and

$$z' = c(z-1)+1. \quad . \quad . \quad . \quad . \quad (4.7)$$

This result is the same as that found for a random frozen mixture of an Ising model component with a non-magnetic component by Bell (1958) and by Sato *et al.* (1959). No such simple result was found for the extended Ising model with $s=1$ (Bell 1958). This is because the probabilities of the three spin orientations $(0, \pm 1)$ were considered separately and not merely the average value $\langle m \rangle$. Thus a second equilibrium equation was introduced. The result (4.7) for the Heisenberg model has been obtained independently by Elliott (1960) and by Smart (1960).

If the temperature from which the mixture is quenched is not high enough for the A–B mixing to be random then the value of κ to be used in finding z' must be calculated for each value of c and for each temperature of quenching by the method of the next section. The value of κ will depend also on γ which is a function of the A–B interaction as defined in § 3.

Curves of critical temperature against concentration are shown for the random frozen distribution in figs. 1–6. Examples of curves for mixtures quenched from finite temperatures are given in fig. 1. In the figures the abscissa is c, the atomic concentration of the magnetic component, and the ordinate is T_C/T_1, the ratio of the critical temperature (in °K) at concentration c to the critical temperature T_1 of the pure FM (or AFM) component.
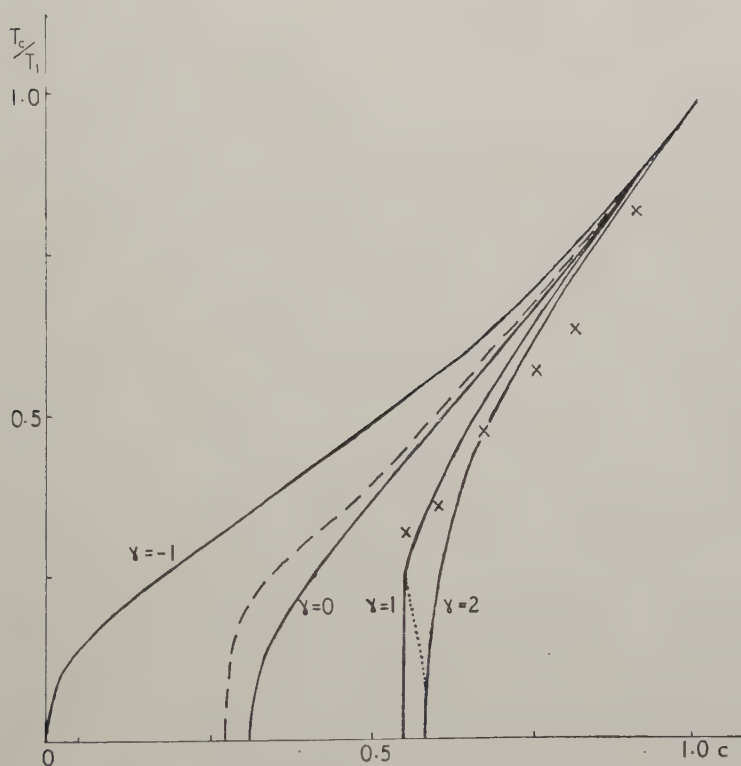
Fig. 1
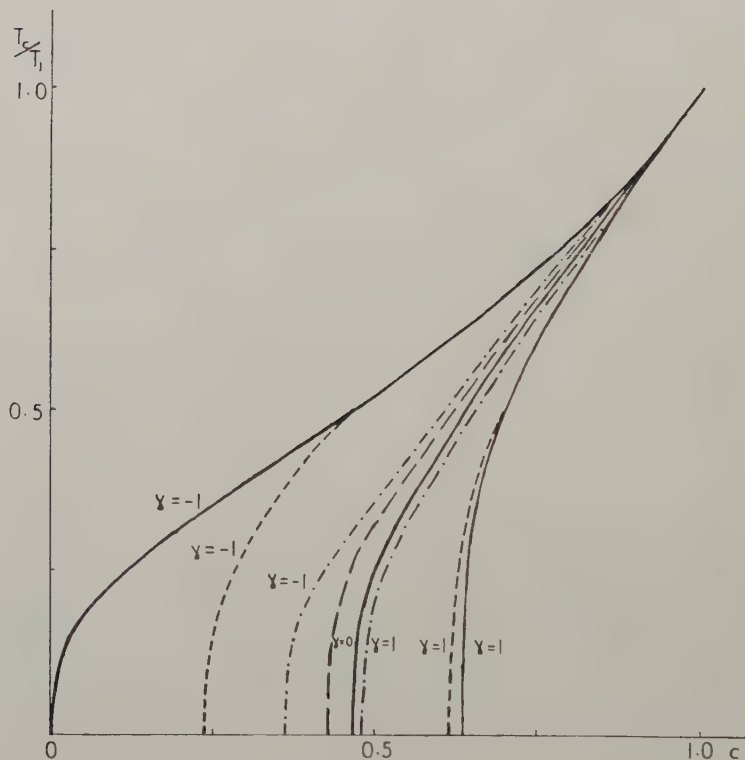
Graphs of critical temperature (T_C) against atomic concentration (c) of magnetic
component for $s = \frac{1}{2}$, $z = 8$, $J > 0$ (FM), for different values of γ. T_1 is
the critical temperature of the pure magnetic component.

———   equilibrium.
— —   random frozen (quenched from infinite temperature).
— · — ·   quenched from temperature $T = 2 \cdot 4\ T_1$.
— — — —   quenched from temperature $T = 0 \cdot 5\ T_1$.

Fig. 2

Graphs of critical temperature against atomic concentration for $s=\frac{1}{2}$, $z=12$, $J>0$ (FM). Experimental points ($\times$) are for Ni–Pt alloys (Marian 1937). ...... unrealizable parts of the theoretical curves. For other details see caption to fig. 1.

Fig. 3
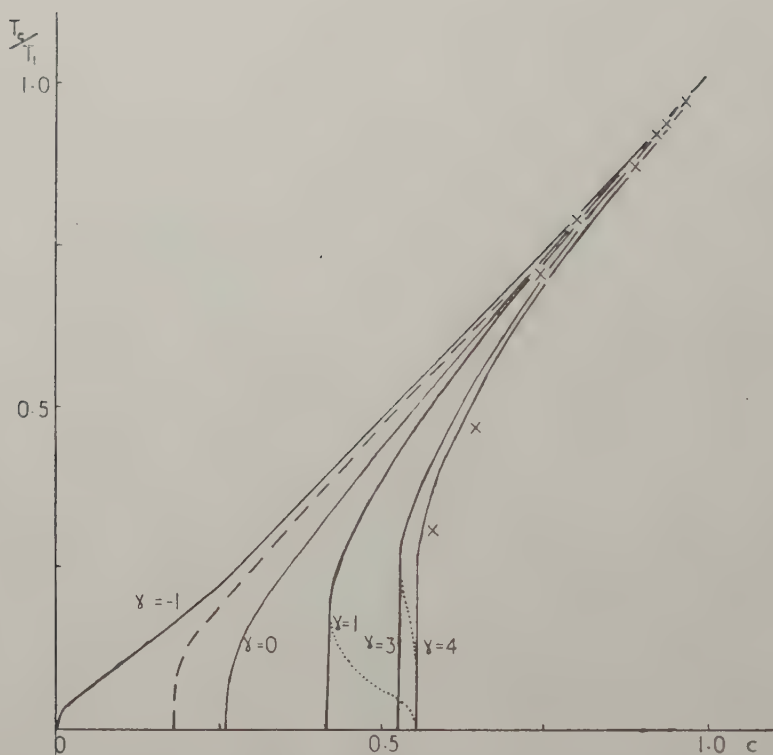
Graphs of critical temperature against atomic concentration for $s=1$, $z=12$, $J>0$ (FM). Experimental points ($\times$) are for Co–Rh alloys (Körster and Horn 1952, Crangle and Parsons 1960). For other details see captions to figs. 1 and 2.

Fig. 4
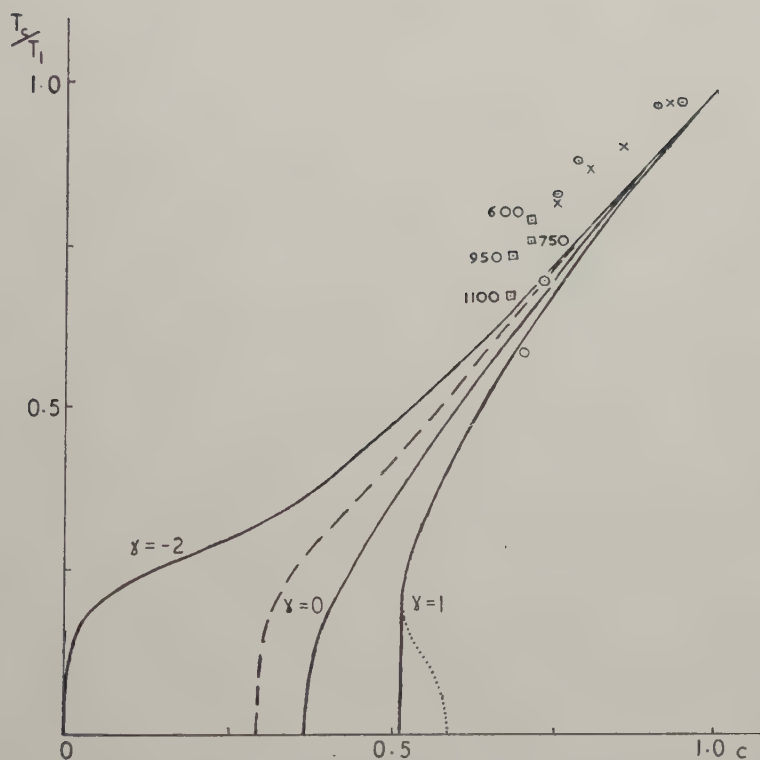
Graphs of critical temperature against atomic concentration for $s=1$, $z=8$, $J>0$ (FM). Experimental points: ($\times$) for Fe–Si (Hoselitz 1952); ($\bigcirc$) for Fe–Al (Suckmisth 1939); ($\square$) for Fe–Si (Guggenheimer *et al.* 1948; the temperature in °C from which the alloy was quenched is given for each point). For other details see previous captions.

Fig. 5
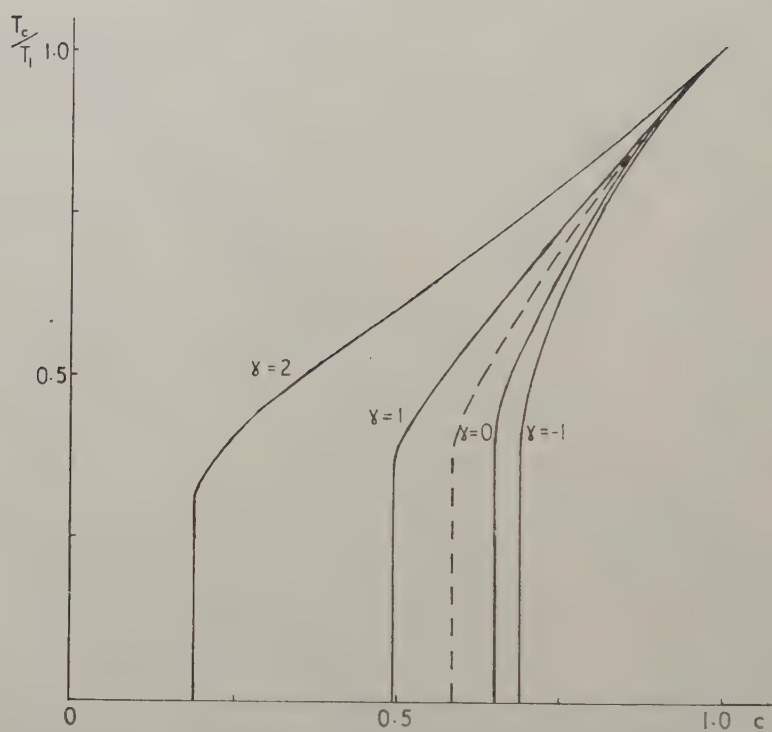
Graphs of critical temperature against atomic concentration for $s=\frac{1}{2}$, $z=8$, $J<0$ (AFM).   For other details see caption to fig. 1.

Fig. 6
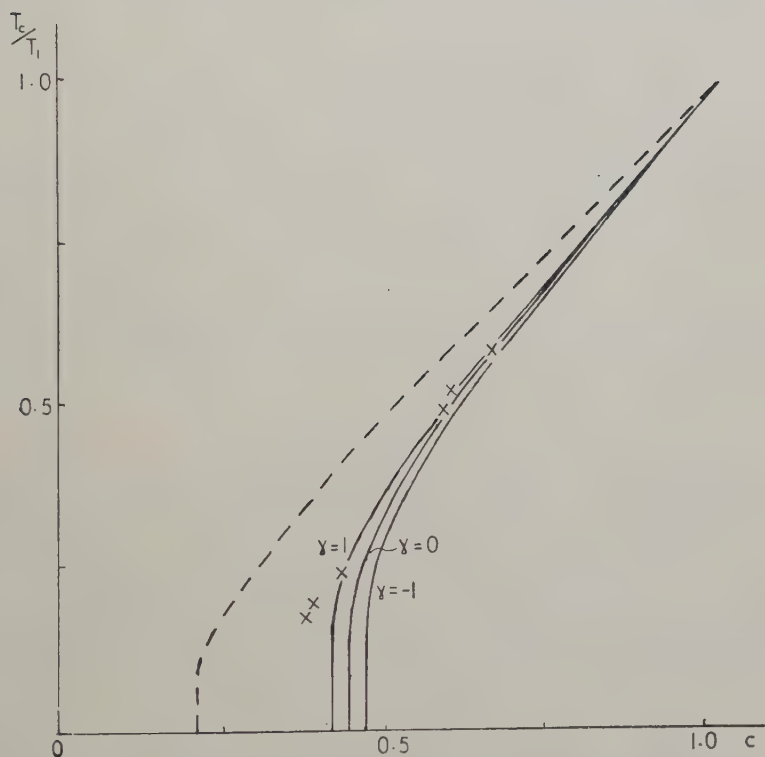
Graphs of critical temperature against atomic concentration for $s = \frac{5}{2}$, $z = 8$, $J < 0$ (AFM). Experimental points: ($\times$) are for Mn–Zn (Baker *et al.* 1960).

§ 5. THE EQUILIBRIUM DISTRIBUTION

In this section we assume that local order can be established by A and B atoms exchanging positions on the lattice, so that N_{AA}, N_{BB} and N_{AB} are functions of temperature. The equilibrium conditions can be derived from a ' Bethe pair ' or ' internal field ' approximation (see Fowler and Guggenheim 1949). If $\lambda = \lambda_A/\lambda_B$, where λ_A and λ_B are the absolute activities of components A and B respectively, an internal field parameter ϵ is introduced by the relation $N_B/N_A = \lambda \epsilon^z$.

It is now supposed that the probability of a B atom appearing on one of a given nearest-neighbour pair of sites, the occupation of the other site of the pair being known, is proportional to $\lambda \epsilon^{z-1}$. Thus

$$\frac{N_{AB}}{N_{AA}} = \frac{2\lambda \epsilon^{z-1} \beta Z_1(H_1')}{Z_2(H_1', H_2')}, \frac{N_{BB}}{N_{AA}} = \frac{\lambda^2 \epsilon^{2z-1}}{Z_2(H_1', H_2')}.$$

From the first of these relations it can be seen that $\lambda \epsilon^{z-1}$ is equal to the parameter ρ defined by (3.4), and the second relation can be written

$$\frac{N_{BB}}{N_{AA}} = \frac{\rho^2}{Z_2(H_1', H_2')}, \qquad \qquad \cdots \cdots \quad (5.1)$$

The case of a regular mixture is obtained formally by putting $s = 0$, so that $Z_1 = Z_2 = 1$. Then (3.4) and (5.1) give the ' quasi-chemical ' formula of the ' Bethe pair ' approximation

$$\frac{N_{AB}^2}{4N_{AA}N_{BB}} = \beta^2.$$

For a general value of s it can be seen from (3.4) and (5.1) that the ' quasi-chemical ' formula is generalized to

$$N_{AB}^2/(4N_{AA}N_{BB}) = \beta^2 \{Z_1(H_1')\}^2/Z_2(H_1', H_2'). \quad \cdots \quad (5.2)$$

The quantity κ defined by (4.1) is no longer temperature independent, but using (3.4) and (5.1) ρ is given by

$$\alpha = \frac{N_B}{N_A} = \frac{N_{BB} + \frac{1}{2}N_{AB}}{N_{AA} + \frac{1}{2}N_{AB}} = \frac{\rho^2 + \rho \beta Z_1(H_1')}{Z_2(H_1', H_2') + \rho \beta Z_1(H_1')}, \qquad (5.3)$$

Thus ρ is defined by the quadratic equation

$$\rho^2 + \rho \beta (1-\alpha) Z_1 - \alpha Z_2 = 0 \qquad \qquad \cdots \cdots \quad (5.4)$$

of which only the positive root

$$\rho = -\tfrac{1}{2}\beta(1-\alpha)Z_1 + \sqrt{\{\tfrac{1}{4}\beta^2(1-\alpha)^2 Z_1^2 + \alpha Z_2\}}$$

is significant. It can be seen from the properties of $Z_1(H_1')$ and $Z_2(H_1', H_2')$ that the substitution of $-H_1'$ and $-H_2'$ for H_1' and H_2' respectively does not affect ρ so that $\rho(-H_0) = \rho(H_0)$ as stated in § 3.

The critical temperature T_c for a given composition (i.e. α) can be obtained by eliminating ρ between (5.3) and (3.7) and solving the resulting equation in T.

§ 6. Curves of Critical Temperature against Concentration

It follows from (4.6) that for the frozen A–B distribution the variation of the critical (i.e. Curie or Néel) temperature with c can be obtained by solving (2.3) for pure A with various values of z. The curves obtained are shown in figs. 1–6 and it can be seen that in each case the critical temperature falls to zero at a non-zero value of c, which will be termed the critical concentration†.

For the equilibrium distribution it is most convenient to consider the parameter $\alpha = (1-c)/c$ as a function of the critical temperature. The equations required are (3.7) together with (5.3). Solving these for α we obtain

$$\alpha = \frac{Q^2 \exp\{-2\gamma|J|/kT_O\} + (2s+1)Q}{Z + (2s+1)Q} \qquad \cdots \quad (6.1)$$

since $Z_1(0) = (2s+1)$. In (6.1) the definition of the symbol Z is

(i) for FM:

$$Z = Z_2(0,0) = \sum_{S=0}^{2s} (2S+1) \exp\{[S(S+1) - 2s(2s+1)]J/kT_C\}. \quad (6.2\,a);$$

(ii) for AFM:

$$Z = Z_2(0,0) = \sum_{S=0}^{2s} (2S+1) \exp\{S(S+1)J/kT_C\}. \qquad \cdots \quad (6.2\,b)$$

In the FM case when $T_C \to 0$,

$$Z \to (4s+1) \quad \text{and} \quad Q \to \frac{(4+1)(sz-2s-1)}{(s+1)(2s+1)}.$$

It can be seen that the behaviour of the Curie temperature–concentration curves at low temperatures depends on the sign of γ. For $\gamma < 0$, $\exp\{-2\gamma|J|/kT\} \to \infty$ as $T \to 0$ and thus $\alpha \to \infty$ as $T_C \to 0$. This implies that the Curie temperature falls to zero only when c becomes zero: the curve of Curie temperature against concentration of ferromagnetic component passes through the origin as may be seen in figs. 1–4. For

$\gamma > 0$, $\exp\{-2\gamma|J|/kT\} \to 0$ as $T \to 0$ and $\alpha(T_C = 0) = (sz-2s-1)/s(z-1)$. Thus the Curie temperature curve meets the c-axis at the point.

$$c = c_0 = s(z-1)/(2sz-3s-1)$$

and for smaller values of c there is no spontaneous magnetization at $T = 0$.

---

† For the random frozen FM mixture it follows from (2.4 a) and (4.7) that $c_0 = (1+1\ s)(z-1)$. However, by expanding the zero-temperature susceptibility for this case as a series of powers of c Elliot *et al.* (1960) have recently deduced that c_0 is independent of s. The variation with s of the Bethe-pair method c_0 for the random frozen FM mixture is thus a measure of the inaccuracy introduced by the approximation. For the body-centred cubic lattice Elliott *et al.* find $c_0 = 0.28$ as against the Bethe-pair values of 0.43, 0.29 and 0.24 for $s = \frac{1}{2}$, 1 and $\frac{3}{2}$ resepctively, while for the face-centred cubic they find $c_0 = 0.22$ as against 0.27, 0.18 and 0.15.

However c_0 is not the lowest value of c for which spontaneous magnetiza-
tion can occur when $\gamma > 0$.   For small positive values of γ the curves will
' bulge ' towards the temperature axis as can be seen for $\gamma = 1$ in figs. 2, 3.
If α, as given by (6.1), is expanded in powers of $\eta = \exp\{-J/kT\}$
then for $\gamma < 2s$ the first term in η is

$$\frac{[zs - (2s + 1)]^2(4s + 1)}{s(s + 1)(2s + 1)^2(z - 1)}\eta^{2\gamma};$$

but, if $\gamma > 2s$, the first term in η is

$$-\frac{2(s + 1)(4s + 1)}{s^2(4s + 1)(z - 1)}\eta^{4s}.$$

Thus, since small η corresponds to small T, for $\gamma > 2s$ the critical curve
for small T_C lies to the right of the vertical tangent at the point $T_C = 0$,
$c = c_0$, while for $\gamma < 2s$ it lies to the left of the tangent and there is a range
of values of c below c_0 for which there exists both an upper and lower
critical temperature.   The influence of higher terms in the series expansion
can cause this latter effect to occur even for $\gamma > 2s$ (see fig. 3 with $\gamma = 3$).
However, it seems that for high enough positive values of γ the critical
temperature will increase monotonically with c and it may be that the
' bulge ' towards the temperature axis for small positive γ and the result-
ing lower critical temperatures for a small range of c are due to the
approximations used and are physically unrealizable.

In the AFM case, although when $T_C \to 0$, $z \to 1$ and $Q \to -z/(2s + 1)$,
eqn. (6.1) is not valid for low values of T_C since we require $Q(T_C) > 0$.
This is associated with the occurrence of a lower critical temperature
even in the case $c = 1$.   Thus in the AFM case each critical curve consists
of an upper branch of Néel points and a lower branch of anti-Néel points
(i.e. lower critical temperatures).   These two branches both start at
$c = 1$ and meet at the point where the tangent to the critical curve is
vertical.   The lower branch can have little physical significance and is
not shown on fig. 5 or 6 where the curves of Néel temperature against
concentration consist of the upper branch and part of the vertical tangent.
The value of c at the meeting point of the branches may be regarded as a
critical concentration since there are no critical temperatures for lower
values of c.   However, values of the critical concentration are likely to be
less accurate than in the FM case where the critical curve actually meets
the c-axis.

§ 7. Discussion

It has been found that the degree of local order has a considerable
effect on the variation of the Curie or Néel temperature with composition.
Where there is local equilibrium on the lattice the variation of the critical
temperature depends on the parameter γ which is related to the A–B
interaction energies.   For FM there is an important difference between
the curves of critical temperature against concentration for $\gamma < 0$ and
$\gamma \geqslant 0$.   In the former case the curves pass through the origin so that a
Curie point exists for any value of c: in the latter case there is a critical

concentration and no Curie point exists for smaller values of c. For AFM there is a critical concentration for all values of γ and this decreases as γ increases.

Positive values of γ correspond to a tendency for the development of long-range order (superlattice formation) which would probably enhance the short-range order effects considered here. Negative values of γ correspond to a tendency for phase separation to occur and this means that in full equilibrium a part of the critical temperature against concentration curve might not be realizable. (A model equivalent to a mixture of an Ising ferromagnetic with a non-magnetic component was examined by Bell (1953) and it was found that, for the values of the A–B interaction parameters considered, separation occurred into phases with and without spontaneous magnetization and rich in the Ising and the other component respectively.)

Local order effects also cause variation in the critical temperature according to the heat treatment applied to the specimen and it is found that in quenched alloys where the A–B distribution is frozen at a particular temperature there is always a critical concentration below which there is no critical temperature (see fig. 1). In general, for $\gamma > 0$ quenched alloys have higher Curie temperatures than equilibrium alloys while for $\gamma < 0$ the reverse is true.

It is of interest that these phenomena occur with the simple dilution model used in which the magnetic moments are localized on the atoms of type A and are of constant magnitude. The concept of localized magnetic moments is supported by experiments on neutron diffraction (Shull and Wilkinson 1955). Also there are a number of alloys in which the magnetic moment on the atoms of the ferromagnetic component does remain constant, at least for small solute concentrations (Hoselitz 1952, p. 138, table II, Lomer and Marshall 1958, Crangle and Parsons 1960, who ascribe 'zero valency' to the solute in such cases). The ferromagnetic metal for which this type of mixing is most frequent is iron, but even so it is found that for $c < 0.9$ the magnetic moment per iron atom begins to fall: this is shown clearly by Parsons *et al.* 1958, in fig. 4 for Fe–Al and in fig. 5 for Fe–Si. Furthermore the A–B interaction may be too complicated for representation by our single parameter γ; for example, in Fe–Si there is segregation between an ordered solid phase of composition Fe_3Si and the intermetallic compound FeSi. The model used must therefore be regarded as an idealization but it is important in that it shows the possibility of wide variation in the curves of critical temperature against concentration without any variation of the magnetic moment on the atoms of the magnetic component and with zero moment on the atoms of the other component.

Some of the available experimental results for solutes with 'zero valency' are plotted in the accompanying figures with the relevant value of z and the nearest value of s. Nickel has 0.6 Bohr magnetons per atom and the Curie points measured by Marian (1937) for Ni–Pt are

shown in fig. 2.   At around $c = 0.75$ superlattice formation occurs (Hansen 1958) so that the Ni–Pt interaction corresponds to $\gamma > 0$. Marian found also that annealed alloys with c between 0.69 and 0.79 have Curie temperatures which are $20°$–$40°$c lower than those of quenched alloys of the same composition.   This agrees with the theoretical deductions which we have made about the effect of heat treatment.

Cobalt has 1·7 Bohr magnetons per atom and the Curie temperatures measured for the α-structure of Co–Rh by Crangle and Parsons (1960) and Körster and Horn (1952) are plotted in fig. 3.   The points obtained from the latter authors are for the lower values of c and presumably refer to quenched alloys since the α-structure is metastable in this region. Their data suggest a cut-off concentration c lying between 0.4 and 0.5: such a value is of the same order as that to be expected for a quenched alloy with $\gamma > 0$.

Iron has 2·2 Bohr magnetons per atom and some points for Fe–Si and Fe–Al are shown in fig. 4.   For Fe–Si Guggenheimer *et al.* (1948) found that with c less than about 0.8 the Curie temperature at a given composition increases as the temperature from which the alloy is quenched decreases.   As mentioned above it is difficult to give a sign to the interaction parameter γ for Fe–Si on the basis of phase behaviour, but this increase of the Curie temperature with decreasing randomness of distribution corresponds to $\gamma < 0$.   However, if these results are accepted the discrepancies between the Curie temperatures obtained by Fallot (1936) and by Parsons *et al.* (1958, fig. 5) for the same system can hardly be attributed to the differences between their heat treatments of the specimens.   For Fe–Al Parsons *et al.* (1958, fig. 4) show that their measured Curie temperatures for quenched alloys down to $c = 0.788$ lie on the same curve as Curie temperatures obtained for annealed alloys by Fallot (1936) and by Sucksmith (1939), although the behaviour of the spontaneous magnetization below the Curie temperature does depend on the heat treatment.   Sucksmith showed that at $c = 0.7$ the replacement of 3·6% of the Fe by Ni causes the Curie temperatures for quenched and annealed alloys to differ by as much as $160°$c.   In both cases shown on fig. 4 the curvature of a line drawn through the experimental points would be far greater near $c = 1$ than for any of the theoretical curves.   In part this may be due to the neglect of A–B superlattice formation in the theory which also, since a Bethe pair approximation is used, underestimates even short-range order effects.   Any more refined mathematical treatment (which would be considerably more complicated) could hardly account for the difference between the gradient of the experimental Curie temperature curve at $c = 1$ for the alloys just discussed and that observed for Fe–V.   Here, although the magnetic moment decreases initially with concentration of vanadium according to the simple dilution law, the Curie temperature increases to a maximum at about $c = 0.85$.   However at $c = 0.6$ the alloy is not FM down to $4.2°$K. indicating the existence of a cut-off concentration (Hansen 1958).

The recent results of Baker *et al.* (1960, private communication) for Mn–Zn mixtures are used for comparison in the AFM case; these are plotted in fig. 6. The experimental points for low temperatures are doubtful and so, of course, are the low temperature parts of the theoretical curves (see § 6). For $c > 0.4$ the experimental points lie very close to the $\gamma = +1$ curve.

There has been some work with alloys with a low concentration of the FM component. Kaufmann *et al.* (1945) investigated quenched gold-rich Fe–Au alloys and Arrott (1958) has shown that the results indicate a cut-off concentration above $c = 0.032$. Similar results on Ni–Au alloys show a cut-off concentration at about $c = 0.4$.

Finally some comment should be made on the results found by Crangle (1960) with palladium-rich Fe–Pd alloys though these are not one of the ' simple dilution ' systems which we have so far discussed since palladium is not a zero-valency solute. The curve of Curie temperature against concentration passes through the origin as in our curves for $\gamma < 0$. However, since superlattice formation occurs the Fe–Pd interaction must be attractive, corresponding to $\gamma > 0$. Our results therefore confirm Crangle's conclusion that the existence of Curie temperatures for very low iron concentrations is due to the appearance of magnetic moments on the palladium atoms.

ACKNOWLEDGMENTS

REFERENCES

ARROTT, A., 1957, *Phys. Rev.*, **108**, 1394.
BELL. G. M., 1953, *Trans. Faraday Soc.*, **49**, 122; 1958, *Proc. phys. Soc.*, **72**, 649.
CRANGLE, J., 1960, *Phil. Mag.*, **5**, 335.
CRANGLE, J., and PARSONS, D., 1960, *Proc. roy. Soc.* A, **255**, 509.
ELLIOTT, R. J., 1960, *J. Phys. Chem. Solids*, **16**, 165.
ELLIOTT, R. J., HEAP, B. R., MORGAN, D. J., and RUSHBROOKE, G. S., 1960, *Phys. Rev. Letters*, **5**, 366.
FALLOT, M., 1936, *Ann. Phys.*, *Paris*, **6**, 305.
FOWLER, R., and GUGGENHEIM, R. A., 1949, *Statistical Thermodynamics* (Cambridge: University Press).
GUGGENHEIMER, K. M., HEITLER, H., and HOSELITZ, K., 1949, *J. Iron St. Inst.* **158**, 192.
HANSEN, M., 1958, *Constitution of Binary Alloys* Second edition (New York: McGraw-Hill).
HOSELITZ, K., 1952, *Ferromagnetic Properties of Metals and Alloys* (Oxford: University Press).
KIKUCHI, R., 1958, *Ann. Phys.*, *N.Y.*, **4**, 1.
KÖRSTER, W., and HORN, E., 1952, *Z. Metallk.*, **43**, 444.
LOMER, W. M., and MARSHALL, W., 1958, *Phil. Mag.*, **3**, 185.
MARIAN, V., 1937, *Ann. Phys.*, *Paris*, **7**, 459.

PARSONS, D., SUCKSMITH, W., and THOMPSON, J. E., 1958, *Phil. Mag.*, **3,** 1174.
SATO, H., ARROTT, A., and KIKUCHI, R., 1959, *J. Phys. Chem. Solids.* **10, 19.**
SHULL, C. G., and WILKINSON, M. K., 1955, *Phys. Rev.*, **97, 304.**
SMART, J. S., 1960, *J. Phys. Chem. Solids*, **16,** 169.
SUCKSMITH, W., 1939, *Proc. roy. Soc.* A, **171,** 525.

Vacancy Trapping in Quenched Aluminium Alloys

By K. H. Westmacott and R. S. Barnes

Atomic Energy Research Establishment, Harwell

D. Hull

Department of Metallurgy, The University, Liverpool

R. E. Smallman

Department of Physical Metallurgy, The University, Birmingham

Abstract

Foils of some aluminium-based alloys have been given various quenching treatments and the size and distribution of the vacancy clusters observed in an electron microscope. It is concluded that the solute atoms trap the vacancies and that their binding energies determine both the scale of the clusters and the number of vacancies they contain.

§ 1. Introduction

There are many examples in the behaviour of dilute solid solutions in which the association of lattice vacancies with solute is thought to play a prominent role. As long ago as 1939 Johnson suggested the importance of 'association' while considering the problem of diffusion in dilute alloys, the binding of vacancies to the solute atoms increasing the mean jump rate of the latter. More recently, there has been a growing interest in the annealing-out of point defects from irradiated and quenched metals to sinks such as dislocation lines and grain boundaries. In this respect Lomer and Cottrell (1955) have emphasized the importance of small quantities of impurity atoms in trapping the vacancies. Such trapping of point defects has been observed in irradiated dilute copper alloys (Blewitt *et al.* 1957, Martin 1960). It is also known that the kinetics of age hardening are extremely sensitive to quenching conditions and solute content; e.g. the rate of 'zone' formation in aluminium–copper alloys at room temperature is 10^7 times faster than the diffusion coefficient extrapolated from the high temperature value and this is thought to be a direct consequence of quenched-in vacancies (De Sorbo *et al.* 1958, Federighi 1958, Smallman *et al.* 1959) as first suggested by Seitz (1952).

Although these experiments indicate the possible interaction of solute atoms and vacancies, no direct evidence of association has been obtained. It is now possible, however, using transmission electron microscopy, to observe the numerous small dislocation loops which result from the excess vacancy concentration (Hirsch *et al.* 1958) and the present experiments were

designed to obtain more direct evidence of the association of vacancies with impurity atoms. This was done by studying the effect of quenching on various aluminium alloys.

§ 2. Experimental Procedure

The binary aluminium-based alloys listed in table 1 were prepared from super-pure metals. The case material was reduced to foils 0·001 in. thick, by alternate rolling (50% reduction in thickness) and homogenization.

Table 1. Solute additions in binary aluminium alloys, atomic per cent

Zn	Cu	Ag	Mg	Si
1·2	0·04	5·4	1·2	0·2
	1·3		3·5	0·4
	1·8		7·3	1·2

All the foils were suspended in a nichrome wire cage adjacent to a thermocouple in a vertical tube furnace and solution treated for two hours at the desired temperature, before being dropped a distance of nine inches into the quenching medium. The solution treatment temperature was between 450°C and 650°C, but 550°C was normally used. A variety of quenching media was used, including brine, distilled water and silicone oil. Subsequent thinning was in Lenoirs solution at 70°C and examination of the foils made in either a Philips or Siemens electron microscope. In estimating the concentration of vacancies from the electron micrographs a constant foil thickness of 5000 Å was assumed.

§ 3. Results

All the alloys contained quenched-in defects in the form of either prismatic loops (Hirsch *et al.* 1958), sessile loops (Smallman 1960) or helical dislocations (Smallman *et al.* 1959, Thomas and Whelan 1959). Figure 1 (*a*)† shows prismatic and sessile loops (A) in the same field of the 3·5% magnesium alloy. The fringe contrast inside the loops marked A indicates that the dislocation line surrounds a stacking fault and is therefore of the Frank sessile type. Sessile loops have not previously been observed in aluminium or its alloys since the high stacking-fault energy favours the formation of prismatic loops (Hirsch *et al.* 1958). In this alloy the stability of the fault may be attributed to the local clustering of solute atoms which presumably lowers the stacking-fault energy or locks the defect by a Suzuki mechanism. These sessile loops are stable at room temperature, but on heating in the beam of the microscope some of them change to prismatic loops as shown at A in fig. 1 (*b*). Figure 2 shows both prismatic loops and helical dislocations in a 1·2% silicon alloy and illustrates the comparative

---

† All figures are shown as plates.

difficulty of nucleating dislocation loops. The helical dislocations are larger than the loops seen in the background (A) suggesting that the helices were formed before the loops. Large individual loops (B) are also present, but these have almost certainly formed by the breakdown of helices as discussed previously (Westmacott *et al.* 1959).

The size and density of the defects found in the alloys varied with different quenching treatments, and in some conditions no defects were observed at all. Thus, for example, in both the higher concentration magnesium and silicon alloys, quenched into water or brine at room temperature, no defects were observed. When the specimens are quenched many of the excess vacancies are lost to existing dislocation lines and grain boundaries and there is a zone free from loops around these sinks (Hirsch *et al.* 1958). During slow quenches the width of the zone is appreciable and in the extreme case all the vacancies are lost to sinks and no loops are formed. This did not happen in these experiments, however, as even during the slowest quench, i.e. into silicone oil or hot water, there were still many loops formed. In estimating the number of vacancies from the size and density of loops it is therefore important that measurements are taken away from permanent sinks. The results, for the 1·2% silicon alloy quenched from 550°C into water between 20°C and 100°C, listed in table 2, indicate that not all the excess vacancies are precipitated.

Table 2.   Al–Si (1·2%).   Quenched into water from 550°C

Water temp. (°C)	Number of loops (cm^{-2} × 10^{-9})	Average diameter (Å)	Vacancy concentration (× 10^5)
100	3·0	800	7
90	3·2	500	3
80	3·6	500	3
70	3·0	300	1
60	4·0	400	2
50	3·6	250	0·7
40	5·4	250	1·2
35	2·4	100	0·1
30	0	0	0
20	0	0	0

When the alloy is quenched into water at 30°C and below no loops are seen, but above this temperature the number of loops is virtually constant. However, the diameter of the loops steadily decreased with increasing severity of the quench and it follows that less vacancies are coming out of solution†. This suggests that if the quenching rate is lowered sufficiently all the excess vacancies will be precipitated.

---

† The unobserved vacancies may exist either individually or as small clusters but it is assumed for the sake of clarity that the former is true.

When any of the quenched silicon alloys are heated to 150°C then many small black dots (~ 60 Å in diameter) are seen, fig. 3. These may be either vacancy clusters or clusters of silicon atoms. After heating at 200°C extensive precipitation of silicon occurs in the form of triangular shaped platelets on $\{111\}$ planes, fig. 4. These have probably formed by the precipitation of silicon on vacancy platelets when they would reduce the Burgers vector of the equivalent dislocation loop and would produce an internal contrast similar to that of stacking faults. Other precipitates appear in the form of needles in the $\langle 110 \rangle$ direction.

In pure aluminium quenched from 550°C the concentration of vacancies was 1×10^{-4} after quenching into brine, water and silicone oil; the width of the denuded zone around dislocations and grain boundaries increased with decreasing quenching rate. As mentioned above, the number of vacancies that have precipitated in loops in the alloys was sensitive to quenching conditions, but even under the optimum conditions the vacancy concentration was never greater than 2×10^{-4}. Because of the inherent difficulties in determining the concentration of vacancies by this method it was not possible to detect any systematic variation in the maximum vacancy concentration for different alloys with equivalent solute contents, however there was a marked variation in the scale of the vacancy precipitation; the diameter of the loops in alloys quenched from 550°C into silicone oil decreased from 1500 Å in pure aluminium to 250 Å in the silicon alloy in the following order of solute additions, viz. zinc, copper, silver, magnesium, silicon. This is illustrated for some of the alloys in fig. 5.

§ 4. Discussion

The concentration of vacancies precipitated from pure aluminium during quenching from 550°C is about 10^{-4}, which is in reasonable agreement with that expected from the Arrhenius type equation

$$C_v = A \exp\left(-E_f/kT\right) \qquad . \quad . \quad . \quad . \quad . \quad . \quad (1)$$

where C_v is the concentration of vacancies at temperature T and E_f is the activation energy for the formation of vacancies (0·75 ev in pure aluminium). In a dilute face-centred cubic alloy in which there is association between the solute atoms and vacancies the concentration of vacancies will be modified by an amount which depends upon the binding energy E_b according to the equation (Lomer 1957)

$$C_v' = A \exp\left(-E_f/kT\right)\left[1 - 12c + 12c \exp\left(E_b/kT\right)\right] \qquad (2)$$

where c is the atomic concentration of solute atoms. Thus the ratio of the concentration of vacancies in equilibrium in the alloy to that in the pure metal is $[1 - 12c \exp\left(E_b/kT\right)]$ and table 3 gives values of this ratio at 550°C for various values of c and E_b.

The concentration of vacancies in equilibrium at 20°C is only about 10^{-13} (eqn. (2)) so that on quenching there will be an excess of vacancies

which will either precipitate or remain in supersaturation. The distribu-
tion of vacancies between the solute and aluminium atoms will vary with
temperature and for any given temperature T is given by

$$12c/(1-12c)\exp(E_b/kT).$$

Values of this distribution ratio at 20°C and 550°C for a number of values of
c and E_b are given in table 4. Thus, for example, for a solute concentration
of 1 atomic per cent with a binding energy of 0·1 ev there will be approxi-
mately 13 times more vacancies associated with solute atoms at 20°C than
at 550°C.

Table 3. Values of C_v'/C_v for different values of c and E_b at 550°C

Concentration of solute atoms, atomic per cent (c)	C_v'/C_v 550°C	
	$E_b = 0 \cdot 1$ ev	$E_b = 0 \cdot 2$ ev
0·5	1·2	2·0
1·0	1·4	2·9
1·5	1·5	3·9
2·0	1·7	4·8
5·0	1·9	10·6

Table 4. Distributions of vacancies between solute atoms and aluminium
atoms. $12c/(1-12c)\exp(E_b/kT)$ at 550°C and 20°C for different
values of c and E_b

Concentration of solute atoms, atomic per cent (c)	$12c(1-12c)\exp(E_b/kT)$ 550°C		$12c/(1-12c)\exp(E_b/kT)$ 20°C	
	$E_b = 0 \cdot 1$ ev	$E_b = 0 \cdot 2$ ev	$E_b = 0 \cdot 1$ ev	$E_b = 0 \cdot 2$ ev
0·5	0·27	1·16	3·50	191
1·0	0·58	2·47	7·42	407
1·5	0·95	4·00	12·0	658
2·0	1·37	5·83	17·5	960
5·0	6·45	27·3	81·9	4471

It follows from the above arguments that on quenching an alloy the
first process to occur will be the redistribution of vacancies between solute
atoms and aluminium atoms and this would happen at all quenching rates.
It is also to be expected that those vacancies which lie near to permanent
sinks (e.g. dislocations and grain boundaries) will be annihilated. Further-
more, because of the high supersaturation of the vacancies, the nucleation
of dislocation loops by the clustering of vacancies will also occur and these

dislocations will in turn act as sinks for further vacancies. Clearly, the number of vacancies that are precipitated in this way during the quench will be a function of the number of loops that are nucleated, and the mobility of the vacancies. The nucleation of loops will depend upon many factors (e.g. supersaturation, quenching rate, diffusion coefficient, etc.); while the mobility of a vacancy will be affected by the magnitude of the binding energy between the solute atoms and the vacancies. Hence, as the binding energy increases the mobility of the vacancy is lowered, so that with a very high quenching rate no nuclei will be formed, and consequently, no loops will be observed. On the other hand, when the quenching rate is extremely slow all the vacancies will have time to go to the permanent sinks so that once again no dislocation loops will be observed. In the intermediate case dislocation loops will of course be observed, but one would expect the number of loops observed to decrease if either the binding energy or the quenching rate was increased.

In quenched alloys the concentration of vacancies, C_v'. never exceeded 2×10^{-4} and it follows from table 3 that E_b is small and less than about $0 \cdot 1$ ev. A binding energy of this order of magnitude would be expected from elasticity calculations using the misfit values of solute and solvent atoms. It is also consistent with the observation of Panseri and Federighi (private communication) who obtained from resistivity measurements a value of $0 \cdot 70 \pm 0 \cdot 02$ ev for E_f in aluminium–zinc alloys compared with $0 \cdot 76$ ev for pure aluminium.

From the experimental observations it is impossible to determine which solute atoms are most strongly bound to vacancies. It is expected that when the binding energy is large the diffusion rate of vacancies to sinks will be reduced and hence the size of the loops (i.e. the number of vacancies which collect at a given nucleus for a given quenching treatment) will give a measure of the binding energy. Thus from the results, the binding energy between a solute atom and vacancy is expected to increase in the order, zinc, copper, silver, magnesium, silicon. However, the fineness in scale could merely indicate the increasing ease with which loops are nucleated in these systems. Thus in aluminium–silicon alloys the concentration of loops is about 3×10^{10} cm^{-2} when quenched-in silicon oil, compared with $1 \cdot 2 \times 10^9$ in pure aluminium given the same treatment.

The results in table 2 for the aluminium–silicon alloy illustrate the importance of diffusion length in determining the size of the loops. As the temperature of the water is raised the diffusion time and hence the size of the loops increases. At distances greater than the collection region around each loop the vacancies will remain in solid solution. The importance of nucleation is evident from the absence of loops when this alloy is quenched into water at $20\,°$c and all the vacancies remain in solution. However, when such a material is annealed at temperatures at which rapid diffusion is expected many defects are observed. The early stages of solute precipitation are also expected at these temperatures. In the presence of a high density of vacancies in solid solution the solute atoms will move rapidly in

association with the vacancies and the triangular defects are probably formed by the collapse of a vacancy platelet in the presence of a high local concentration of solute atoms. The stacking-fault energy and dislocation line energy in this region are likely to be very different from that of pure aluminium and may account for the triangular shape containing a stacking fault. The absence of defects even after ageing of the high magnesium alloy is perhaps because the vacancies are trapped by impurities during the quench and upon subsequent heating there is insufficient supersaturation of vacancies to nucleate loops, and due to the lack of nuclei the vacancies drain off the existing sinks.

Thus the number of loops seen in quenched metals depends upon the ability to form nuclei during the quench, and the number of vacancies in each loop upon the effective diffusion distance of the vacancies during the quench, both these terms will, of course, depend on E_b. Only if the diffusion distance is considerably greater than the distance between nuclei will all the vacancies precipitate.

REFERENCES

BLEWITT, T. H., COLTMAN, R. R., KLABUNDE, C. E., and NOGGLE, T. S., 1957, *J. appl. Phys.*, **28,** 639.

DESORBO, W., TREAFTIS, H. N., and TURNBULL, D., 1958, *Acta Met.*, **6,** 501.

FEDERIGHI, T., 1958, *Acta Met.*, **6,** 379.

HIRSCH, P. B., SILCOX, J., SMALLMAN, R. E., and WESTMACOTT, K. H., 1958, *Phil. Mag.*, **3,** 897.

JOHNSON, R. P., 1939, *Phys. Rev.*, **56,** 814.

LOMER, M., 1957, Vacancies and Point Defects in Metals and Alloys, J.I.M. Symposium.

LOMER, M., and COTTRELL, A. H., 1955, *Phil. Mag.*, **46,** 711.

MARTIN, D. G., 1960, European Atomic Energy Society Symposium on Principles of Radiation Damage in Crystals, Saclay.

SEITZ, F., 1952, *Advanc. Phys.*, **1,** 43.

SMALLMAN, R. E., WESTMACOTT, K. H., and COILEY, J. A., 1959, *J. Inst. Met.*, **88,** 127.

SMALLMAN, R. E., 1960, *The Metallurgist*, **1,** 146.

THOMAS, G., and WHELAN, M., 1959, *Phil. Mag.*, **4,** 511.

WESTMACOTT, K. H., HULL, D., BARNES, R. S., and SMALLMAN, R. E., 1959, *Phil. Mag.*, **4,** 1089.

CORRESPONDENCE

The Interfacial Energy of Coherent Twin Boundaries in Copper

By M. C. INMAN and A. R. KHAN

National Physical Laboratory, Teddington, Middlesex

IN 1951, Fullman determined the interfacial energy of coherent twin boundaries in copper annealed at 950°C, by optical examination of the equilibrium dihedral angles developed at the intersection of surface traces of twin and grain boundary planes. The value 0·045 was obtained for the ratio γ_t/γ_G of the twin and grain boundary energies. From similar observations of thermally etched twin and grain boundary groove angles at a copper–lead vapour interface, the result 0·026 was deduced for γ_t/γ_G. Using the mean value 0·035 for the ratio γ_t/γ_G, and assuming γ_G to be approximately 600 erg cm^{-2} in copper (Fisher and Dunn 1952), γ_t is about 21 erg cm^{-2}. In recent years, a knowledge of the energy γ_t of coherent twin boundaries has assumed importance as a guide to the stacking fault energy and dislocation width, and Fullman's result has been the basis of various estimates of these quantities in copper (Seeger and Schoeck 1953) and other metals (Hirsch and Thornton 1958). A more precise technique to measure γ_t/γ_G would therefore be very useful, and it is the purpose of this letter to report the improvement in precision which electron transmission microscopy can give, compared to the optical method used by Fullman.

We have examined thin films of copper with a Siemen's Elmiskop I electron microscope. Clear pictures of coherent twin boundary–grain boundary intersections were obtained which show the change in direction of the grain boundary at the line of intersection, due to the small force exerted by the twin. In many cases the surface plane of both the grain and the twinned material can be established by selected area diffraction, so that the (111) twin plane is determined. The angle of inclination of this plane to the surface of the specimen is then precisely known. In addition, the inclinations of the grain boundary planes can also be deduced by comparing their projected widths with that of the coherent twin plane. We assume the specimen thickness is constant over the small area of intersection. With the above information it is possible to compute the true dihedral angles between the twin and grain boundary planes from measurements of apparent angles between their surface traces, by making corrections for the angles of inclination at the intersection. We have now measured the true dihedral angles of intersection in a number of transmission specimens prepared from

OFHC copper foil annealed for 4 hours at 950°C. The ratio γ_t/γ_G was then determined by Fullman's method where forces arising from the interfacial energies are resolved in a direction parallel to the coherent twin plane. Our measurements of γ_t/γ_G lie in the range $+0.008$ to $+0.045$ with very strong clustering about the mean $+0.02$.

Fullman's corresponding measurements of the ratio γ_t/γ_G with the optical microscope, have a range -0.04 to $+0.24$ with clustering around a mean value $+0.045$. It appears that the detailed information inherent in the three-dimensional pictures obtained by electron transmission microscopy increases the precision of measurement of γ_t/γ_G by roughly a factor ten. A more reliable estimate can therefore be obtained of the relative magnitudes of stacking-fault energies and dislocation widths in the face-centred cubic metals. At the present time, our measurements indicate that the stacking-fault energy in copper is little more than half the value 40 ergs cm^{-2} usually assumed from Fullman's work.

Finally, the enhanced precision of our method leads to the possibility that small changes in the ratio γ_t/γ_G resulting from impurity additions, can be reliably detected and measured. In this way we hope to obtain new information about impurity segregation at interfaces and the consequent changes in interfacial energies.

REFERENCES

FISHER, J. C., and DUNN, C. G., 1952, *Imperfections in Nearly Perfect Crystals* (New York: John Wiley & Sons), p. 317.
FULLMAN, R. L., 1951, *J. appl. Phys.*, **22**, 448.
SEEGER, A., and SCHOECK, G., 1953, *Acta Met.*, **1**, 519.
THORNTON, P. R., and HIRSCH, P. B., 1958, *Phil. Mag.*, **3**, 748.

Refractive Index of Solid Krypton and Solid Argon

By B. L. Smith

Department of Physics, Queen Mary College (University of London), London, E.1

Jones and Smith (1960) determined the refractive index (n) of solid argon over the temperature range 74°K to 84°K. The results indicated a probable increase of the Lorentz–Lorenz function $(n^2-1)/(n^2+2)\rho$ with increasing density (ρ) but this result depended upon a revised assessment of the available measurements of density near the triple point. In this note corresponding measurements of the refractive index of solid krypton are reported, together with some new determinations of the density of solid argon near the triple point which confirm the conclusion of the earlier paper.

The refractive index of solid krypton was determined over the temperature range 71°K to 109°K using the simple oxygen cryostat and spectrometer described by Jones and Smith. The specimen was condensed into a hollow Perspex prism and the refractive index determined by the method of minimum deviation. The krypton was stated by the British Oxygen Company Ltd., to contain up to 0·5% xenon and of the order of 0·001% of other impurities. Results of measurements made at a wavelength of 5893 Å are shown in fig. 1, and in fig. 2 the Lorentz–Lorenz function is plotted against density. Values of the density were taken from the data of Figgins and Smith (1960).

The density of solid argon was re-determined over the temperature range 77°K to 83°K by the bulk-density method used by Dobbs *et al.* (1956) and by Figgins and Smith. The argon was stated to be of at least 99·999% purity and the results are shown in fig. 3. It is seen that they are in fair agreement with those of previous investigators, including the value of the density at the melting point deduced by Clusius and Weigand (1940) from observations of the melting curve and of the density of the liquid, and their value as revised by Jones and Smith. In fig. 4 the Lorentz–Lorenz function for solid argon is plotted versus density for the refractive index data of Jones and Smith and values of the density taken from the curve of fig. 3.

Assuming that the specific influence of temperature is small, it appears from figs. 2 and 4 that the Lorentz–Lorenz function increases with increasing density for both solids. This is not in agreement with the theory based on the Lorentz local field model, which predicts that for a non-polar solid with cubic symmetry the Lorentz–Lorenz function should

Fig. 1
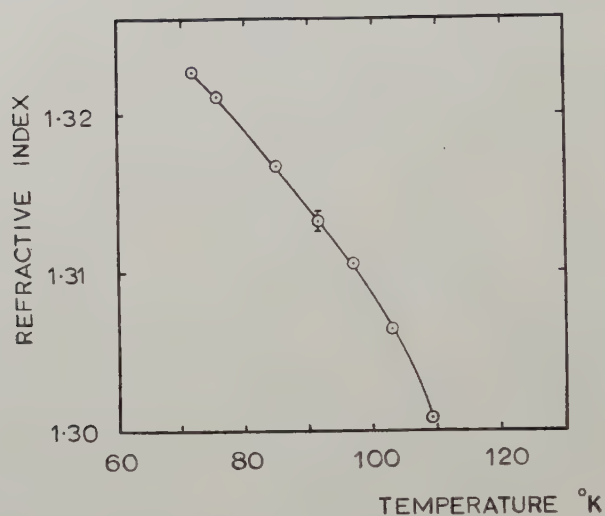
Refractive index of solid krypton.

Fig. 2
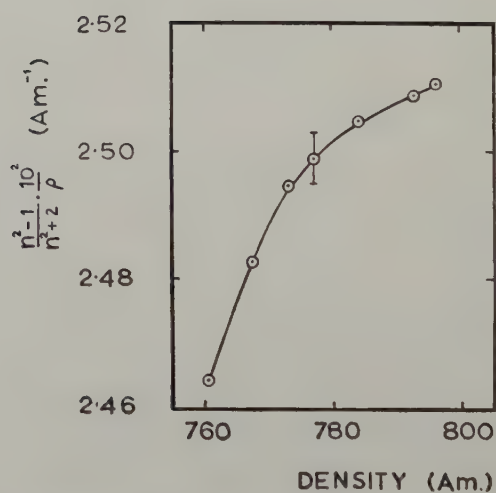
Lorentz–Lorenz function $(n^2-1)/(n^2+2)\rho$ of solid krypton versus density.

Fig. 3

Density of solid argon.

Fig. 4

Lorentz–Lorenz function of solid argon versus density.
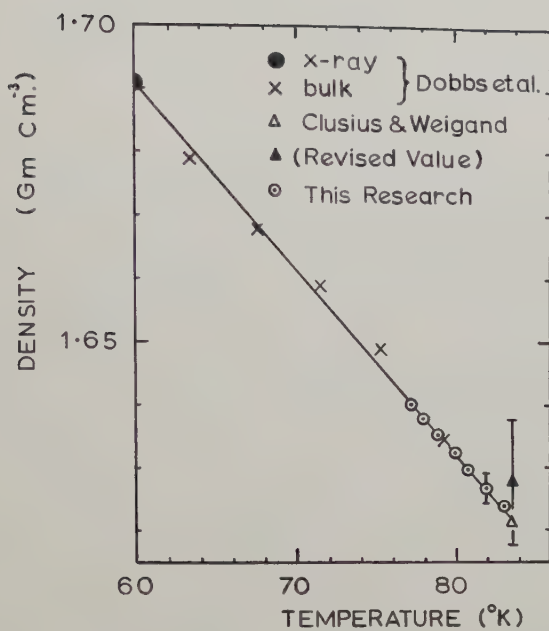
be independent of density. Measurements of the refractive index are now being extended to a lower temperature range (where more accurate data for the density are available) so that the range of densities employed can be extended.

REFERENCES

CLUSIUS, K., and WEIGAND, K., 1940, *Z. phys. Chem.* B, **46,** 1.
DOBBS, E. R., FIGGINS, B. F., JONES, G. O., PIERCEY, D. C., and RILEY, D. P., 1956, *Nature, Lond.*, **178,** 483.
FIGGINS, B. F., and SMITH, B. L., 1960, *Phil. Mag.*, **5,** 186.
JONES, G. O., and SMITH, B. L., 1960, *Phil. Mag.*, **5,** 355.

The Solubility of Krypton in Liquid Cadmium and Indium

By G. W. Johnson

Metallurgy Department, University of Leeds

In a previous paper (Johnson and Shuttleworth 1959) experimental measurements of the solubility of krypton in the tetravalent liquid metals lead and tin were found to agree quite well with values estimated from the surface energies of the liquid metals. This work has now been extended to divalent cadmium and trivalent indium, and the estimated solubilities are in reasonable agreement with the experimental results.

Since the last paper was published Hewitt et al. (1960) have reported attempts to measure the solubility of xenon in liquid bismuth by mass spectrographic and radioactive techniques. They found that at 500°c and a xenon pressure of 1 atmosphere the atomic fraction of xenon dissolved in liquid bismuth was less than 2×10^{-10} ($r < 6 \times 10^{-7}$), and this would be expected as the solubility estimated from the surface energy of liquid bismuth is $r \sim 10^{-12}$.

Measurements on liquid indium were made over a temperature range of 1000°c to 1300°c, but because of its low boiling point the measurements on liquid cadmium could not be made above 1150°c because the silica tube exploded.

Results are shown in the figure and the solubility increases with temperature according to the equation

$$r = r_\infty / \text{antilog} \, (T_s/T)$$

where r is the Ostwald coefficient defined by

$$r = \frac{\text{Number of gas atoms in unit volume of liquid metal}}{\text{Number of gas atoms in unit volume of gas}}$$

$$= \text{Volume of gas dissolved in unit volume of metal.}$$

Values of r_∞, T_s, and the heat of solution $2 \cdot 3RT_s$ (energy required to transfer a krypton atom from the gas into solution in the metal), are given in table 1 together with more accurate values for the elements reported previously.

Table 1

Metal	r_∞	T_s (°K)	$2 \cdot 3RT_s$ (kcal/mole)
Cadmium	1·5	11000	50·3
Indium	1·5	10125	46·3
Lead	0·13	7110	32·5
Tin	0·73	9550	43·7

The thermodynamic equation giving the solubility in terms of the energy H needed to transfer an atom at rest in the gas into solution in the metal, and the vibrational entropy S of a krypton atom dissolved in the liquid metal is

$$r = X \exp\left(S/R\right) \exp\left(-H/RT\right)$$

$$X = \frac{h^3}{(2\pi mkT)^{3/2}} \frac{1}{a^3} = 4 \cdot 053 \frac{\rho}{MT^{3/2}}$$

where m is the mass of a krypton atom, $1/a^3$ the number of metal atoms in unit volume of liquid metal, ρ the density of the liquid metal at the temperature of the experiment, and M its molecular weight.
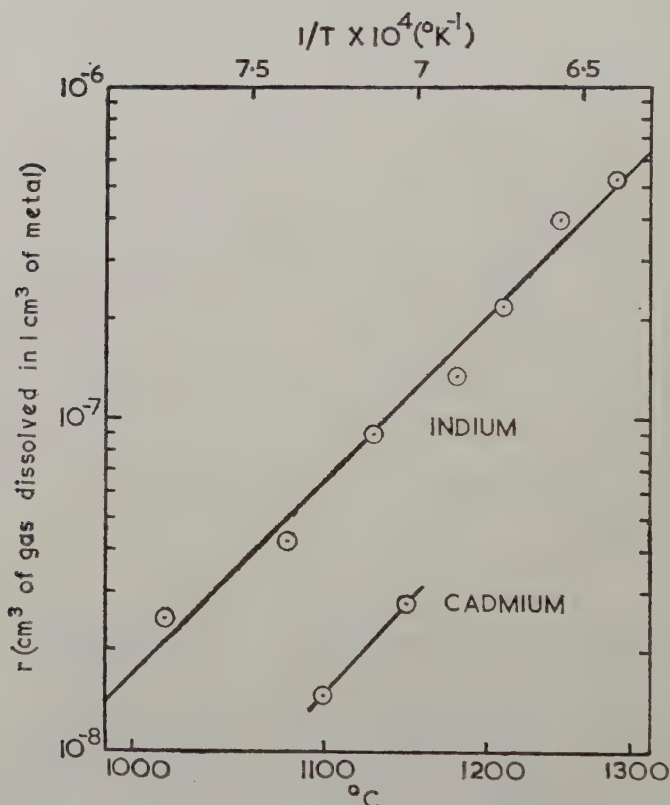
The variation with temperature of the Ostwald solubility coefficient r.

Values of H and S for liquid cadmium and indium are given in table 2 together with the recalculated values for liquid lead and tin. The cadmium results are very approximate but they are included for comparison with the other results.

Previous work on lead, tin and silver suggested that a theoretical estimate of the heat of solution of krypton in a liquid metal could be made by considering that the energy H is made up of three terms: the energy H_h to make a hole in the liquid of the size of a krypton atom, the vibrational energy of a krypton atom in the liquid and the negative van der Waals interaction energy between the krypton atom and the surrounding metal atoms.

The energy to make a hole in the liquid was estimated by multiplying the surface area of a sphere of the same radius as a krypton atom ($1.98 Å$) by the surface energy per unit area of the liquid metal extrapolated to $0°K$, and the vibrational energy of a krypton atom was approximated to H_{vib} the enthalpy of a metal atom. Adsorption data (Rosenberg 1958, Haul and Swart 1957) suggested that the van der Waals interaction energy should be about 5 kcal/mole.

Table 2

Metal	H (kcal/mole)	S (cal/°K/mole)	S_m (cal/°K/mole)	H_{vib} (kcal/mole)	H_h (kcal/mole)	γ_0 (ergs/cm^2)
Cadmium	55	29	25·5	7·1	48·2	680
Indium	51·2	29·0	27·5	11·2	42·7	602
Lead	36·7	23·8	28·1	10·2	44·2	624
Tin	48·0	27·2	27·2	11·7	42·5	599

The surface energies γ_0 extrapolated to $0°K$ of cadmium (Oriani 1950) and indium (Melford and Hoar 1956–57) are given in table 2 together with the values of H_h calculated from them. Considerable variations exist in the experimental values of the surface energies of lead and tin and the latest measurements (Melford and Hoar 1956–57) are given in table 2.

The estimated values of H are within a few kilocalories of the experimental values for the liquid cadmium, indium and tin systems, but the surface energy quoted for lead is 28% greater than that given in the previous paper and the estimated value of H is now 12 kcal/mole too large.

In table 2 the vibrational entropy S of a krypton atom dissolved in the liquid metal is compared with the vibrational entropy S_m of the metal atoms derived from specific heat data (*International Critical Tables* 1926, Kubaschewski and Ll. Evans 1958). The differences between the gas and metal entropies are small and not much greater than the probable errors in the experimental values.

REFERENCES

HAUL, R. A. W., and SWART, E. R., 1957, *Z. Elektrochem.*, **61,** 380.
HEWITT, F. G., LACEY, J. A., and LYALL, E., 1960, *Reactor Technology*, **1,** 167.
International Critical Tables, 1926, Ed. E. W. Washburn, 5 (New York; McGraw-Hill), p. 88.
JOHNSON, G. W., and SHUTTLEWORTH, R., 1959, *Phil. Mag.*, **4,** 957.
KUBASCHEWSKI, O., and LL. EVANS, E., 1958, *Metallurgical Thermochemistry*, 3rd edn (Pergamon Press).
MELFORD, D. A., and HOAR, T. P., 1956–57, *J. Inst. Met.*, **85,** 197.
ORIANI, R. A., 1950, *J. chem. Phys.*, **18,** 575.
ROSENBERG, A. J., 1958, *J. phys. Chem.*, **62,** 1112.

The Refractivity and Light Scattering of Crystals Containing Defects

By E. W. J. Mitchell and J. E. Whitehouse
J. J. Thomson Physical Laboratory, The University, Reading

Several authors (see Dexter 1958) have discussed the refractivity of crystals containing defects, but little attention has been given to the scattering of light by defects. Refractivity depends linearly on the polarizability of the defects, whereas the amount of light scattered out of the crystal depends on the square of their polarizabilities. In this note we should like to point out that under certain circumstances this distinction may be used to estimate the concentration of defects in a crystal.

The refractivity of an assembly of $N(\text{cm}^{-3})$ identical particles each of polarizability α_0 is

$$R_f = \frac{3}{4\pi} \frac{n^2 - 1}{n^2 + 2} = N\alpha_0. \qquad \cdots \cdots \quad (1)$$

As long as α_0 and N are not changed it does not matter whether the particles are random or ordered. However, the amount of light scattered by the assembly is very dependent on the order, being zero in the case of the perfect crystal. If the crystal contained $N_d(\text{cm}^{-3})$ vacant sites and $N_d(\text{cm}^{-3})$ interstitial atoms also of polarizability α_0, and if it were otherwise perfect the amount of light scattered at right angles from the crystal (the Rayleigh ratio) would be

$$R_{90}' = 2N_d(\tfrac{1}{2}k^4)\alpha_0^2 \qquad \cdots \cdots \cdots \cdots \quad (2)$$

where k is the wavelength constant $(2\pi/\lambda)$ in the medium ($k^4 = 24 \cdot 5 \times 10^{20}$ for quartz at 4400 Å) and R_{90}' is the scattered flux, per unit solid angle, per unit volume of medium, per unit incident intensity. In these ideal circumstances we could determine N_d from measurements of R_f and R_{90}'.

In a more realistic case we can attempt to allow for the relaxation of atomic positions surrounding the point defects and for the associated spread of the wave functions of the outer electrons of the interstitial atoms. Let the polarizability associated with these effects be represented by $\Delta\alpha_i$ for the interstitial atom and $\Delta\alpha_v$ for the vacancy. We also suppose that the volume of the crystal containing defects is such that there are N' atoms per cm³. We then have

$$R_{90}' = \tfrac{1}{2}k^4 N_d[(-\alpha_0 + \Delta\alpha_v)^2 + (\alpha_0 + \Delta\alpha_i)^2], \quad \cdots \cdots \quad (3a)$$

$$R_f' = (N' - N_d)\alpha_0 + N_d\Delta\alpha_v + N_d(\alpha_0 + \Delta\alpha_i)$$

$$= N'\alpha_0 + N_d(\Delta\alpha_v + \Delta\alpha_i). \qquad \cdots \cdots \cdots \cdots \quad (3b)$$

The density change is given by $\quad \dfrac{\Delta\rho}{\rho_0} = \dfrac{N - N'}{N}$,

and using (3 a) and (3 b) we have

$$\frac{\Delta R_f}{R_f} = -\frac{R_f - R_f'}{R_f} = \frac{\Delta\rho}{\rho_0} - f_d \frac{(\Delta\alpha_v + \Delta\alpha_i)}{\alpha_0} \qquad . \quad . \quad . \quad (4)$$

where f_d is the fraction of defects N_d/N.

The above discussion was prompted by some measurements which we have made on neutron-irradiated quartz. The specimen has been irradiated in a hollow uranium slug with an estimated dose of $6 \cdot 4 \times 10^{18}\,\mathrm{n}^\circ\,\mathrm{cm}^{-2}$ of energy over 1 Mev. In order to achieve the state in which the polarizabilities associated with the point defects were close to α_0 the crystal was optically and thermally bleached. The latter was carried out by heating at $540^\circ\mathrm{c}$ and as a result of these treatments all the electrons should be in the lowest energy levels in the irradiated crystal. In support of the assumption that this condition had been reached we found that absorption bands due to trapped electrons and holes, and associated luminescence peaks, had been removed. Several authors have found that annealing of atomic damage is not significant at $500^\circ\mathrm{c}$—e.g. Wittels (1953), Mitchell and Paige (1956).

In this condition $\Delta R_f/R_f$, $\Delta\rho/\rho_0$ and R_{90}' were measured. $\Delta R_f/R_f$ was measured for both the ordinary and extraordinary rays and found to be $-(0 \cdot 12 \pm 0 \cdot 03)\%$. By comparing with an unirradiated block from the same crystal $\Delta\rho/\rho_0$ was found by weighing in air and water to be $-(0 \cdot 13 \pm 0 \cdot 05)\%$. We therefore conclude that $f_d(\Delta\alpha_v + \Delta\alpha_i)/\alpha_0$ is small. Since there is a density change f_d cannot itself be very small so that we conclude that $|\Delta\alpha_v + \Delta\alpha_i| \ll \alpha_0$. This of course may mean either that both $\Delta\alpha_v$ and $\Delta\alpha_i$ are of the same sign and small, or that they are large but of opposite sign.

The scattered light from the crystal shows a λ^{-4} variation. It is of interest to see what fraction of point defects would be required to account for the observed change in R_{90}'. Assuming the first alternative given above ($\Delta\alpha_i$ and $\Delta\alpha_v$ both small) and taking $\overline{\alpha_0} = \frac{1}{3}(\alpha_{Si} + 2\alpha_{0x})$, f_d can be calculated from (1) and (2). After correcting for a small amount of light scattering from the unirradiated crystal the values of R_{90}' were $4 \cdot 8 \times 10^{-6}$ for **E** parallel, and $2 \cdot 4 \times 10^{-6}$ for **E** perpendicular to the c-axis of the crystal. Although this indicates an anisotropic polarizability we can determine an approximate value of f_d using the isotropic $\overline{\alpha_0}$. By this means we find $f_d = 2 \cdot 5$ or $1 \cdot 3\%$. Previous measurements using long wavelength neutron scattering indicated that f_d was at least $0 \cdot 8\%$.

We conclude therefore that the assumption of point defects together with the use of the method described gives a plausible account of the quartz results. However, it must be pointed out that one cannot distinguish by these experiments alone between point defects and various combinations of point defects and disordered regions of less than about $1000\,\text{Å}$.

The quartz work referred to here has been used to illustrate the applicability of the method, and a detailed account of the optical work will be

published later. It would be of interest to compare refractivity, density and light scattering on a crystal containing some well understood defect, such as vacancies in the alkali halides.

REFERENCES

DEXTER, D. L., 1958, *Phys. Rev.*, **111,** 119.
MITCHELL, E. W. J., and PAIGE, E. G. S., 1956, *Phil. Mag.*, **1,** 1085.
WITTELS, M., 1953, *Phys. Rev.*, **89,** 656.

REVIEWS OF BOOKS

Theoretical Physics in the Twentieth Century : A Memorial Volume to Wolfgang Pauli. (Interscience Publishers, 1960.) [Pp. 328.] $10.00.

THIS memorial volume to Pauli is partly a summary of progress in subjects closest to Pauli's interests and partly an account of the heroic age of modern physics in which Pauli played so important a part. The distinguished contributors include Niels Bohr who writes of Pauli's arrival in Copenhagen at the age of twenty-two when he was already well known for his authoritative review article on relativity written two years before and of his increasing authority until he became the very conscience of the community of theoretical physicists. Kronig writes on the turning point of modern physics in the mid-1920's, with particular reference to the development of Pauli's proposals that an electron has two intrinsic states and that it satisfies an exclusion principle. Both Kronig and Van der Waerden discuss the proposal for a spinning electron first made by Kronig, after hearing Pauli's suggestion of a two-state electron, but not published because of strong theoretical and experimental objections valid at that time. It is interesting to learn that Uhlenbeck and Goudsmit, after making independently their proposal of a spinning electron, almost withdrew it from publication for similar reasons. Pauli was the last of the great theorists at that time to accept the concept of the spinning electron and gave his approval only after Thomas had established consistency with experiment. In contrast to this reluctance Pauli's great concern for consistency with known laws of conservation lead him to the striking prediction of a new (mass-less) particle, the neutrino, in 1931, to explain certain phenomena in beta decay. One wonders whether he would have proposed the neutrino so readily had it then been known that parity was not conserved in beta decay and the neutrino appears to have a fundamental asymmetry. The recent developments in our understanding of beta decay are surveyed in an excellent article by Miss Wu. Other notable contributors include Wentzel on Field Theory, Bargman on Relativity, and Peierls on Quantum Theory of Solids. This is an excellent volume that can be enjoyed by any educated physicist.   R. J. E.

Quantum Theory : Methods and applications. By R. DAUDEL, R. LEFEBVRE and C. MOSER. (New York ; Interscience Publishers, 1959.) [Pp. 572.] $14.50.

THE subject matter of this book is a good deal narrower than its title suggests. In fact it is concerned very largely with the theory of the electronic structure of small molecules such as oxygen and methane and with the properties of conjugated hydrocarbons and their derivatives.

The authors' arrangement of material is somewhat unusual : the first half of the book is largely qualitative in character, while the second half covers much the same ground but in a more quantitative way. Such a treatment is most helpful in a subject where mathematical detail is liable to obscure scientific motivation. I wondered, however, whether the publication of the first section independently would not be financially helpful to a large number of potential readers.

Very few books giving a detailed description of this important branch of theoretical chemistry are available. The present one is probably the most useful to those seeking a reasonably advanced introduction to the subject.
                L. E. O.

Axiomatics of Classical Statistical Mechanics. By RUDOLF KURTH. (Pergamon Press, 1960.) [Pp. x + 180.] £2 5s. 0d.

THIS volume appears as Volume II in the International Series of Monographs on Pure and Applied Mathematics, and is no doubt one of the volumes devoted to pure mathematics. In it the author, who has for some time made a study of the basic concepts employed in statistical mechanics and in the difficulties one can encounter when trying to apply statistical mechanics to such systems as star clusters, constructs classical statistical mechanics as a deductive system : this is certainly in accord with Gibbs' point of view who tried to construct it as part of rational mechanics since " one is building on an insecure foundation, who rests his work on hypotheses concerning the constitution of matter ". In the main the author has admirably succeeded in his formidable task, and his monograph will be of great interest to the many people who are interested in the foundations of statistical mechanics. The present reviewer feels, however, that apart from these people, the present volume will not appeal to physicists, although it should be of interest to mathematicians working in the fields of probability theory and set theory.   D. t. H.

Theory of Detonation. By IA. B. ZELDOVICH and A. S. KOMPANEETS. (New York and London: Academic Press, 1960.) [Pp. 284.]   Price $10.00.

A serious problem which has faced those interested in acquiring a basic knowledge of shock waves and detonations has been the absence of suitable texts in English. In consequence, such knowledge has tended to be restricted to a very narrow range of persons directly concerned with the field, which is also to some extent security-ridden. *Theory of Detonations* by Zeldovich and Kompaneets goes a long way towards supplying the needs of a wider circle.

A detonation is a shock wave supported by chemical reactions, and any theoretical treatment of it must be preceded by some discussion of shock waves without attendant chemical reaction. This is treated simply and elegantly in the first chapter. Distinction is drawn between weak (i.e. nearly isentropic) and strong shocks, and plane one-dimensional and centrally symmetric propagation are discussed.

The next section deals with the hydrodynamic theory of detonation and leads to a substantiation of the Chapman–Jouguet hypothesis. Here also the combination of simple mathematics with clear diagrams leads to a satisfactory treatment. The rest of the book is given over to discussion of those aspects of detonation which have interested the workers at the Chemical Physics Institute of the Academy of Sciences of the USSR—i.e. losses in detonation in pipes, spinning detonations, the effects of roughened walls, and the detonation of condensed explosives. In the last case there is an interesting semi-quantitative discussion.

Modern references are almost exclusively to Russian work, to which the book will prove a useful key. The translation is excellent, and the translator, regrettably, anonymous.   T. M. S.

Fig. 2

Superlattice dislocations in fully ordered alloy, i.e. $S=1$. Normal to micrograph is [100].

Fig. 3

.5 μ

Superlattice dislocations in partially ordered alloy in which $S = 0.68$.

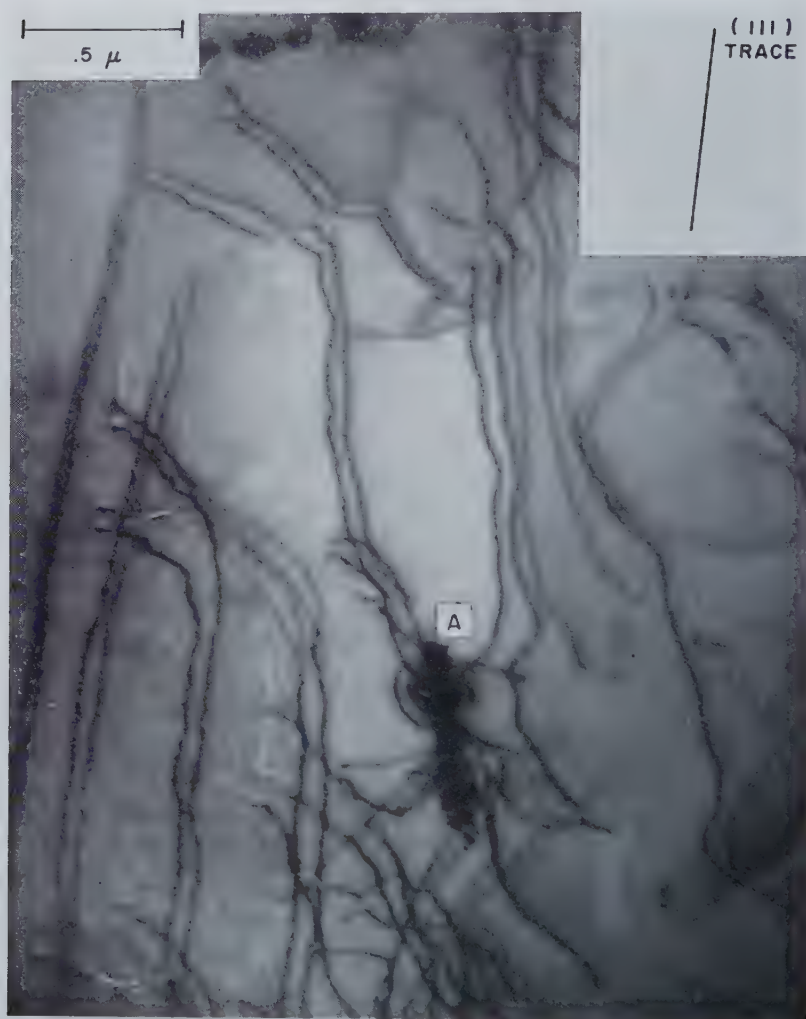Fig. 4

Superlattice dislocations in partially ordered alloy in which $S = 0.45$.   Normal to micrograph is [112].
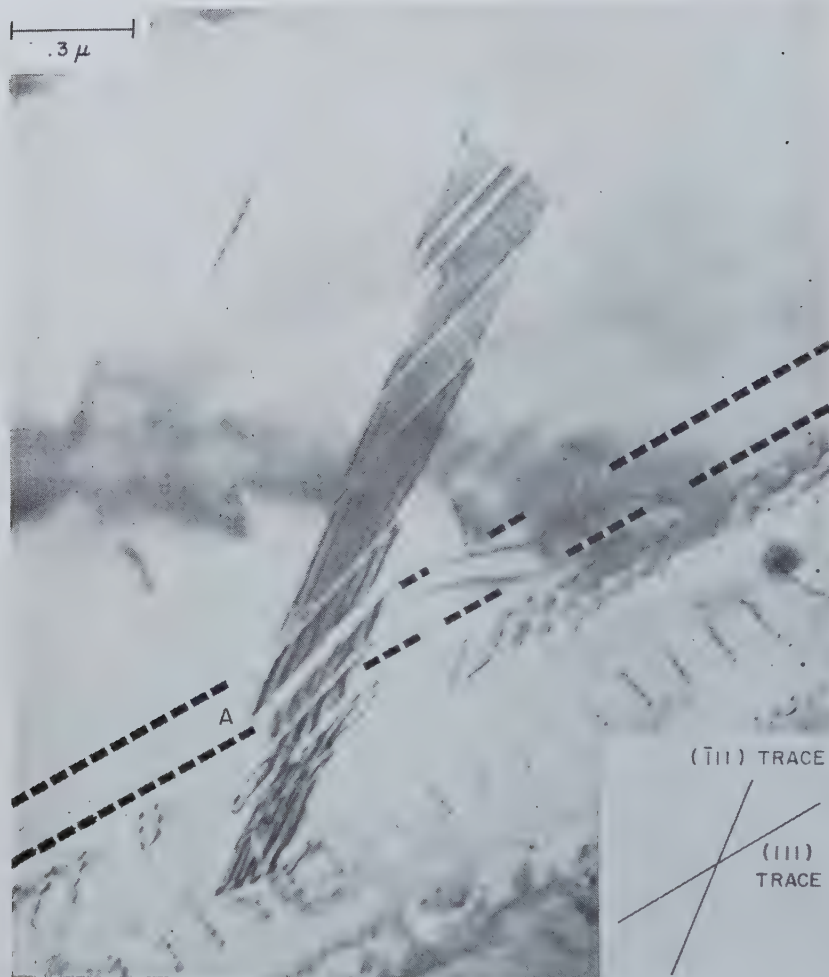
Fig. 5

Superlattice dislocations in partially ordered alloy in which $S = 0.45$. Normal to micrograph is $[11\bar{2}]$.
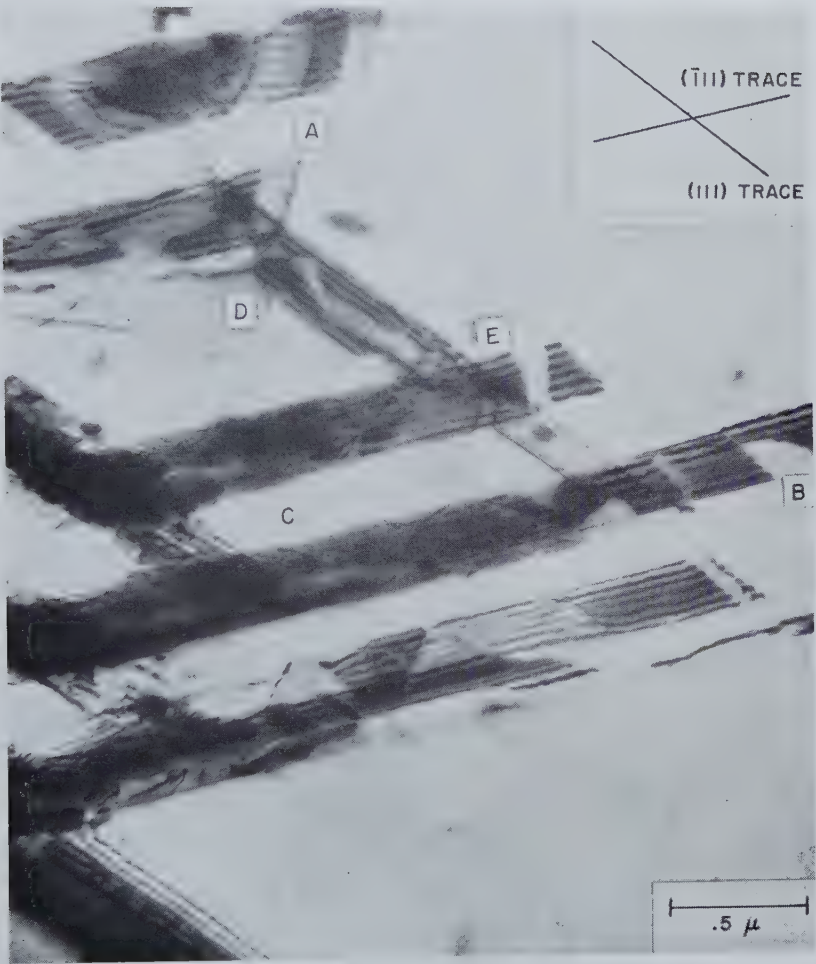
Fig. 6

Micrograph showing the relatively high resistance to electrochemical attack of stacking faults in the disordered alloy compared to the matrix.

Fig. 7

Intersection of dislocations with stacking fault in disordered alloy.   Normal to micrograph is [032].

Fig. 9

Stacking-fault configurations in the disordered alloy.   Normal to micrograph is [021].

Fig. 10

Generation of dislocations at stacking-fault interfaces.   Normal to micrograph is [032].

Fig. 13

Configuration of ordinary dislocations in the disordered Ni₃Mn alloy.   Normal
to micrograph is [112].

A. J. FORTY

Phil. Mag. Ser. 8, Vol. 6, Pl. 103.
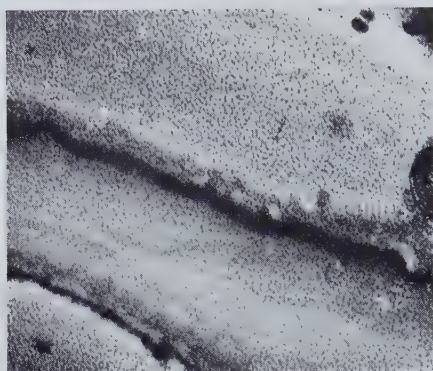
Fig. 1

Fig. 2

Black speckle developed in crystal during slow decomposition. × 10 000.
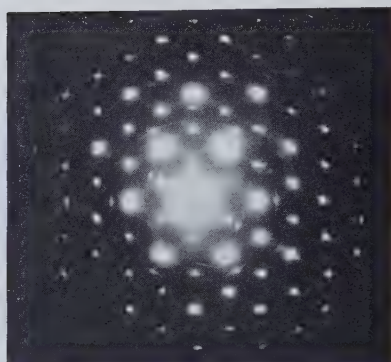
Diffraction pattern for area of crystal shown in fig. 1. Note the occurrence of extra spots and rings which may be related to the presence of precipitates of lead (ref. fig. 9).

Fig. 3
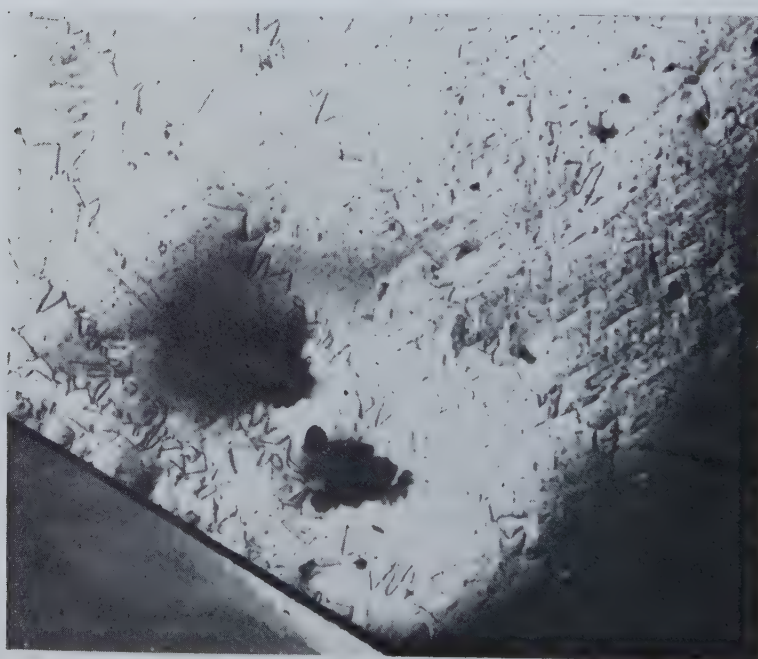
Black speckle developed in a crystal containing helical dislocations. Note the preferential growth of precipitates along the zig-zag segments of these. × 14 000.

Fig. 4
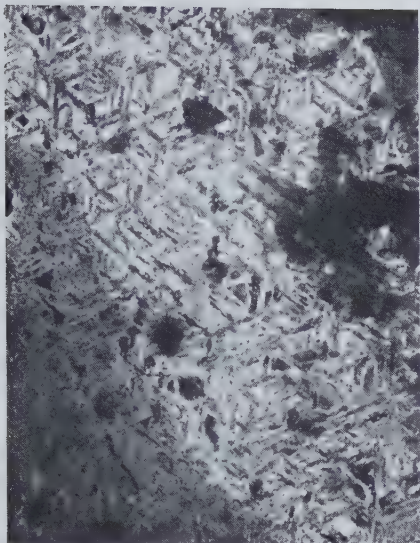
The development of cross-hatched pattern of precipitates after prolonged periods of slow decomposition.   × 14 000.

Fig. 5
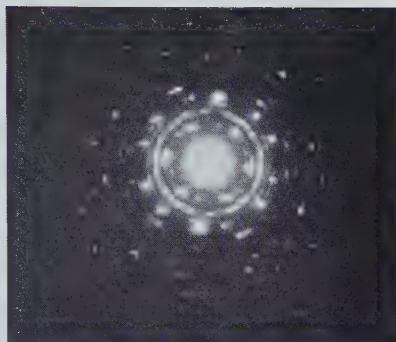
Diffraction pattern for the area of crystal shown in fig. 4.

Fig. 6
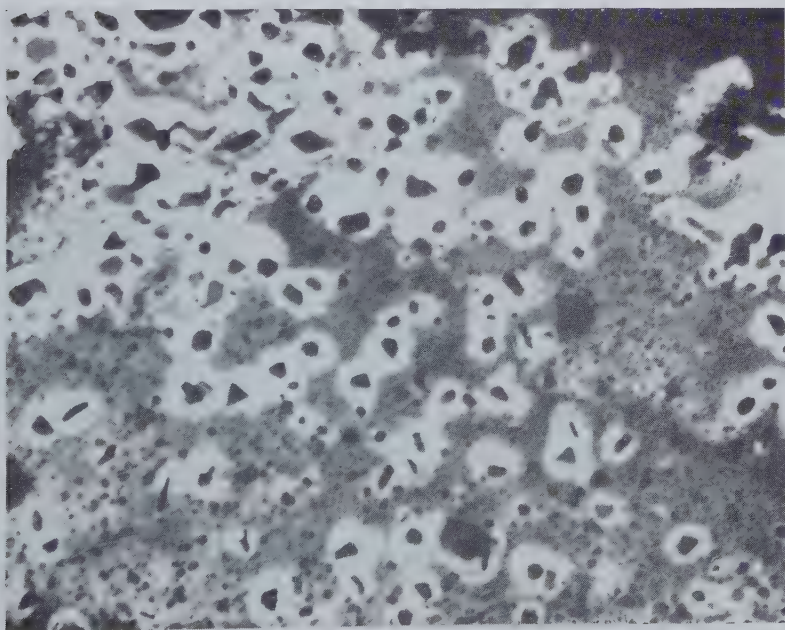
Crystallites produced in the centre of decomposition under irradiation at high beam intensities.   × 10 000.

A. J. FORTY

Phil. Mag. Ser. 8, Vol. 6, Pl. 105.
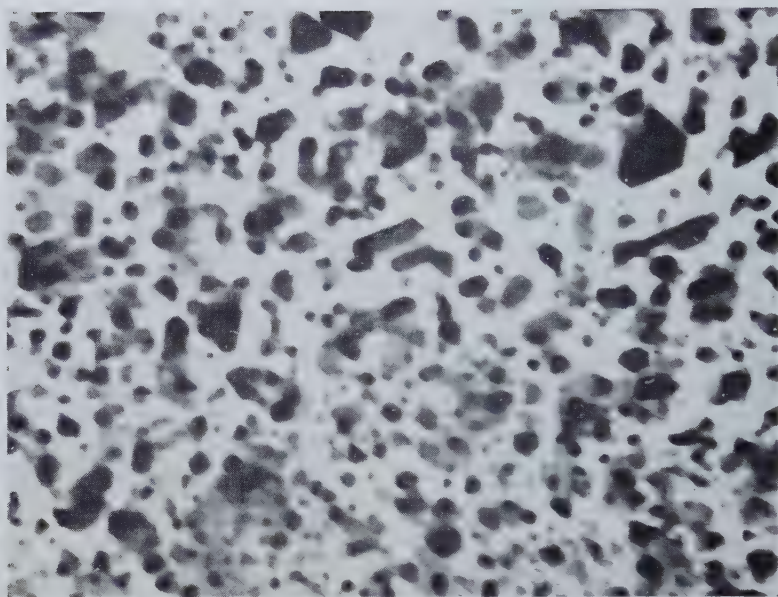
Fig. 7

Platelets produced by irradiation at high beam intensities.   These are similarly
oriented in the lead iodide crystal. × 20 000.

Fig. 8

Diffraction pattern for the area of crystal shown in fig. 7.   Note the extra
spots which may be identified with the presence of f.c.c. lead and also the
occurrence of the star by streaking between the {10$\bar{1}$0} spots and {11$\bar{2}$0}
spots.

Fig. 10

Illustrating the precipitation of a new phase inside cavities in the intermediate
zone of decomposition.   × 7000.

Fig. 11

(a)   (b)
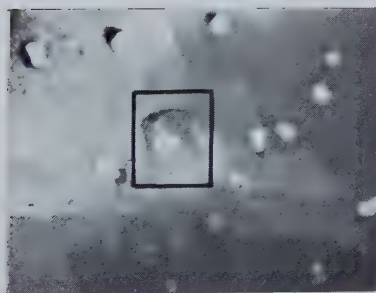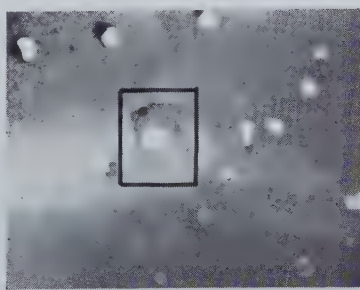
Illustrating the breakaway of a cavity from a precipitate.   (a) Cavity attached.
(b) Cavity detached.   × 14 000.

Fig. 12
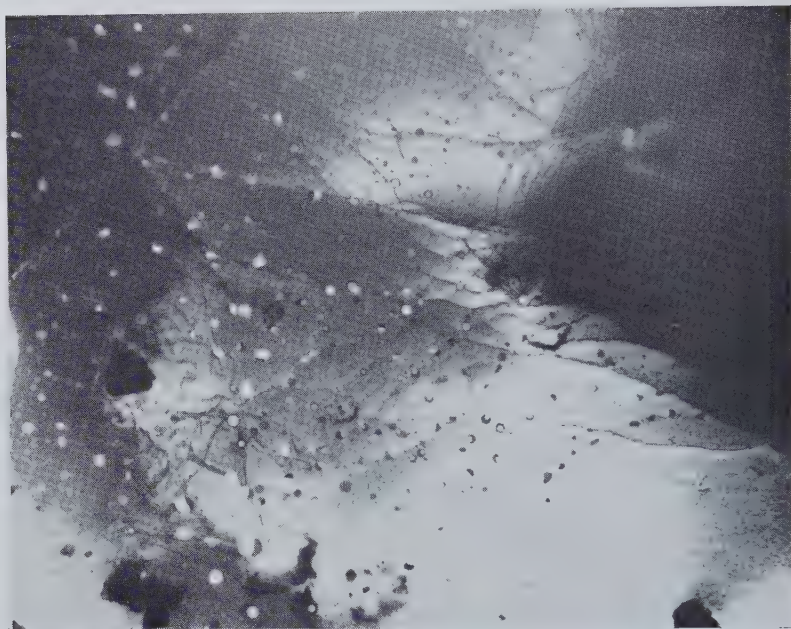
Illustrating the interaction between cavities and dislocations.   Notice that the cavities are filling in with the new black phase.   ×7000.

Fig. 13
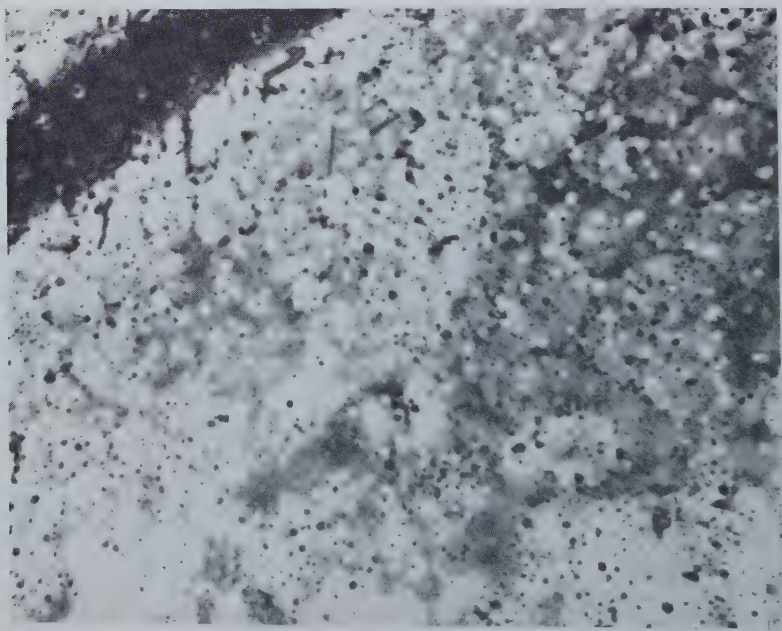
Precipitation inside cavities in the intermediate zone.   There are no dislocations and the cavities are able to move more freely in this case.   ×7000.

A. J. FORTY

Phil. Mag. Ser. 8, Vol. 6, Pl. 108.

Fig. 14

(a)

(b)
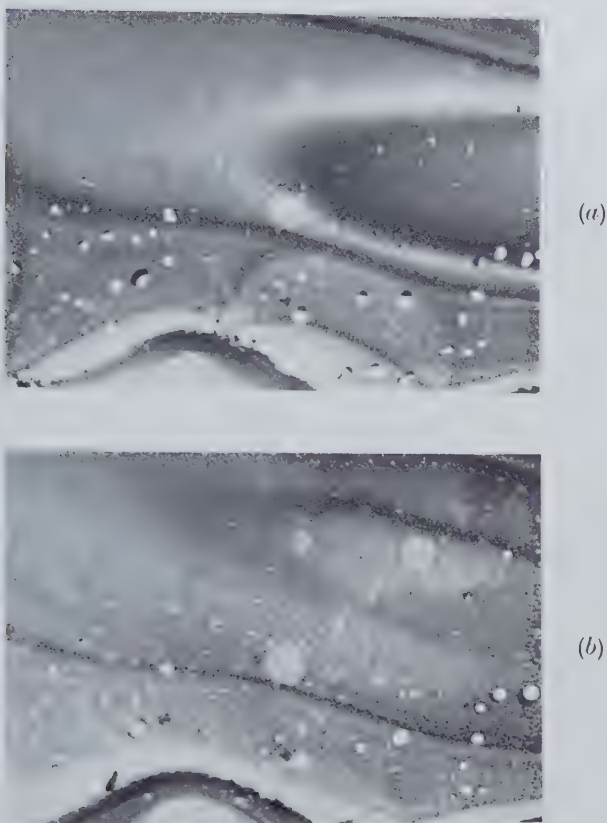
Illustrating the instability of the precipitation inside cavities. (a) Precipitate present in several cavities. (b) Precipitate removed by slight increase of intensity of irradiation locally. ×10 000.

Fig. 15
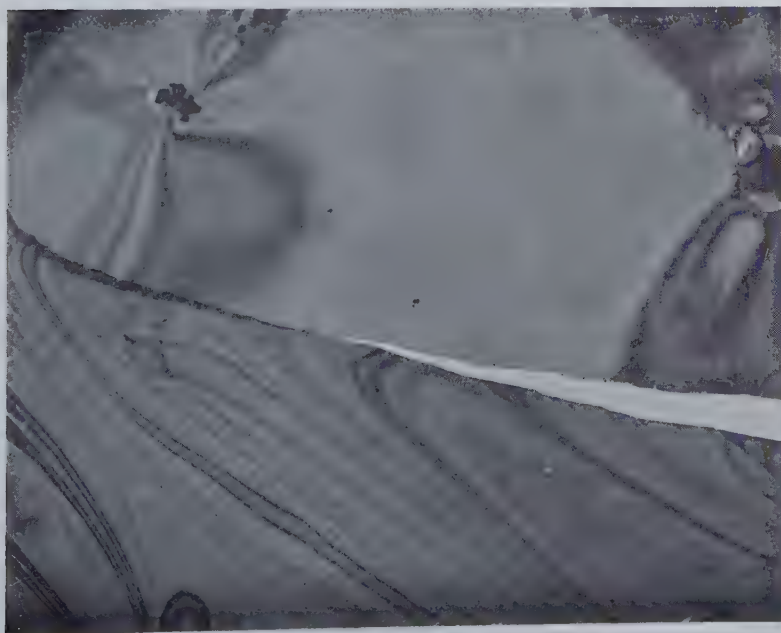
Illustrating the conditioning effect associated with decomposition. ×7000.

Fig. 1
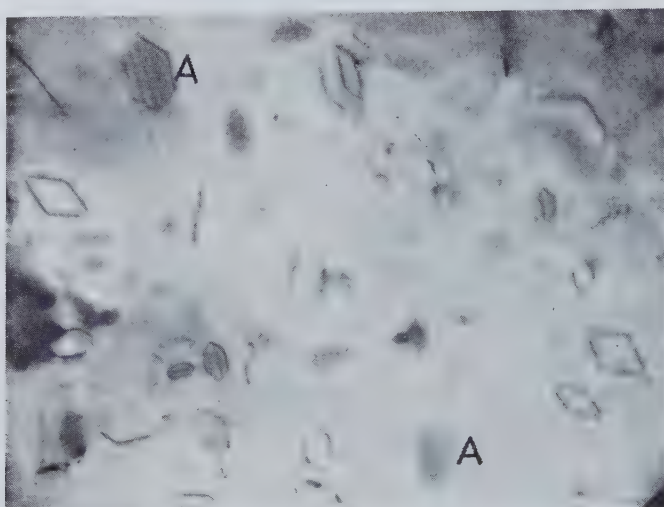
(*a*)
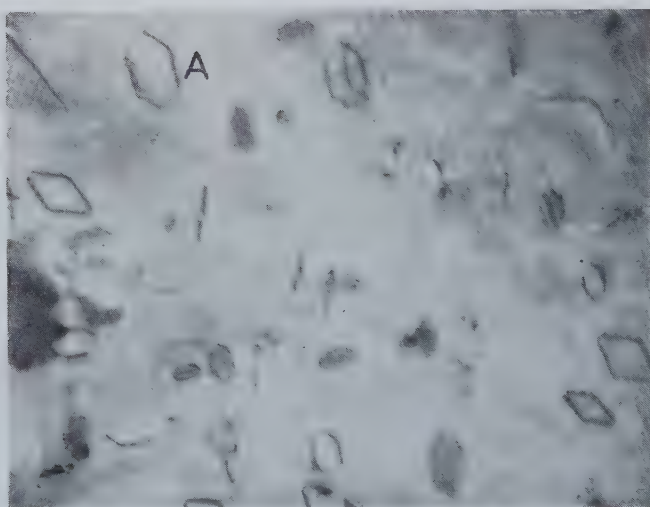
(*b*)

Aluminium 3·5% magnesium quenched from 550°c into silicone oil at −20°c.
(*a*) Prismatic and sessile dislocation loops in the as quenched condition.
×24 000.   (*b*) The same field after being exposed to the electron beam
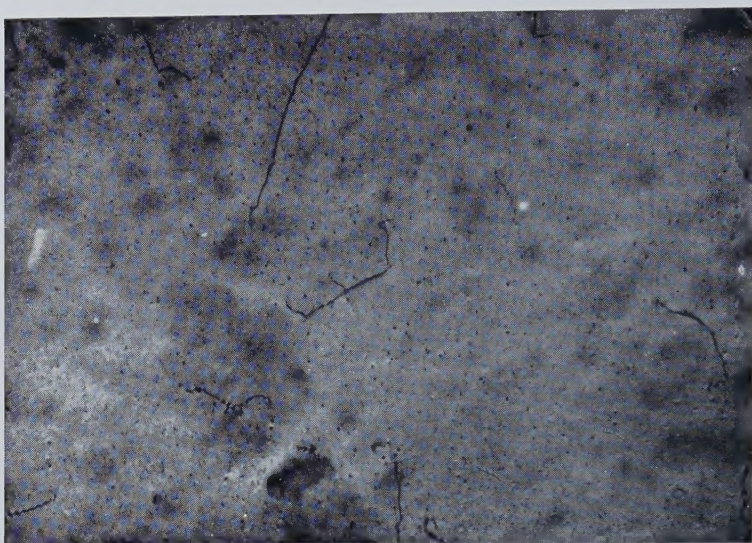for several minutes.   ×24 000.

Fig. 2
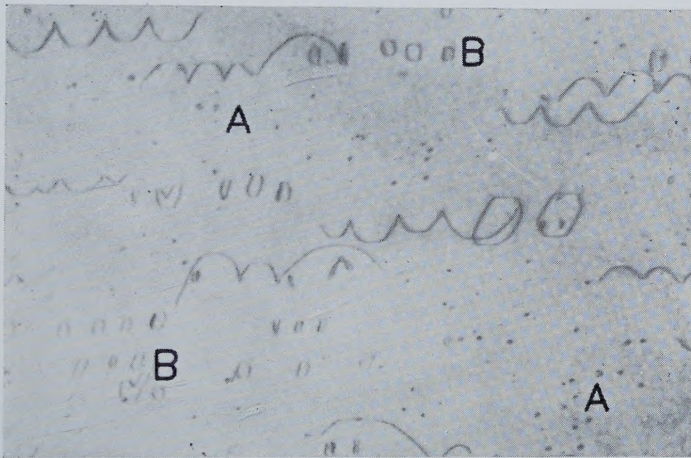
Aluminium–1·2% silicon quenched from 550°c into 50°c distilled water.   Note the average diameter of the condensed vacancy loops is 250 Å compared with the helical dislocation and their loop diameters of 1500 Å.   × 24 000.

Fig. 3

Aluminium–1·2% silicon quenched from 550°c into 50°c water and aged
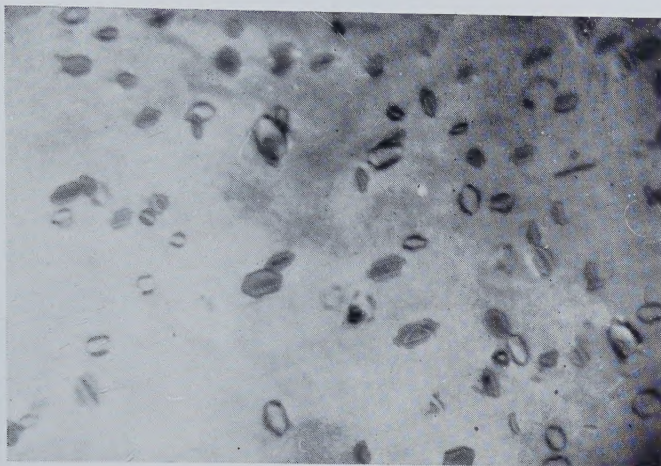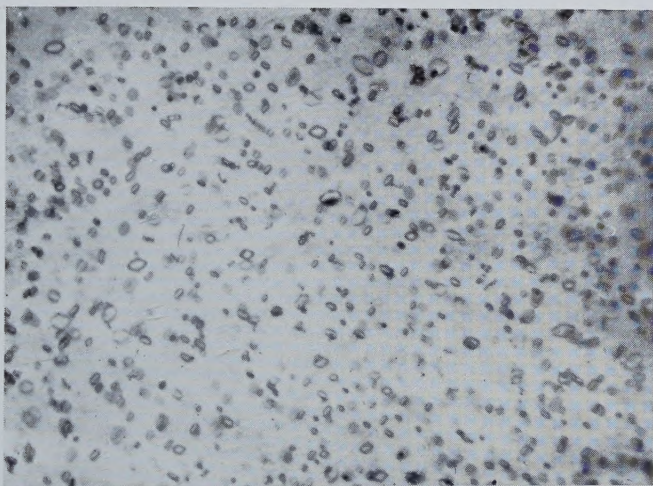at 150°c for 1 hour.   × 24 000.

Fig. 4

Aluminium–1·2% silicon quenched from 550°c into 50°c water and aged
at 200°c for 1 hour.   × 24 000.
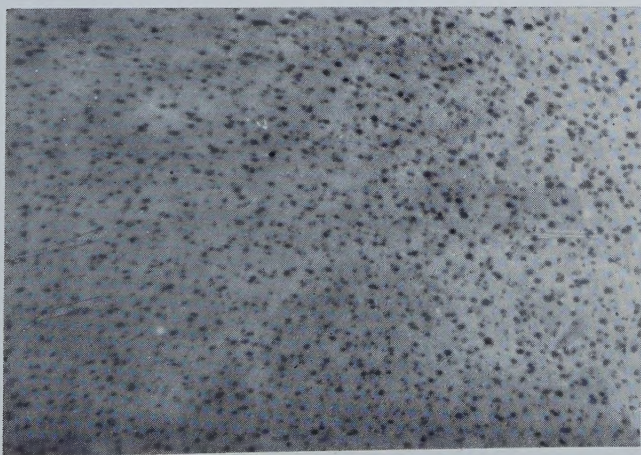
Fig. 5

Variation of loop size with alloying addition; quenched from 550°c into 20°c silicone oil. ×24 000. (a) Super-pure aluminium. (b) Aluminium–1·2% magnesium. (c) Aluminium 1·2% silicon.